WASHINGTON UNIVERSITY
THE HENRY EDWIN SEVER GRADUATE SCHOOL
DEPARTMENT OF CIVIL ENGINEERING

STRUCTURAL HEALTH MONITORING OF FLEXIBLE CIVIL STRUCTURES

by

Juan Martin Caicedo

Prepared under the direction of Professor Shirley J. Dyke

A dissertation presented to the Sever Institute of
Washington University in partial fulfillment
of the requirements of the degree of

DOCTOR OF SCIENCE

August, 2003

Saint Louis, Missouri

WASHINGTON UNIVERSITY
THE HENRY EDWIN SEVER GRADUATE SCHOOL
DEPARTMENT OF CIVIL ENGINEERING

ABSTRACT

STRUCTURAL HEALTH MONITORING OF FLEXIBLE CIVIL STRUCTURES

by Juan Martin Caicedo

ADVISOR: Professor Shirley J. Dyke

August 2003
St. Louis, Missouri

This thesis proposes a structural health monitoring technique for flexible civil structures such as cable-stayed bridges and high rise buildings. A complete description of the technique its implementation on two types of structures is included herein. The methodology consists of two steps. First, the natural excitation technique and the eigensystem realization algorithms are used to identify the natural frequencies and mode shapes of the structure. Then, the least squares solution of the eigenvalue problem is used to determine structural parameters. This methodology can be automated in a way similar to the development of the finite element method. Damage is identified by finding changes in the identified structural parameters over time. The methodology was implemented on three structures. The first structure is the IASC-ASCE SHM benchmark problem. This implementation covers the first two numerical phases and the experimental phase of this problem. The technique is also implemented on a numerical model of the Bill Emerson Memorial Bridge located in Cape Girardeau, Missouri and on a laboratory test specimen representing a cable-stay bridge. These studies demonstrate potential of the methodology for implementation in flexible civil structures.

To my family.

Contents

Tables

Figures

Acknowledgments

Many people have contributed to the development of this work. I express my gratitude to Dr. Shirley J. Dyke for her constant, unconditional support and guidance during the last four years. I would also like to thank Dr. Erik Johnson at the University of Southern California for his valuable comments about the methods discussed in this dissertation and Dr. Gursoy Turan at the Izmir Yuksek Institute of Technology for the endless hours of work in the modeling of the Bill Emerson Memorial Bridge.

I would also like to express my appreciation to Diego F. Giraldo for his invaluable help in the analysis of the experimental benchmark problem, and to Catherine Whyte and Geoff Burrell for their assistance in the construction and testing of the cable-stayed bridge model.

I would like to thank the members of my committee, Dr. Lawrence Bergman, Dr. Shirley Dyke, Dr. Thomas Harmon, Dr. Hiro Mukai, Dr. Kevin Truman for their comments and suggestions about this work.

Lastly, I acknowledge the partial support of the National Science Foundation under grants CMS 97-33272 (Dr. S.C. Liu, Program Director) and CMS 0245402 (Dr. Steve McCabe, Program Director).

Chapter 1

Structural Health Monitoring of Large Structures

Long span bridges and tall buildings are costly to construct and can be critical to the smooth operation of modern infrastructure. The loss or unnecessary closure of key structures in the transportation network will have severe consequences on regional or national economies. Thus, these are likely to be the structures we will initially invest money in to implement monitoring systems. Global methodologies that facilitate detection, quantification and location of damage in large civil structures are needed. These techniques would monitor structural health in an automated (near real-time) mode, reducing the uncertainty of the integrity of the structure and providing valuable information to decision makers after a major event. Structures can be immediately closed if they are damaged and remain open if they are intact, reducing the time that these structures are unused. Monitoring the behavior of these structures will provide immediate indications of the health of the structure, and significantly reduce the impact of unnecessary closures on the economy of the region; and, potentially, the nation. Early detection of damage will also reduce maintenance and operating costs. In the near future the additional cost to install a monitoring system will be relatively inexpensive.

The Ji Lu bridge located in Taiwan provides an extreme example of the catastrophic effects of natural hazards on our infrastructure. The bridge suffered heavy damage in the Chi-Chi Taiwan earthquake on September 21st of 1999 [19]. The 240m long bridge has two symmetric spans supported by a single pier. The deck of the bridge is a prestressed concrete box girder supported by harped cables connected to the center of the deck. The

bridge was under construction at the time of the earthquake. Three precast elements had not been installed yet, and the cables had not undergone final tensioning. The 7.6 magnitude earthquake with an epicenter approximately 6 km northeast of the bridge produced extensive damage in the deck and tower of the bridge. The tower was damaged at both the base and deck levels, indicating large moments at these locations. Pounding of the deck against the two end supports of the bridge was also observed. The deck also presented extensive damage at the connection with the pier.

The Duzce and Kocaeli Turkey earthquakes in 1999 also seriously affected the transportation system of the region [54]. During these events the Arifiye Overpass and the Sakarya Center Bridge collapsed. The deck of the Arifiye Overpass was composed of five U-shaped prestressed concrete beams and was supported by three piers and two abutments. This four span bridge collapsed due to excessive ground displacements disjointing the deck to one of the abutments. The Sakarya Center Bridge had eight spans of simply supported girders and collapsed for similar reasons.

The Bolu Viaduct suffered severe damage during the Duzce earthquake in 1999. The viaduct was under construction at the time of the earthquake, but all structural work was completed. The 2313m long viaduct consists of 117 spans, each 39.6m long. Seven prestressed concrete beams are used in each span and are joined by a deck slab at the piers. The energy dissipation devices were severely damaged and large deformation in the superstructure occurred during the earthquake as shown in Fig. 1-1.

Currently, visual inspection is the most common technique for identifying damage in bridges and other structures and serves as the standard to which all other nondestructive evaluation technologies may be compared. Visual inspection is costly, time consuming, and prone to human error. The high costs for annual inspection are evident. For example, the New Jersey Department of Transportation budgeted over $24 million for bridge inspections in the 2003 fiscal year capital program[66].

(a) Energy Dissipation Device

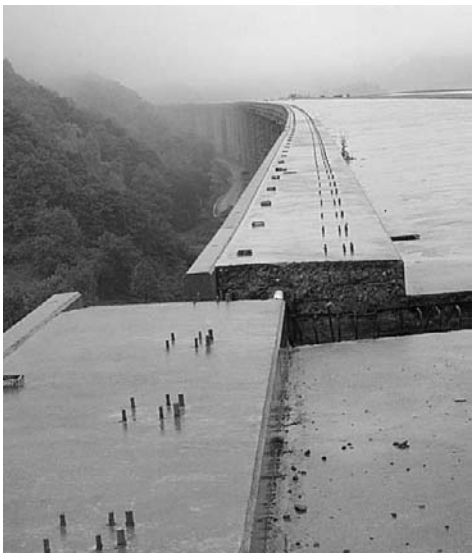

(b) Deck Offset

FIGURE 1-1. Bolu Viaduct after Duzce Earthquake

The time required for such inspections also should be considered. The Seattle Department of Transportation (SDOT) operates and maintains over 150 bridges throughout Seattle, including four movable bridges that must be inspected. After a major catastrophic event such as an earthquake, key bridges on lifeline routes are visually inspected to assess their structural integrity and provide accurate information so that all commuters and other city agencies responding to emergencies can plan safe travel routes [78]. Following the inspection of the “lifeline” bridges, the remainder of the 150 bridges and numerous additional structures in the city must be checked for safety.

In addition to the time and cost for such visual inspections, the consistency of this approach has been questioned. A study done by the Non-Destructive Evaluation Validation Center (NDEVC) in McLean, Virginia found that the accuracy and reliability of visual inspection can vary considerably [68]. Factors such as fear of traffic, visual acuity and color vision, light intensity, inspector workload, perceptions of maintenance, complexity, and accessibility produced significant variability in routine visual inspections. Moreover, in-depth visual inspections using visual inspection alone are not likely to detect

or identify the specific types of defects for which the inspection is prescribed, and may not reveal deficiencies beyond those that could be noted during a routine inspection.

It is clear that there is a need for more reliable, faster and less expensive methods for the evaluation of structures, in particular for expensive and vital structures that are elements of lifeline routes. In the case of a catastrophic event, these routes must quickly be inspected to allow access to emergency teams. There is also a need for methodologies to increase the reliability of the current damage detection techniques, reducing the time and expense involved.

Structural health monitoring (SHM) techniques identify damage by determining changes in the properties of structures. This dissertation focuses on SHM techniques using changes in the dynamic properties of the structure. Although a SHM technique by itself might not provide a complete solution for the monitoring of structures, it can give the inspectors a good estimation of the structure's health in a short period of time. Advances in sensors, data acquisition systems and data networks [62] are facilitating the implementation of these techniques, even in the case of large civil structures [72]. Thus, additional research is needed to develop reliable SHM techniques that will allow a quick and accurate evaluation of structures after a catastrophic event, as well as inexpensive damage identification in structures over their lifetime.

This dissertation proposes a SHM technique based on changes in the modal parameters of the structure, which are obtained from ambient vibration tests using methods currently available in literature. A parameter identification technique is proposed herein, which uses modal parameters to detect changes in the properties of structural members, based on the eigenvalue problem of the undamped equation of motion.

1.1 Review of Previously Developed SHM Techniques

Different types of structural health monitoring methodologies are available depending on the level of identification needed by the user. Traditionally SHM methodologies have been classified into four levels [76]. Level one techniques determine if damage exists in the structure. The existence and location of damage is identified by level two techniques. Level three techniques detect the existence, location and severity of damage. Level four techniques identify the existence, location and severity of damage, as well as define the remaining life of the structure. Additional variables, such as the type of damage or time at which damage occurs, can also be considered by SHM techniques.

SHM methodologies which use variations in the natural frequencies can be used to detect the existence of damage. Salawu [77] presents a review of several methodologies to identify damage in a structure based on changes in the natural frequencies. Several examples are considered in which damage is identified, and in some cases located, using only changes in the resonant frequencies. This reference includes a section discussing the factors to consider when using natural frequencies for damage detection, including topics such as sensor location and frequency range of the measurements.

If the existence and location of damage are required, determination of the mode shapes of the structure is appropriate for some structures. For this task indices such as the modal assurance criteria (MAC) and coordinate modal assurance criteria (COMAC) can be used. The MAC determines the relationship between two mode shapes. If the two mode shapes are linearly dependent the MAC is equal to one, but if they are orthogonal the MAC is equal to zero. The COMAC between two sets of mode shapes is equal to one if the mode shapes are equal at coordinate j. The COMAC will be zero if no correlation exists between the mode shapes. The COMAC can be used to locate damage by identifying the maximum deviation of the mode shape from the undamaged value. Nolambi *et al*. [69], successfully used COMACs to locate damage in a reinforced concrete beam.

Several of these indices, including the MAC, the COMAC, the Mode Shape Curvature (MSC), the Modal Strain Energy Index (MSEI), and Modal Flexibility Index (MFI) were compared by Wang et al [84] using a numerical model of the Tsing Ma Bridge. The Tsing Ma Bridge was the longest suspension bridge in the world when opened to the public in 1997, with a main span of 1377m (4517 ft). The deck is a steel truss supported by two 206m (676 ft) tall reinforced concrete towers, and it carries six lanes of traffic on the upper level and two railway tracks and two emergency lanes on the lower level. For this study the authors developed a finite element model of the bridge using ABAQUS. Three damage scenarios were studied, where damage was induced by reducing the stiffness of members by 98%. All the methodologies tested in this paper are based on changes in the mode shapes of the structure. The authors determined that, from the methodologies studied, the MSC, MSEI and MFI were the most appropriate for the Tsing Ma Bridge. The MSC and the MSEI were the only methodologies that identified all damage case scenarios, although some false positives were obtained.

Another possible implementation of SHM techniques is to identify the time when damage occurred. This goal can be achieved by wavelet transforms as shown by Hou *et al.* [42]. Here the wavelet transform is used to identify discontinuities in the acceleration records, indicating that a member of the structure has fractured. The methodology was successfully applied to the IASC-ASCE Benchmark Problem, discussed later in this dissertation. It is not clear that this method can be implemented in the case of gradual damage.

SHM methodologies to detect the existence, location and degree of damage in a structure are also available in the literature. Most of these techniques use two primary steps. First, a modal identification method is used to determine the natural frequencies and mode shapes of the structure. The second step is to use the identified modal parameters to calculate structural parameters such as moment of inertia in structural members. Damage is located and quantified by examining the changes in the structural parameters between two

different tests. The field of modal identification has been extensively studied in the literature. In contrast, few parameter identification methodologies are available.

One example of a two step method is discussed in [22]. Here the modal parameters are obtained using MODE-ID developed by Beck *et al.* [3]. The method obtains the most likely values of natural frequencies by reducing the error between the measured response of the structure and the calculated response from a numerical model. The methodology gives the modal frequencies, damping ratios, participation factors and mode shapes at the measured degrees of freedom and participation factors. In the second part of the method, the mass and stiffness matrices are identified by updating a model of the structure using a Bayesian probabilistic framework [4].

Bernal [7] also uses a two step method for damage detection. In this case the ERA-OKID algorithm is used for the identification of the natural frequencies and mode shapes of the damage and undamaged structures. Next, the flexibility matrices for both are calculated and compared to determine the existence of damage. Then, Damage Localization Vectors (DLV) are used to locate the damaged vectors.

1.2 Implemented SHM Techniques for Large, Flexible Structures

Flexible structures such as cable-stayed and suspension bridges are increasing in popularity for spans over 200m due to their economy and attractive appearance. The longest cable-stayed bridge today is the Tatara bridge in Japan with a main span of 890m, followed by the Normandi bridge in France with a 856m span. These are complex structures, difficult to model and exhibiting large interactions between the translational and rotational motions. They present new challenges to the SHM continuity, such as very low frequencies of vibration and closely spaced modes. A number of papers describing the studies of modal identification techniques and damage identification can be found in the

literature. To date there does not seem to be a working implementation of a SHM methodology for either of these structures.

The Hong Kong Highway Department made an important investment in the on-line monitoring of three long-span bridges [58]. The Tsing Ma suspension bridge, Kap Shui Mun cable-stayed bridge, and the Ting Kau cable-stayed bridge were instrumented with a total of 774 permanent sensors. A number of studies have been performed using the instrumentation on these bridges in the fields of modal identification and SHM. Probabilistic neural networks (PNN) have been used for the identification and location of damage in a numerical model of the Ting Kau Bridge [67]. The authors concluded that damage in the bridge could be identified and located with an 85% or greater probability using 20 modes of vibration and PNN. Damage was simulated by reducing the stiffness of members of connections or reducing the tension force of a cable for different case scenarios. These damage scenarios considered a 20% reduction in the tension of a cable, 75% loss in the bending stiffness of a connection in the deck, or a 90% loss in the stiffness of a girder. The PPN was trained using natural frequencies from the numerical model. These natural frequencies were contaminated with a random number, simulating errors in the modal identification. In this paper the authors did not use any information from the vibration modes.

Qin *et al.* [73] discussed the modal identification of the Tsing Ma Bridge using the fast eigensystem realization algorithm (FERA). FERA is a modified version of the ERA and uses an eigensystem decomposition of the Hankel matrix instead of the normal singular value decomposition reducing the processing time. Testing on the bridge was performed immediately after its construction. This testing was intended to obtain a digital signature of the bridge for future implementations of SHM methodologies. Ambient vibration produced by wind and the movement of construction machinery was used. The random decrement technique was employed to obtain free response data from the acceleration records obtained. Due to the size of the structure and the availability of sensors, the bridge

was divided into 15 subsections. Testing was carried out on each section, and a reference signal was maintained between the different sections. Thirteen acceleration measurements were obtained for every subsection, including 3 at the reference point. Mode shapes were obtained by assembling the partial mode shapes obtained from each subsection. The authors obtained a total of 79 natural frequencies from the structure; 35 mode shapes with 26 coordinates were identified from these 79 modes. Many of the transverse modes of the deck were found to be coupled with torsional modes. The identified modal parameters obtained showed good agreement with the modal parameters from a finite element analysis.

The structural health monitoring system of the Namhae Suspension Bridge is described in Kim *et al.* [56]. The bridge connects mainland Korea with Namhae Island and has a total length of 660m. The structural health monitoring system of the bridge consists of 74 static sensors and 36 channels for dynamic measurements. The static sensors include 30 tiltimeters and 44 static strain gauges. The dynamic system includes 4 displacement sensors, 10 dynamic strain gauges, 12 uniaxial accelerometers, 6 channels for triaxial accelerometers, and 4 channels for anemometers. The natural frequencies of the bridge have been identified using the dynamic system installed in the bridge. In this study the natural frequencies were obtained by identifying peaks in the power spectral density functions.

Lew *et al.* [60] studied four different methods for the modal identification of flexible structures. The structure selected for this study was a Mini-Mast structure at the NASA Langely Research Center. The data for the identification was obtained from a numerical model of the structure and different levels of noise were superimposed. The eigensystem realization algorithm (ERA), the ERA with data correlation (ERA/DC), the MDVV algorithm (named after Moonen, DeMoor, Vandenberghe and Vandewalle), and the Q-Markov algorithm. Impulse response functions were available for the different algorithms. The authors found that ERA/DC had a computational advantage over ERA because it

produces a square Hankel matrix, although both methods produced similar results. The Q-Markov method requires more data than ERA to obtain similar results. Similarly, the Q-Markov method required a larger matrix for the singular value decomposition.

Huang *et al.* [43] implemented the Ibrahim time-domain (ITD) technique to measure the modal parameters Yuang-Shan bridge. The 360 m long highway bridge consists of a three-span continuous prestressed concrete box-girder. Two types of excitation were used in this paper. A truck falling from a block or suddenly stopping on the bridge provided the first type of excitation, and ambient excitation provided the second type. The random decrement technique [24] was used for the implementation of the methodology using ambient vibration. The authors obtained 14 modes with the free vibration data and 12 modes with the ambient vibration tests. Good correlation was found between the modes found with the ambient vibration tests and the free response tests.

Kim *et al*. [55] studied the effects of the mass of vehicles crossing different type of bridges. The bridges studied were a suspension bridge with a main span of 404m and two side spans of 128m, a five span highway bridge with a maximum span of 95m and a simply supported bridge with a span of 46m. Thirty minutes of acceleration records were obtained for each bridge. The data was categorized according to the vehicle mass, and the power spectral density was calculated for each case. The authors did not find any difference in the peaks of the power spectral densities for the first two bridges, indicating that the effect of the mass on these structures was small. However, in the small bridge the variation of the natural frequency was estimated to be 5.4%.

1.3 Overview

In this dissertation a two step structural health monitoring methodology is proposed and validated. The technique uses available modal identification algorithms such as the natural excitation technique (NExT), and the eigensystem realization algorithm (ERA) to obtain

natural frequencies and mode shapes of the structure. A new parameter identification technique is proposed and implemented to assess the health of the structure. An approach is described to implement the parameter identification technique using a procedure similar to finite elements. This facilitates implementation of the technique to any type of structure.

In the second chapter of this dissertation the structural health monitoring technique is described in detail along with necessary background information. Here NExT and ERA are discussed. Special emphasis is given to the effects of using free vibration response instead of impulse response functions in ERA. The chapter finishes with the description of the least squares solution of the eigenvalue problem. This method is used for the identification of parameters in elements of the structure, such as Young's modulus or moment of inertia. A full description of the method is provided, including a discussion of how to implement it using a finite element framework. This includes the formation of elemental matrices, transformation from local to global coordinates, application of constraint equations and, finally, boundary conditions. Although the methodology described is developed for a beam element, it can be extended to other finite elements. This facilitates the implementation of the technique to any type of structure.

The third chapter discusses the implementation of the SHM methodology to the IASC-ASCE SHM benchmark problem. This benchmark problem has served as a testbed for the proposed methodology during the last four years. Descriptions of the benchmark structure and the various numerical and experimental phases of the benchmark problem are provided. The results and lessons learned from the implementation of the proposed methodology are also discussed herein.

The sensitivity of static and dynamic parameters to damage in the deck of a cable-stayed bridge is discussed in chapter four. The structure selected for this study is the Bill Emerson Memorial Bridge located in Cape Girardeau, Missouri, U.S.A. The sensitivity of

the static displacements, natural frequencies and mode shapes to damage in the deck of the bridge is studied. For this study a nonlinear static model of the bridge is developed. A discussion of the challenges in modeling these types of structures is provided.

Chapter five presents the implementation of the proposed SHM technique to the numerical model of the Emerson Bridge described in chapter four. Here different identification models are studied. NExT and ERA are used for the identification of the modal parameters and the least squares solution of the eigenvalue problem is used to detect changes in the elemental properties of the structure. Differences between the implementation of the technique for large scale structures such as the Emerson Bridge and smaller structures such as the benchmark structure of chapter three are identified, providing important information for future implementations of the technique.

Chapter six discusses the design, construction and testing of a laboratory experiment used for verification of the proposed SHM methodology. A cable-stayed bridge model with one pier and two spans is designed and constructed for this purpose. Modal identification was performed using hammer excitation and the ERA. Damage is induced in the bridge deck by reducing the section of one of the members. The damage is correctly located by identifying changes in the structural parameters using a least squares solution of the eigenvalue problem.

A summary and conclusions of the presented work is given in chapter seven. A section describing the pros and cons of the proposed methodology is provided in this chapter. Conclusions regarding the implementation of the methodology to large scale structures and a comparison to implementations on other types of structures are also discussed. Finally, some possibilities for future research in the area of SHM for large scale structures are provided.

Chapter 2

Structural Health Monitoring Techniques

Structural Health Monitoring (SHM) is a topic of interest for researchers in the present decade, and currently SHM techniques are being developed and verified around the world. Recent conferences such as the International Workshop in Structural Health Monitoring, usually held at Stanford University, [21] and the International Conference on Structural Health Monitoring, held this year in Tokyo, Japan (November 13-15), demonstrate the interest in this topic.

Different approaches are available depending on the type of damage identification required. For example, wavelet transforms are used to identify discontinuities in acceleration records, making it possible to identify the time when damage occurs [42], or changes in the flexibility matrix can be used to detect the existence of damage [8]. Several of these methods use modal parameters for damage identification. Typically these methods have two steps. First, the natural frequencies and mode shapes of the structure are identified using a modal identification technique. Then, structural parameters are identified. The field of modal identification has been widely studied by aerospace, mechanical and civil engineers, and method such as the Eigensystem Realization Algorithm are widely used for a vast range of applications. In contrast, few structural parameter identification techniques are available in the literature.

In this chapter a SHM technique is proposed. The method uses the eigenvalue problem of the undamped equations of motion to identify stiffness values. Changes in these stiffness

values will indicate the location and extent of damage in a structure. The first part of this chapter discusses the methods used for the identification of the modal parameters. Next, the structural parameter identification technique proposed in this dissertation is discussed. Last, two indices used for damage identification are presented. These indices are used to identify the change in order of mode shapes in structures due to damage (i.e. the 9th mode trading places with the 8th mode) in the subsequent parameter studies.

2.1 Modal Identification

In this section two methods are discussed which, when combined, are the basis of the modal identification step. These include the natural excitation technique (NExT) and the eigensystem realization algorithm (ERA). The first method is used to obtain a free vibration record from ambient vibration tests, allowing modal identification without knowing the forces exciting the structure. The ERA is used to obtain the modal parameters of the structure from the free vibration records.

2.1.1 Natural Excitation Technique

The natural excitation technique allows one to obtain data that can be treated as free responses from a structure when the input is not measured, or is actually unmeasurable. Here the excitation is assumed to be stationary with frequency content that spans the modes of vibration of the structure and uncorrelated with the response of the structure. The method was developed by James et al. [45-47], and shows that the matrix of correlation functions between the responses of the system and a response to be selected to be the reference response is a solution of the homogenous matrix equation of motion.

Consider the equation of motion

$$\mathbf{M}\ddot{\boldsymbol{y}}(t) + \mathbf{C}\dot{\boldsymbol{y}}(t) + \mathbf{K}\boldsymbol{y}(t) = \boldsymbol{u}(t), \tag{2-1}$$

where $\mathbf{M}$, $\mathbf{C}$ and $\mathbf{K}$ are the mass, damping and stiffness matrices of the structure, $\mathbf{y}(t)$ is the vector of displacements at time t, $\mathbf{u}(t)$ are the excitation forces and $\dot{(\ )}$ denotes the derivative with respect to time. When the inputs are random processes Eq. 2-1 is written

$$\mathbf{M}\ddot{\boldsymbol{Y}}(t) + \mathbf{C}\dot{\boldsymbol{Y}}(t) + \mathbf{K}\boldsymbol{Y}(t) = \boldsymbol{U}(t), \tag{2-2}$$

where $\boldsymbol{Y}(t)$ is a stochastic displacement vector process and $\boldsymbol{U}(t)$ is the stochastic force excitation vector process. Postmultiplying Eq. 2-2 by a reference scalar stochastic process $Y_i(s)$ yields

$$\mathbf{M}\ddot{\boldsymbol{Y}}(t)Y_i(s) + \mathbf{C}\dot{\boldsymbol{Y}}(t)Y_i(s) + \mathbf{K}\boldsymbol{Y}(t)Y_i(s) = \boldsymbol{U}(t)Y_i(s). \tag{2-3}$$

Taking the expected value of Eq. 2-3 we obtain

$$\mathbf{M}\boldsymbol{R}_{\ddot{\boldsymbol{Y}}Y_i}(t, s) + \mathbf{C}\boldsymbol{R}_{\dot{\boldsymbol{Y}}Y_i}(t, s) + \mathbf{K}\boldsymbol{R}_{\boldsymbol{Y}Y_i}(t, s) = \boldsymbol{R}_{\boldsymbol{U}Y_i}(t, s), \tag{2-4}$$

where $\boldsymbol{R}(\ )$ denotes a vector of correlation functions between the random processes at times t and s. Recognizing that the excitation forces are uncorrelated with the responses of the structure, Eq. 2-4 yields

$$\mathbf{M}\boldsymbol{R}_{\ddot{\boldsymbol{Y}}Y_i}(t, s) + \mathbf{C}\boldsymbol{R}_{\dot{\boldsymbol{Y}}Y_i}(t, s) + \mathbf{K}\boldsymbol{R}_{\boldsymbol{Y}Y_i}(t, s) = 0. \tag{2-5}$$

For weakly stationary processes it can be shown that [5]

$$\dot{\mathbf{R}}_{\boldsymbol{Y}Y_i}(\tau) = \mathbf{R}_{\dot{\boldsymbol{Y}}Y_i}(\tau) = -\mathbf{R}_{\boldsymbol{Y}\dot{Y}_i}(\tau), \tag{2-6}$$

where $\tau = t - s$. Taking the 4th derivative of Eq. 2-4 yields

$$\mathbf{M}\ddot{\boldsymbol{R}}_{\ddot{Y}\ddot{Y}_i}(t-s) + \mathbf{C}\dot{\boldsymbol{R}}_{\ddot{Y}\ddot{Y}_i}(t-s) + \mathbf{K}\boldsymbol{R}_{\ddot{Y}\ddot{Y}_i}(t-s) = 0. \tag{2-7}$$

Equation 2-7 is of the same form as Eq. 2-1, showing that the correlation functions can be viewed as free responses.

2.1.2 Eigensystem Realization Algorithm

The Eigensystem Realization Algorithm was developed by Juang and Pappa in 1985 [49], and it has shown to be an effective method for modal identification of flexible structures [60]. This algorithm uses the principles of minimum realization to obtain a state space representation of the system. For a better understanding of how the algorithm works, and the implications of using the NExT or RDT with ERA, it is necessary to introduce the concepts of realizations and Markov parameters [51, 48].

The state space representation of a linear, time-invariant, discrete system is defined by

$$\mathbf{x}(k+1) = \mathbf{A}\mathbf{x}(k) + \mathbf{B}\mathbf{u}(k) \tag{2-8}$$

$$\mathbf{y}(k) = \mathbf{C}\mathbf{x}(k) + \mathbf{D}\mathbf{u}(k), \tag{2-9}$$

where $\mathbf{A}$, $\mathbf{B}$, $\mathbf{C}$ and $\mathbf{D}$ are the state matrices, and $\mathbf{x}$ is the state vector at the k-th step; $\mathbf{u}$ $(r \times 1)$ and $\mathbf{y}$ $(m \times 1)$ are the input and output vectors of the system. Assume that the system is excited by a discrete-time impulse function with an amplitude equal to one, and that the initial conditions of the system are zero,

$$\mathbf{u}(0) = 1; \mathbf{u}(k) = 0 \tag{2-10}$$

and

$$\mathbf{x}(0) = 0; \mathbf{x}(k) \neq 0, \tag{2-11}$$

for k = 1, 2, 3... s. Inserting these values into Eqs. 2-8 and 2-9, we obtain

$$\mathbf{y}_0 = \mathbf{D}; \mathbf{y}_1 = \mathbf{CB}; \mathbf{y}_2 = \mathbf{CAB}; \mathbf{y}_k = \mathbf{CA}^{k-1}\mathbf{B}. \tag{2-12}$$

The constant matrices $\mathbf{D}$, $\mathbf{CB}$, $\mathbf{CAB}$,... $\mathbf{CA}^{k-1}\mathbf{B}$ are known as Markov parameters. A realization of the system is defined as the matrices $\mathbf{A}$, $\mathbf{B}$ and $\mathbf{C}$ that best yield the responses of the system to be identified.

The ERA is a technique used to determine the system matrices from pulse response records. The ERA uses the Markov parameters for the identification of the system. The first step in the ERA is to form the Hankel matrix from the system responses as

$$\mathbf{H}(0) = \begin{bmatrix} \mathbf{y}_1 & \mathbf{y}_2 & \cdots & \mathbf{y}_\gamma \\ \mathbf{y}_2 & \mathbf{y}_3 & \cdots & \mathbf{y}_{\gamma+1} \\ & & \ddots & \vdots \\ \mathbf{y}_p & \mathbf{y}_{p+1} & \cdots & \mathbf{y}_{p+\gamma-1} \end{bmatrix}, \tag{2-13}$$

where γr and pm are the number of columns and rows of the Hankel matrix. Substituting Eq. 2-12 in Eq. 2-13, the Hankel matrix becomes

$$\mathbf{H}(0) = \begin{bmatrix} \mathbf{CB} & \mathbf{CAB} & \ldots & \mathbf{CA}^{\gamma-1}\mathbf{B} \\ \mathbf{CAB} & \mathbf{CA}^2\mathbf{B} & \ldots & \mathbf{CA}^{\gamma}\mathbf{B} \\ & & \ddots & \vdots \\ \mathbf{CA}^{p-1}\mathbf{B} & \mathbf{CA}^{p}\mathbf{B} & \ldots & \mathbf{CA}^{p+\gamma-2}\mathbf{B} \end{bmatrix}. \tag{2-14}$$

The matrix $\mathbf{H}(0)$ can be written in terms of two matrices as

$$\mathbf{H}(0) = \mathbf{PQ} = \begin{bmatrix} \mathbf{C} \\ \mathbf{CA} \\ \vdots \\ \mathbf{CA}^{p-1} \end{bmatrix} \begin{bmatrix} \mathbf{B} & \mathbf{AB} & \dots & \mathbf{A}^{\gamma-1}\mathbf{B} \end{bmatrix}, \tag{2-15}$$

where $\mathbf{P}$ is defined as the observability matrix and $\mathbf{Q}$ is defined as the controllability matrix. The next step is to perform a singular value decomposition of the Hankel matrix

$$\mathbf{H}(0) = \mathbf{R}\Sigma\mathbf{S}^T, \tag{2-16}$$

where the matrix Σ contains nonnegative diagonal elements in decreasing order, and the columns of $\mathbf{R}$ and $\mathbf{S}$ are orthonormal. Under ideal conditions, the matrix Σ is

$$\Sigma = \begin{bmatrix} \Sigma_g & \mathbf{0} \\ \mathbf{0} & \mathbf{0} \end{bmatrix}, \tag{2-17}$$

where g is the order of the system to be identified and the 0 are matrices of appropriate dimensions. In reality, the diagonal terms of the matrix Σ are non-zero as they are contaminated with small singular values. By eliminating the small singular values it is possible to obtain a minimum realization that represents the system to be identified.

From Eqs. 2-16 and 2-17 we can write

$$\mathbf{H}(0) = (\mathbf{R}\Sigma^{1/2})(\Sigma^{1/2}\mathbf{S}^T) = \mathbf{PQ}, \tag{2-18}$$

$$\mathbf{P} = \mathbf{R}\Sigma^{1/2}; \ \mathbf{Q} = \Sigma^{1/2}\mathbf{S}^T. \tag{2-19}$$

After examining Eqs. 2-19 and 2-15 we conclude that the first m rows of $\mathbf{P}$ are the matrix $\mathbf{C}$, and the first r columns of $\mathbf{Q}$ are $\mathbf{B}$.

To calculate the system matrix $\mathbf{A}$, another Hankel matrix $\mathbf{H}(1)$ is computed as

$$\mathbf{H}(1) = \begin{bmatrix} \mathbf{Y}_2 & \mathbf{Y}_3 & \cdots & \mathbf{Y}_{\gamma+1} \\ \mathbf{Y}_3 & \mathbf{Y}_4 & \cdots & \mathbf{Y}_{\gamma+2} \\ & & \ddots & \vdots \\ \mathbf{Y}_{p+1} & \mathbf{Y}_{p+2} & \cdots & \mathbf{Y}_{p+\gamma} \end{bmatrix} = \begin{bmatrix} \mathbf{CAB} & \mathbf{CA}^2\mathbf{B} & \cdots & \mathbf{CA}^{\gamma}\mathbf{B} \\ \mathbf{CA}^2\mathbf{B} & \mathbf{CA}^3\mathbf{B} & \cdots & \mathbf{CA}^{\gamma+1}\mathbf{B} \\ & & \ddots & \vdots \\ \mathbf{CA}^{p}\mathbf{B} & \mathbf{CA}^{p+1}\mathbf{B} & \cdots & \mathbf{CA}^{p+\gamma-1}\mathbf{B} \end{bmatrix}. \tag{2-20}$$

$$\mathbf{H}(1) = \mathbf{PAQ}, \tag{2-21}$$

$$\mathbf{H}(1) = \mathbf{R}\Sigma^{1/2}\mathbf{A}\Sigma^{1/2}\mathbf{S}^T. \tag{2-22}$$

From Eq. 2-22 $\mathbf{A}$ is given by

$$\mathbf{A} = \Sigma^{-1/2}\mathbf{R}^T\mathbf{H}(1)\mathbf{S}\Sigma^{-1/2}. \tag{2-23}$$

When the ERA is used in conjunction with NExT, the input signal is not an impulse response function but a free response function. Thus, the initial conditions are

$$\mathbf{u}(k) = 0;\ \mathbf{x}(k) \neq 0. \tag{2-24}$$

With these new initial conditions Eq. 2-12 becomes

$$\mathbf{Y}_0 = \mathbf{C}\mathbf{x}(0);\ \mathbf{Y}_1 = \mathbf{CA}\mathbf{x}(0);\ \mathbf{Y}_2 = \mathbf{CA}^2\mathbf{x}(0);\ \mathbf{Y}_k = \mathbf{CA}^k\mathbf{x}(0), \tag{2-25}$$

and the Hankel matrix is

$$H(0) = \begin{bmatrix} \mathbf{Y}_1 & \mathbf{Y}_2 & \cdots & \mathbf{Y}_{\gamma} \\ \mathbf{Y}_2 & \mathbf{Y}_3 & \cdots & \mathbf{Y}_{\gamma+1} \\ & & \ddots & \vdots \\ \mathbf{Y}_p & \mathbf{Y}_{p+1} & \cdots & \mathbf{Y}_{p+\gamma} \end{bmatrix} = \begin{bmatrix} \mathbf{CAx}(0) & \mathbf{CA}^2\mathbf{x}(0) & \cdots & \mathbf{CA}^{\gamma}\mathbf{x}(0) \\ \mathbf{CA}^2\mathbf{x}(0) & \mathbf{CA}^3\mathbf{x}(0) & \cdots & \mathbf{CA}^{\gamma+1}\mathbf{Bx}(0) \\ & & \ddots & \vdots \\ \mathbf{CA}^p\mathbf{x}(0) & \mathbf{CA}^{p+1}\mathbf{x}(0) & \cdots & \mathbf{CA}^{p+\gamma-1}\mathbf{x}(0) \end{bmatrix}. \quad (2\text{-}26)$$

With the singular value decomposition Eq. 2-26 becomes

$$\mathbf{H}(0) = \mathbf{R}\Sigma\mathbf{S}^T = \mathbf{PQ}_{\mathbf{x}}, \quad (2\text{-}27)$$

where

$$\mathbf{Q}_{\mathbf{x}} = \begin{bmatrix} \mathbf{x}(0) & \mathbf{Ax}(0) & \cdots & \mathbf{A}^{\gamma-1}\mathbf{x}(0) \end{bmatrix}. \quad (2\text{-}28)$$

Similar to the case of an impulsive input, the $\mathbf{C}$ matrix will still be the first m rows of $\mathbf{P}$. However, in this case the $\mathbf{B}$ matrix cannot be described as the first r columns of $\mathbf{Q}_{\mathbf{x}}$. To calculate the matrix $\mathbf{A}$ the Hankel matrix $\mathbf{H}(1)$ is formed

$$H(1) = \begin{bmatrix} \mathbf{Y}_2 & \mathbf{Y}_3 & \cdots & \mathbf{Y}_{\gamma+1} \\ \mathbf{Y}_3 & \mathbf{Y}_4 & \cdots & \mathbf{Y}_{\gamma+2} \\ & & \ddots & \vdots \\ \mathbf{Y}_{p+1} & \mathbf{Y}_{p+2} & \cdots & \mathbf{Y}_{p+\gamma} \end{bmatrix} = \begin{bmatrix} \mathbf{CA}^2\mathbf{x}(0) & \mathbf{CA}^3\mathbf{x}(0) & \cdots & \mathbf{CA}^{\gamma+1}\mathbf{x}(0) \\ \mathbf{CA}^3\mathbf{x}(0) & \mathbf{CA}^4\mathbf{x}(0) & \cdots & \mathbf{CA}^{\gamma+2}\mathbf{Bx}(0) \\ & & \ddots & \vdots \\ \mathbf{CA}^{p+1}\mathbf{x}(0) & \mathbf{CA}^{p+2}\mathbf{x}(0) & \cdots & \mathbf{CA}^{p+\gamma}\mathbf{x}(0) \end{bmatrix}, \quad (2\text{-}29)$$

$$\mathbf{H}(1) = \mathbf{PAQ}_{\mathbf{x}} = \mathbf{R}\Sigma^{1/2}\mathbf{A}\Sigma^{1/2}\mathbf{S}^T. \quad (2\text{-}30)$$

Using Eq. 2-30 we can obtain

$$\mathbf{A} = \boldsymbol{\Sigma}^{-1/2}\mathbf{R}^{T}\mathbf{H}(1)\mathbf{S}\boldsymbol{\Sigma}^{-1/2}. \tag{2-31}$$

As shown by Eqs. 2-23 and 2-31 the ERA can be applied to free vibration data without modification for the calculations of the **A** and **C** matrices. The **B** matrix cannot be identified with the free response data obtained from NExT.

2.2 Parameter Identification Technique

Once the modal parameters of the structure are determined, these must be related to structural parameters such as moment of inertia or Young's modulus to detect damage. The change in these parameters will allow us to identify, locate and quantify the damage in a structure. In this section a method is proposed to identify structural parameters from the modal data obtained from the ERA.

2.2.1 Least Squares of Eigenvalue Problem

The structural parameter identification method proposed in this section uses the undamped natural frequencies and mode shapes to determine parameters that form the elemental stiffness matrices of the structure. Although in this dissertation emphasis is given to the identification of Young's modulus, the methodology can also be used to identify other parameters that affect the stiffness matrix such as moments of inertia. To use this method the mass matrix of the structure must first be estimated. Consider the undamped eigenvalue problem

$$(\mathbf{K} - \mathbf{M}\lambda_i)\phi_i = 0, \tag{2-32}$$

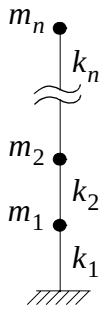

FIGURE 2-1. Lumped Mass Model of an *n*-story Structure

where $\mathbf{K}$ and $\mathbf{M}$ are the $n \times n$ stiffness and mass matrices, respectively, and λ_i and ϕ_i are the *i*-th eigenvalue and eigenvector. Equation 2-32 can be written as

$$\mathbf{K}\phi_i = \mathbf{M}\lambda_i\phi_i . \tag{2-33}$$

Typically the number of identified modes is significantly smaller than the number of degrees of freedom in the identification model. Thus, from Eq. 2-33 it is not generally possible to determine $\mathbf{K}$ because there are $(n \times (n+1))/2$ unknowns (due to symmetry), and there are only $n \times m$ equations, where m is the number of identified natural frequencies and mode shapes. Equation 2-33 can be rewritten as

$$\theta_i\mathbf{r} = \mathbf{M}\lambda_i\phi_i , \tag{2-34}$$

where θ_i is a matrix formed using the elements of the *i*-th eigenvector ϕ_i and $\mathbf{r}$ is a vector of the unknown parameters. To demonstrate this concept consider the *n*-story shear structure shown in Fig. 2-1. The left hand side of Eq. 2-33 is

$$\mathbf{K}\phi_i = \begin{bmatrix} k_1 + k_2 & -k_2 & \cdots & 0 & 0 \\ -k_2 & k_2 + k_3 & \cdots & 0 & 0 \\ & & \ddots & & \vdots \\ 0 & 0 & & k_n + k_{n-1} & -k_n \\ 0 & 0 & \cdots & -k_n & k_n \end{bmatrix} \begin{bmatrix} \phi_{i,1} \\ \phi_{i,2} \\ \vdots \\ \phi_{i,n-1} \\ \phi_{i,n} \end{bmatrix}, \tag{2-35}$$

where $\phi_{i,k}$ is the *k*-th component of the *i*-th mode shape. This term can be rewritten as

$$\begin{bmatrix} \phi_{i,1} & \phi_{i,1} - \phi_{i,2} & 0 & 0 & 0 \\ 0 & \phi_{i,2} - \phi_{i,1} & \phi_{i,2} - \phi_{i,3} & 0 & 0 \\ 0 & 0 & & \ddots & \vdots \\ 0 & 0 & & \phi_{i,n-1} - \phi_{i,n-2} & \phi_{i,n-1} - \phi_{i,n} \\ 0 & 0 & \cdots & 0 & \phi_{i,n} - \phi_{i,n-1} \end{bmatrix} \begin{bmatrix} k_1 \\ k_2 \\ \vdots \\ k_{n-1} \\ k_n \end{bmatrix} = \theta_i \mathbf{r}. \tag{2-36}$$

Stacking Eq. 2-34 for the *m* identified modes we write

$$\Theta \mathbf{r} = \Gamma, \tag{2-37}$$

where

$$\Gamma = \begin{bmatrix} \mathbf{M}\lambda_1\phi_1 \\ \mathbf{M}\lambda_2\phi_2 \\ \\ \mathbf{M}\lambda_m\phi_m \end{bmatrix}, \text{ and } \Theta = \begin{bmatrix} \theta_1 \\ \theta_2 \\ \\ \theta_m \end{bmatrix}. \tag{2-38}$$

From Eq. 2-37 the vector of unknown parameters $\mathbf{r}$ can be obtained using

$$\mathbf{r} = \Theta^{-p}\Gamma \tag{2-39}$$

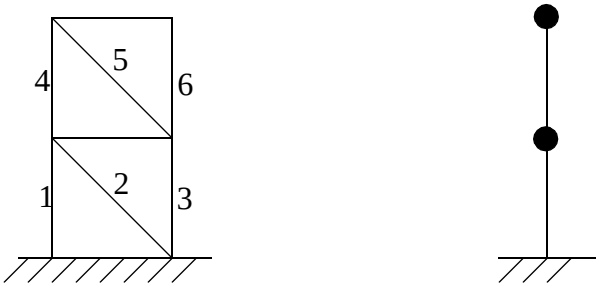

a. Two floor structure **b. Identification model**

FIGURE 2-2. Two Floor Structure and Identification Model

where $(\ )^{-p}$ denotes the pseudoinverse. If more equations are available than unknowns, the solution is equivalent to a least squares solution for the unknown parameters.

One of the advantages of this method is that information related to the geometry of the structure is used, and only nonzero elements of the stiffness matrix are identified. It is also possible to include known values of the stiffness matrix (*i.e.*, members known to be healthy) to improve the results obtained.

The procedure to obtain the matrix θ_i in Eq. 2-34 can be automated in a way similar to the development of the finite element method. When creating the identification finite element mesh, special care should be taken to account for elements whose stiffness cannot be isolated from the contribution of nearby elements. Consider the two floor structure shown in Fig. 2-2a, where the parameters to be identified are the Young's moduli for every element. Assuming that the floors are rigid and only one measurement is obtained per floor, it is not possible to identify Young's modulus for each element. Elements 1, 2 and 3 will affect the stiffness of the first floor, and elements 4, 5 and 6 will affect the stiffness of the second floor. Thus, the correct identification model to use in this case is the two degree of freedom identification model shown in Fig. 2-2b. Typically, modeling errors will affect the resulting identified parameters due to the differences between the real structure and the identification model. The identified parameters are not an actual representation of the real

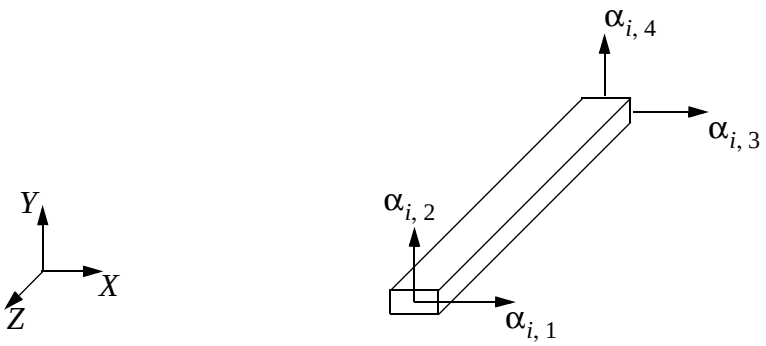

FIGURE 2-3. Shear Finite Element

values but the variations of these parameters are proportional to the reductions induced by damage making it possible to identify and quantify the location of damage [15].

In the next paragraphs these steps are described for an Euler-Bernoulli element. A similar procedure can be applied for other finite elements.

Elemental Matrix

In this section the elemental identification matrix, θ_e, for a shear beam element is developed. At the end of this section the elemental identification matrix for an Euler-Bernoulli beam is obtained through a similar procedure.

Consider the stiffness matrix for the 2D shear beam finite element shown in Fig. 2-3.

$$\mathbf{k}_e = \frac{12E}{L^3}\begin{bmatrix} I_y & 0 & -I_y & 0 \\ 0 & I_x & 0 & -I_x \\ -I_y & 0 & I_y & 0 \\ 0 & -I_x & 0 & I_x \end{bmatrix}, \tag{2-40}$$

where E is the Young's modulus, I_x and I_y are the cross sectional moments of inertia with respect to the *X* and *Y* axes, respectively, and L is the element length. Multiplying $\mathbf{k}_e$ by the *i*-th mode shape ϕ_i we obtain

$$\mathbf{k}_e\phi_i = \frac{12E}{L^3}\begin{bmatrix} I_y & 0 & -I_y & 0 \\ 0 & I_x & 0 & -I_x \\ -I_y & 0 & I_y & 0 \\ 0 & -I_x & 0 & I_x \end{bmatrix}\begin{bmatrix} \alpha_{i,1} \\ \alpha_{i,2} \\ \alpha_{i,3} \\ \alpha_{i,4} \end{bmatrix}, \tag{2-41}$$

$$\mathbf{k}_e\phi_i = \frac{12E}{L^3}\begin{bmatrix} \alpha_{i,1}I_y - \alpha_{i,3}I_y \\ \alpha_{i,2}I_x - \alpha_{i,4}I_x \\ \alpha_{i,3}I_y - \alpha_{i,1}I_y \\ \alpha_{i,4}I_x - \alpha_{i,2}I_x \end{bmatrix}, \tag{2-42}$$

where $\alpha_{i,j}$ is the *j*-th element of the *i*-th eigenvector. If the parameter to be identified is the stiffness, using Eq. 2-42 we can write the elemental identification matrix for the *i*-th mode shape $\theta_{e,i}$ and the vector of unknown parameters $\mathbf{r}_e$ as

$$\theta_{e,i} = \frac{12}{L^3}\begin{bmatrix} \alpha_{i,1}I_y - \alpha_{i,3}I_y \\ \alpha_{i,2}I_x - \alpha_{i,4}I_x \\ \alpha_{i,3}I_y - \alpha_{i,1}I_y \\ \alpha_{i,4}I_x - \alpha_{i,2}I_x \end{bmatrix}, \text{ and } \mathbf{r}_e = [E], \tag{2-43}$$

respectively.

If the parameters to be identified are the moments of inertia of the element, Eq. 2-43 becomes

$$\theta_{e,\,i} = \frac{12E}{L^3}\begin{bmatrix} 0 & \alpha_{i,\,1} - \alpha_{i,\,3} \\ \alpha_{i,\,2} - \alpha_{i,\,4} & 0 \\ 0 & \alpha_{i,\,3} - \alpha_{i,\,1} \\ \alpha_{i,\,4} - \alpha_{i,\,2} & 0 \end{bmatrix}, \text{ and } \mathbf{r}_e = \begin{bmatrix} I_x \\ I_y \end{bmatrix}. \tag{2-44}$$

The number of rows and columns of the elemental identification matrix are equal to the number of degrees of freedom in the element and the number of unknown parameters respectively.

Coordinate Transformation

The matrices θ_e found in Eqs. 2-43 and 2-44 are in local coordinates. These identification matrices can be transformed to global coordinates using a transformation matrix, similar to the approach used in the finite element method. Consider the coordinate transformation

$$\mathbf{k'}_e = \mathbf{T}^T\mathbf{k}_e\mathbf{T}, \tag{2-45}$$

where $\mathbf{T}$ is the coordinate transformation matrix. Post-multiplying both sides of Eq. 2-45 by ϕ_i yields

$$\mathbf{k'}_e\phi_i = \mathbf{T}^T\mathbf{k}_e\mathbf{T}\phi_i \tag{2-46}$$

$$\mathbf{k'}_e\phi_i = \mathbf{T}^T\mathbf{k}_e\phi^{\dagger}{}_i, \tag{2-47}$$

where the vector $\phi^{\dagger}_{i} = \mathbf{T}\phi_i$ is the *i*-th eigenvector in local coordinates. Eq. 2-47 can be written as

$$\mathbf{k}'_e \phi_i = \theta'_{e,i} \mathbf{r}_e , \tag{2-48}$$

where

$$\theta'_{e,i} = \mathbf{T}^T \theta_{e,i} . \tag{2-49}$$

Note that for this transformation the identification matrix $\theta_{e,i}$ is formed with the eigenvectors in local coordinates $(\phi^{\dagger}_{i})$.

Matrix Assembly

Once the element matrices are obtained for all of the elements, the global identification matrix θ_i for the *i*-th mode of vibration is assembled. The dimension of θ_i is $n \times l$, where n is the number of degrees of freedom of the identification model, and l is the number of unknown parameters. The elements of the $\theta_{e,i}$ matrix for the *j*-th element will be placed in the columns corresponding to the unknown parameters of this element and the rows corresponding to the degree of freedom of this element.

To illustrate the process consider the 2DOF structure shown in Fig. 2-4. Assuming that the unknown parameter is Young's modulus, E, the elemental identification matrices are

$$\theta_{1,i} = \frac{12}{L^3}\begin{bmatrix} \alpha_{i,1} I - \alpha_{i,2} I \\ \alpha_{i,2} I - \alpha_{i,1} I \end{bmatrix} \text{ and } \theta_{2,i} = \frac{12}{L^3}\begin{bmatrix} \alpha_{i,2} I - \alpha_{i,3} I \\ \alpha_{i,3} I - \alpha_{i,2} I \end{bmatrix} . \tag{2-50}$$

FIGURE 2-4. 2DOF Structure

The assembled identification matrix is

$$\theta_i = \begin{bmatrix} \alpha_{i,1}I - \alpha_{i,2}I & 0 \\ \alpha_{i,2}I - \alpha_{i,1}I & \alpha_{i,2}I - \alpha_{i,3}I \\ 0 & \alpha_{i,3}I - \alpha_{i,2}I \end{bmatrix}. \tag{2-51}$$

The first column corresponds to the unknown parameter E_1, and the second parameter corresponds to the parameter E_2. The rows correspond to each degree of freedom ($\alpha_{i,1}$, $\alpha_{i,2}$, $\alpha_{i,3}$).

The degree of freedom $\alpha_{i,1}$ corresponds to the base of the structure. This degree of freedom is included in the elemental and general identification matrices. In a later section we will see how to consider boundary conditions.

Constraint Equations

Constraints can be considered to include relationship between degrees of freedom. A common application of constraint equations is rigid links. These elements rigidly connect a slave and a master node. The degrees of freedom of the slave node will depend only on

the displacement and rotation of the master node. In the finite element method constraint equations are applied to the stiffness matrix using the equation

$$\mathbf{K}' = \mathbf{Q}^T\mathbf{K}\mathbf{Q} \tag{2-52}$$

where $\mathbf{Q}$ is the constraint equation matrix, and $\mathbf{K}'$ is the stiffness matrix after the constraint equations are applied. Equation 2-52 is of the same form of Eq. 2-45. Thus, similar to the transformation of coordinates for the identification matrix, the constraint equations can be written as

$$\theta'_i = \mathbf{Q}^T\theta_i \tag{2-53}$$

where the matrix θ_i is constructed with the eigenvector

$$\phi'_i = \mathbf{Q}\phi_i. \tag{2-54}$$

For a 3D rigid element, the relation between the master and slave degrees of freedom is

$$\begin{bmatrix} u_m \\ u_s \end{bmatrix} = \mathbf{Q}\begin{bmatrix} u_m \end{bmatrix}, \tag{2-55}$$

where u_m and u_s are the degrees of freedom for the master and slave nodes. The constraint matrix is

$$\mathbf{Q} = \begin{bmatrix} \mathbf{I} \\ \mathbf{q} \end{bmatrix}, \tag{2-56}$$

where $\mathbf{I}$ is the identity matrix of appropriate dimensions, and

$$\mathbf{q} = \begin{bmatrix} 1 & 0 & 0 & 0 & dz & -dz \\ 0 & 1 & 0 & -dz & 0 & dx \\ 0 & 0 & 1 & dy & -dx & 0 \\ 0 & 0 & 0 & 1 & 0 & 0 \\ 0 & 0 & 0 & 0 & 1 & 0 \\ 0 & 0 & 0 & 0 & 0 & 1 \end{bmatrix}. \tag{2-57}$$

Boundary Conditions

Boundary conditions are imposed by eliminating the rows of the θ_i matrix corresponding to the boundary degree of freedom. Also, the components of the mode shape associated with a boundary degree of freedom should be equal to zero. Considering the structure shown in Fig. 2-4, boundary conditions are applied by eliminating the first row of the identification matrix in Eq. 2-51 and by making $\alpha_{i,1}$ equal to zero. The resulting identification matrix is

$$\theta_i = \begin{bmatrix} \alpha_{i,2} I & \alpha_{i,2} I - \alpha_{i,3} I \\ 0 & \alpha_{i,3} I - \alpha_{i,2} I \end{bmatrix}. \tag{2-58}$$

Known Parameters

When information regarding specific structural members is available (e.g., by visual inspection or any other means) this information can be incorporated into the methodology to reduce the number of unknown parameters and improve the accuracy of the results. The stiffness matrix can be written as

$$\mathbf{K} = \mathbf{K}_u + \mathbf{K}_k, \tag{2-59}$$

where $\mathbf{K}_u$ is the stiffness matrix for the elements with unknown parameters and $\mathbf{K}_k$ is the stiffness matrix of the elements with known parameters. Inserting Eq. 2-59 into Eq. 2-33 we obtain

$$(\mathbf{K}_u + \mathbf{K}_k)\phi_i = \lambda_i \mathbf{M}\phi_i . \tag{2-60}$$

Rearranging this, and including Eq. 2-34 yields

$$\theta_i \mathbf{r} = (\lambda_i \mathbf{M} - \mathbf{K}_k)\phi_i . \tag{2-61}$$

Including all the identified natural frequencies and mode shapes, the matrix Γ in Eq. 2-39 is

$$\Gamma = \begin{bmatrix} (\mathbf{M}\lambda_1 - \mathbf{K}_k)\phi_1 \\ (\mathbf{M}\lambda_2 - \mathbf{K}_k)\phi_2 \\ \vdots \\ (\mathbf{M}\lambda_m - \mathbf{K}_m)\phi_m \end{bmatrix} . \tag{2-62}$$

Implementation

The methodology described in this section was implemented in Matlab as a part of a finite element toolbox. Full 3D identification models with bar elements can be created with this toolbox using additional elements such as rigid links and lumped masses. The toolbox was programmed using object oriented techniques, allowing for the inclusion of new elements, such as shells and bricks in a systematic way.

2.3 Indices for damage identification

In the literature several indices exist to identify and locate damage in a structure. Although these indices are not based on the identification of physical parameters of the structure, they may be used to locate damage in the structure by identifying changes in the properties of the structure. One advantage of these techniques is that a model of the structure is not needed to identify damage in the structure. These indices are used in this dissertation to compare the mode shapes of the structure in the sensitivity studies presented in Chapter 4.

2.3.1 Modal Assurance Criterion

Suppose that the mode shapes of a structure are identified from two tests a and b. The MAC is used to quantify the correlation between two mode shapes and is defined as

$$\mathrm{MAC} = \frac{\left\{ \sum_{j=1}^{n} {}^{a}\phi_{i,j}\, {}^{b}\phi_{i,j} \right\}^2}{\left(\sum_{i=1}^{n} ({}^{a}\phi_{i,j})^2 \right)\left(\sum_{i=1}^{n} ({}^{b}\phi_{i,j})^2 \right)} \tag{2-63}$$

where ${}^{a}\phi_{i,j}$ is the j-th coordinate of the i-th mode shape of measurement a, ${}^{b}\phi_{i,j}$ is the j-th coordinate of the i-th mode shape of measurement b, and n is the number of degrees of freedom. Note that the mode shapes between measurements a and b should be the same (*e.g.*, first translational mode shape in the transverse direction).

If the two mode shapes are aligned, the MAC will equal one. If they are not linearly correlated, the MAC factor will equal zero. Lower values of MAC for the same mode shape between measurements a and b indicates that the structure has changed, possibly

due to damage. Noise in the measurements, structural nonlinearities, and poor identification of the mode shapes are sources of error for the MAC factors. Marwala and Heyns [63] reported that MAC values should not be used for modes that are closely spaced (*e.g.*, such as those often found in flexible structures).

Damage in complex structures can cause the order of the modes to change. MAC factors can also be used to identify shifts in the order of mode shapes between two measurements. This is most evident in the case of cable-stayed bridges where the natural frequencies are closely spaced and damage in the structure is likely to cause shifting in the mode shapes.

2.3.2 Mode Orthogonality

It is also possible to determine the orthogonality of two mode shapes if the mass of the system is known or can be closely estimated. For mode shapes that are normalized with respect to the mass, we know [23]

$$\mathbf{\Phi}^T\mathbf{M}\mathbf{\Phi} = \mathbf{I}, \tag{2-64}$$

where $\mathbf{I}$ is the identity matrix, $\mathbf{\Phi}$ is the matrix of mode shapes and $\mathbf{M}$ is the mass matrix. When comparing the same mode for two different measurements of the structure, Eq. 2-64 yields

$$b = \phi_u^T\mathbf{M}\phi_d, \tag{2-65}$$

where ϕ_u is the mode shape of the undamaged structure, and ϕ_d is the mode shape of the potentially damaged structure. If the structure has no damage the value of b is close to one, indicating that the mode shape has not changed.

The property of modal orthogonality was found to be very effective to sort the mode shapes of damaged structure to match the mode shapes of the undamaged structure. This technique facilitates the comparison of damaged and undamaged structures to be discussed in chapter 4. Here, a modification of Eq. 2-65 is used

$$\mathbf{b} = \Phi_u^T \mathbf{M} \phi_i . \tag{2-66}$$

The vector $\mathbf{b}$ will have n elements, where n is the number of mode shapes in the matrix Φ_u^T. The element of $\mathbf{b}$ closest to one will identify the mode in Φ_u^T corresponding to ϕ_i.

2.4 Summary

The two step SHM methodology proposed in this dissertation was discussed in this chapter. In this methodology, NExT obtains free response records from ambient vibration tests, and ERA identifies the modal parameters from the free response data. The ERA was originally developed to identify a state space representation of a system from frequency response functions. The use of ERA with free response data is presented indicating that the matrices **A** and **C** of the state space representation can be obtained from the free response records. Modal parameters of the structures can be identified from these two matrices.

In the proposed methodology the least squares solution of the eigenvalue problem is used for the identification of structural parameters. The procedure for the implementation of this methodology based on finite element meshes was presented in this chapter. This includes the calculation of elemental identification matrices, coordinate transformation, matrix assembly, and application of constraint equations and boundary conditions. This procedure simplifies the implementation of the methodology to large structures.

In the final portion of this chapter the description of the COMAC and the use of mode orthogonality for mode sorting are presented. When damage occurs in a structure the mode of vibration can switch places (i.e. the 9th mode becomes the 8th mode). These methods are used in the following chapters to sort the modes of the structure, allowing the comparison of modes of vibration between the damaged and undamaged states.

Chapter 3

Verification through Benchmark Implementation

During the past several years benchmark problems have become a very popular topic in structural control and structural health monitoring. The main objective of a benchmark problem is to permit direct comparison of different techniques, methodologies, sensors and/or devices through a testbed problem widely available to the research community. In 1999 the American Society of Civil Engineering (ASCE) with the International Association of Structural Control (IASC) formed a task group for the definition of the first benchmark problem in structural health monitoring [52]. The group defined a simple problem that could serve as testbed for the research community. In May of 2000 the first session dedicated to the benchmark problem was held at the 14th Engineering Mechanics Conference in Austin, Texas. At this conference several solutions for the benchmark problem were presented including the work of Katafygiotis *et al.* [53], Dyke *et al.* [33], Au *et al*. [1], Bernal and Gunes [8], and Corbin *et al*. [26]. Although the first benchmark problem started as a simple exercise, the complexity of the problem has grown over time. To date, a total of seven sessions at different conferences have been dedicated to the different stages of the benchmark problem including two sessions at the ASME-ASCE Joint Mechanics and Materials Conference in San Diego, California (June 27-29, 2001), one session at the 3rd International Workshop on Structural Health Monitoring (September 12-14 2001), one session at the 15th ASCE Engineering Mechanics Conference in New York (June 2-5, 2002), one session at the IMAC XXI Conference in Orlando, Florida (February 3-6, 2003), and a session at the 16th ASCE Engineering Mechanics Conference in Seattle, Washington (July 16-18, 2003).

The methodology described in this dissertation has been applied to the different stages of the benchmark problem, and this chapter presents a summary of that work.

3.1 Benchmark Problem Description

The benchmark problem has been divided into a numerical phase and an experimental phase. In the numerical phase, numerical models of a structure are used to compute acceleration records. Damage in the structure is determined using these dynamic responses. In the experimental phase the acceleration records are obtained from a physical model. Different excitation cases and damage patterns are considered.

More information about the activities of the task group on structural health monitoring can be found at the IASC-ASCE task group in SHM benchmark problems web page at <http://wusceel.cive.wustl.edu/asce.shm>.

3.1.1 Benchmark Structure

The benchmark structure selected is the 2 bay by 2 bay, 4-story steel structure scaled 1:3, located at the Earthquake Engineering Laboratory at the University of British Columbia, Canada (Figure 3-1). Although the numerical phase of the benchmark problem was based on numerical models of the structure, this structure was selected by the task group for its availability. The structure has a square plan of width 2.5m and has a height of 3.6m. The beams and columns are steel, hot-rolled grade 300W sections with properties given in Table 3-1 [52]. The floor masses varied through the different phases of the benchmark problem.

a. Benchmark Structure

b. Diagonal Members

FIGURE 3-1. Benchmark Structure

TABLE 3-1. Properties of the Benchmark Structure

Property	Columns	Beam	Braces
Section Name	B100X9	S75X11	L25X25X3
Area (m^2)	1.133×10^{-3}	1.43×10^{-3}	1.41×10^{-4}
Moment of Inertia in the strong dir. (m^4)	1.97×10^{-6}	1.22×10^{-6}	0
Moment of Inertia in the weak dir. (m^4)	6.64×10^{-7}	2.49×10^{-7}	0
St. Venant torsion constant (m^4)	8.01×10^{-9}	3.82×10^{-9}	0

3.2 First Numerical Phase

Two numerical models were developed based on the benchmark structure. The first is a 12 DOF model that allows motion at each floor in the horizontal plane, and rotations with respect to the vertical axis. The translational stiffness of this model was modeled as 106.6 MN-m in the strong direction of the structure and 67.9 MN-m in the weak direction. The second model has a total of 120 DOF. The floor nodes of the second model are restrained to have the same horizontal rotation and in-plane rotation (i.e., a rigid floor). Both models

had a total mass of 3200 kg in the first floor, 2400 kg on the second and third floor, and either 1600 kg or 1700 kg on the last floor depending on the case being simulated. The natural frequencies of the two models without damage are shown in Table 3-2 as reported by Johnson *et al*. [52]. The type of motion, either translation in the *X* or *Y* axis, or rotation with respect to the *Z* axis, is also indicated.

TABLE 3-2. Natural Frequencies for the Benchmark Models

12 DOF	120 DOF	12 DOF	120 DOF	12 DOF	120 DOF
9.41 *Y*	8.20 *Y*	32.07 *X*	24.24 *X*	48.68 *X*	39.73 *X*
11.79 *X*	8.53 *X*	38.85 *Y*	35.58 *Y*	60.60 *X*	55.16 *X*
16.53 θ	13.95 θ	45.17 θ	39.05 θ	68.64 θ	60.75 θ
25.60 *Y*	22.54 *Y*	48.37 *Y*	39.73 *X*	85.51 θ	79.46 θ

X: Translational mode along the *X* axis.
Y: Translational mode along the *Y* axis.
θ : Rotational mode about the *Z* axis.

These two models were used for the first and second numerical phases of the benchmark problem. The goal of the first phase numerical study was to study the effect of noise in the sensors and the effects of modeling errors in the SHM methodologies. In this phase damage was induced in the structure by removing the braces in the structure or by reducing the stiffness of beam column connections. Although removal of the braces causes a severe reduction in the stiffness of the structure, the committee agreed that this was a good starting point for the benchmark problem. The structure was excited with band limited white noise with a 100Hz cutoff frequency. Four acceleration records per floor were available, two in the *X* direction, and two in the *Y* direction, for a total of sixteen accelerometers in the structure. A white noise with a root mean square (RMS) amplitude of 10% of the RMS of the roof acceleration was added to the acceleration records to simulate noise in the sensors.

Six simulation cases and 5 damage cases were studied in this phase. In all cases a 12 DOF identification model was used. This approach produced some modeling errors when the

acceleration records were calculated using the 120 DOF structural model. Case I was the simplest. Here the 12 DOF structural model was used to calculate the acceleration in the structure which was excited only in the weak direction. Case 2 was the same as case 1, but used the 120 DOF structural model. Case 3 considered the excitation to act only at the roof using the 12 DOF structure. Cases 4 and 5 considered the structure to have some asymmetry. In this case the center of mass at the roof was different than the center of inertia, and excitation was used in both directions. In case 4 the 12 DOF structural model was used, and in case 5 the 120 DOF model was used. Case 6 was the same as case 5, but a limited number of sensors was available.

Five damage patterns were studied in this phase. The first damage pattern assumed that all the braces in the first floor of the structure were removed. All the braces were removed in the first and third floor for the second damage pattern. For damage pattern three only one brace was removed, in the first story. An additional brace was removed in the third story to form damage pattern four. Finally, damage pattern five was the same as four with the addition of a reduction in the stiffness of the connections between a column and a beam at the first level.

This initial numerical phase of the benchmark problem has been extensively studied in references [12, 15, 33] using the methods described earlier in this dissertation. It was found that the methods are not sensitive to noise in the sensors. It was also found that modeling errors have some effect on the methodology, but for this particular structure it was not important. Additionally, an iterative procedure was developed for the case were only a limited number of sensors (on the 2nd and 4th floors) were available. In the referenced work a parameter study of the effect of the number of points used in the calculation of the cross spectral density function was also presented.

3.3 Second Numerical Phase

After the first numerical phase, the committee decided to test the physical model. In the summer of 2000 a series of tests were performed at the Earthquake Engineering Laboratory at the University of British Columbia [30, 32]. After analyzing the data collected in the tests, members of the committee decided that before using experimental data more studies based on numerical simulations were needed. The decision was made to study some of the difficulties presented with the experimental data in a more controlled environment. Thus, a second numerical phase of the SHM benchmark problem was proposed.

The focus of this second numerical phase was the investigation of the differences between the model considered to be the "real structure" and the identification model. Although modeling errors existed in the first phase between the 12 DOF identification structure and the 120 DOF structural model (or "real structure"), the structure was too perfect. For example, the center of mass coincided with the center of inertia, all of the beams had exactly the same stiffness, and all of the floors had the same mass which was known by the participants. Thus, for the second phase numerical problem, the committee decided to use the 120 DOF structural model with the following modifications [6]: the mass of each floor was multiplied by uniformly distributed random coefficient in the range [0.9, 1.1]; the position of the center of mass of each floor was multiplied by a uniformly distributed random coefficient in the range [-0.25m, 0.25m]; the axial stiffness of the braces was multiplied by a uniformly distributed random coefficient in the range [0.9, 1.1]; the moment connection between the beams and the columns was modeled as a linear rotational spring. The stiffness of these springs was selected to match the first natural frequency of the benchmark structure obtained experimentally, and it is multiplied by a uniformly distributed random coefficient in the interval [0.75, 1.25]. The uniformly distributed random coefficients for each structural parameter were selected once and were held constant throughout the different simulations.

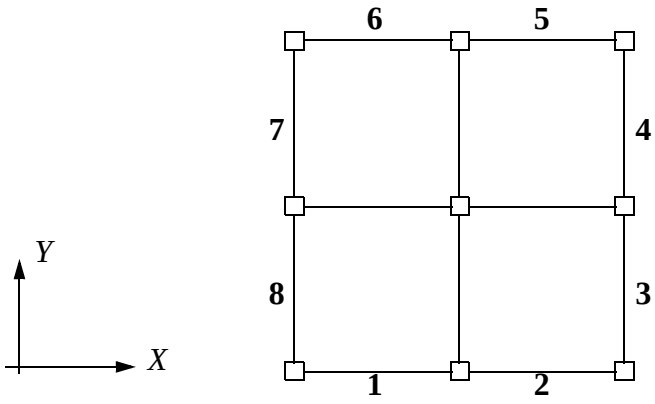

FIGURE 3-2. Element Numbers (Diagonals)

As in the first phase, the excitation was band-limited white noise applied to each floor in the structure. Noise in the sensors was also considered by including a broadband random signal with an amplitude equal to 10% of the RMS of the roof acceleration.

Two damage scenarios were proposed in the benchmark problem [6], and the results of the first case scenario are presented here [13]. Damage was simulated by decreasing the stiffness of the braces in the structure. As in the first phase, the mass was held constant. The first damage pattern considered a reduction of 50% in the stiffness in two of the braces at the first floor (at locations 1 and 6, Fig. 3-2). These braces were located on opposite sides of the structure in the strong (*X*) direction. A reduction of 25% in the same members was considered for the second damage pattern. The third damage pattern considers a 50% reduction in the stiffness of two braces at the first floor (at locations 1 and 6), and a 25% reduction of the same two braces at the third floor.

3.3.1 Identification Models

Two different identification models were employed for structural parameter identification. The first identification model is a shear model with only 8 DOF (including displacement in the *X* and *Y* directions for each floor) as shown in Fig. 3-3a Using this model one can

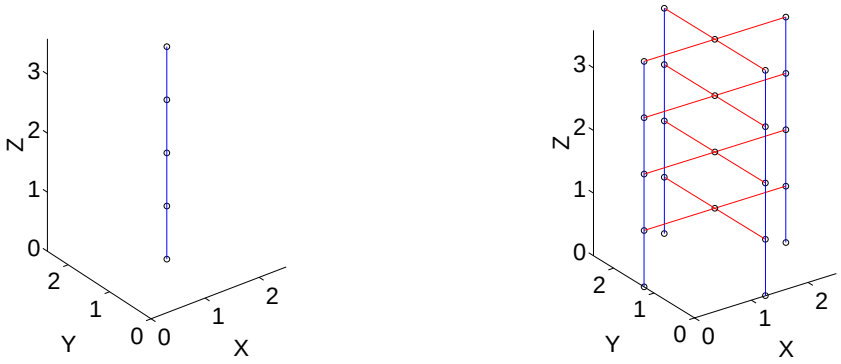

(a) 8 DOF Model **(b) 12 DOF Model**

FIGURE 3-3. Structural Identification Models

identify the floor and direction affected by the damage, indicating its existence and partial information on its location. The second model is shown in Fig. 3-3b. This model has 12 DOF (the 8 DOF model, plus rotations about the vertical axis) and can be used to obtain better information on the location of the damage. Specifically, the damaged side can be determined. Here, four elements are used at each floor. Each element is connected to a central lumped mass using a rigid link.

Because many DOF are condensed out in the identification model, each element represents contributions from a portion of the structural model (or “real” structure), rather than being exclusively influenced by a single member of the physical structure, and the identified damage cannot be attributed to a single member but, rather, to one or more of several members in that particular portion of the structure. Figure 3-4 shows the members from the experimental structure that influence a particular element of the identification model. Note that some members of the physical structure affect only one corresponding element of the identification model, while others contribute stiffness to several elements of the model.

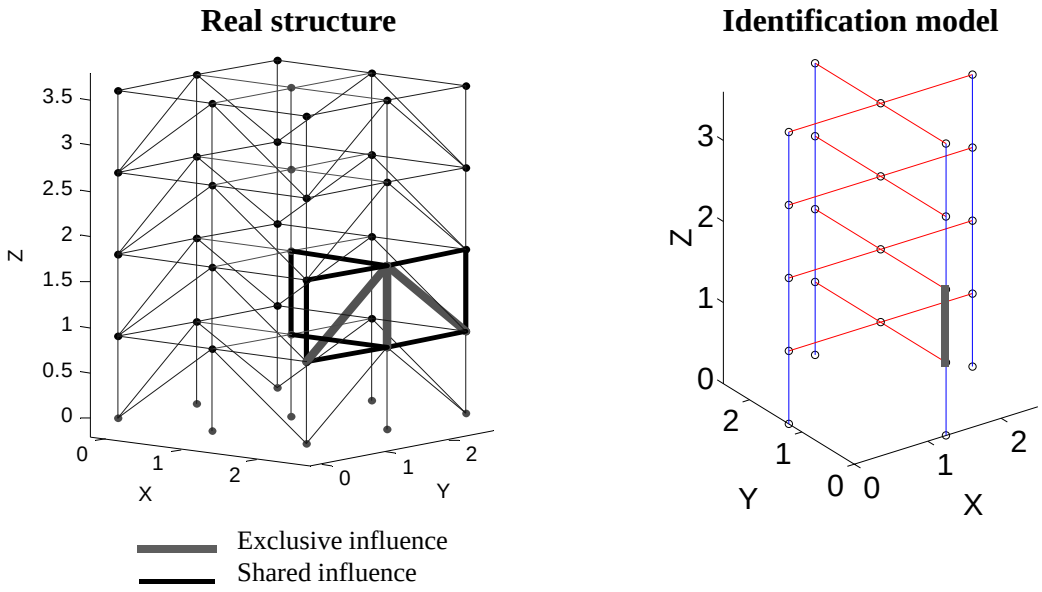

FIGURE 3-4. Association Between Members of the Structure and the Identification Model

3.3.2 Benchmark Results

To identify the damaged floors, the damage SHM methodology is applied in each direction separately using the 8 DOF model. Four acceleration records are available for each floor, 2 in the *X* direction, and 2 in the *Y* direction. In each direction the translational accelerations were calculated as

$$\mathbf{a}_x(t) = \frac{\mathbf{a}_{x1}(t) + \mathbf{a}_{x2}(t)}{2}, \text{ and } \mathbf{a}_y(t) = \frac{\mathbf{a}_{y1}(t) + \mathbf{a}_{y2}(t)}{2} \quad (3\text{-}1)$$

where $\mathbf{a}_{x1}$ and $\mathbf{a}_{x2}$ are vectors of acceleration obtained for the *X* direction on opposite sides of the structure, and $\mathbf{a}_{y1}$ and $\mathbf{a}_{y2}$ are the acceleration records obtained for opposite sides in the *Y* direction.

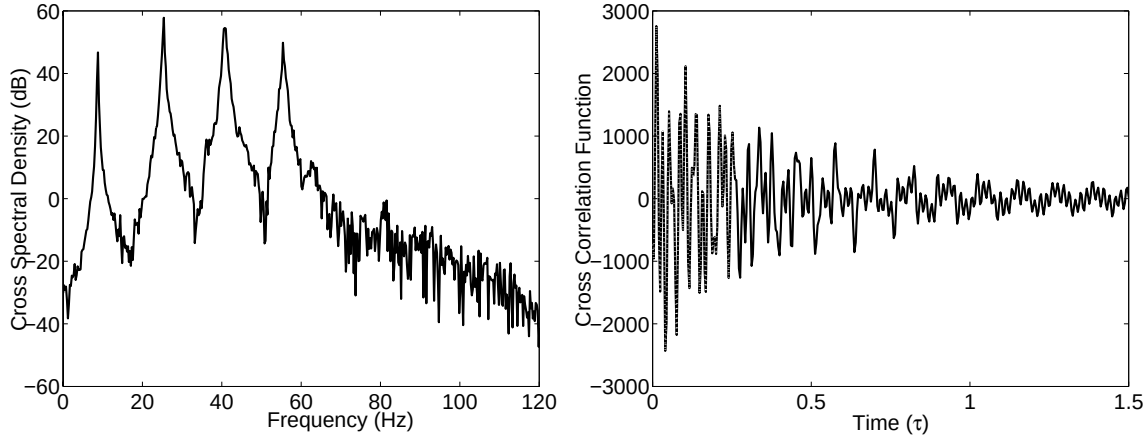

(a) Cross spectral density function **(b) Cross correlation function**

FIGURE 3-5. Cross spectral density and cross correlation functions

For calculation of the cross correlation functions, a boxcar window of 1024 points with 75% overlapping was used. The acceleration of the roof of the structure was selected as the reference channel for calculating the cross spectral density functions. This channel was selected because it is far from any of the nodes of the mode shapes and it will contain information of the four natural frequencies about the structure. Figure 3-5 shows a typical cross spectral density function and the corresponding cross correlation function from the data. The four modes of the structure can be easily identified as peaks in this plot.

A Hankel matrix width 150 rows and 30 columns using a total of 66 time samples of the cross correlation function was used for implementation of the ERA. The dotted portion of the cross correlation function in Figure 3-5b corresponds to the data used to form the Hankel matrix. Figure 3-6 shows a typical plot of the singular values of the Hankel matrix. A drop is observed after the 8th singular value indicating that the structure has 4 modes of vibration (8 poles).

The resulting natural frequencies are shown in Table 3-3. Figure 3-7 shows the identified mode shapes for the healthy structure in the strong (*X*) direction. The natural frequencies

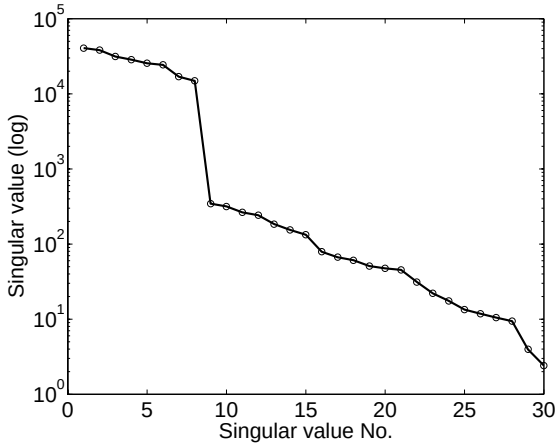

FIGURE 3-6. Singular Values

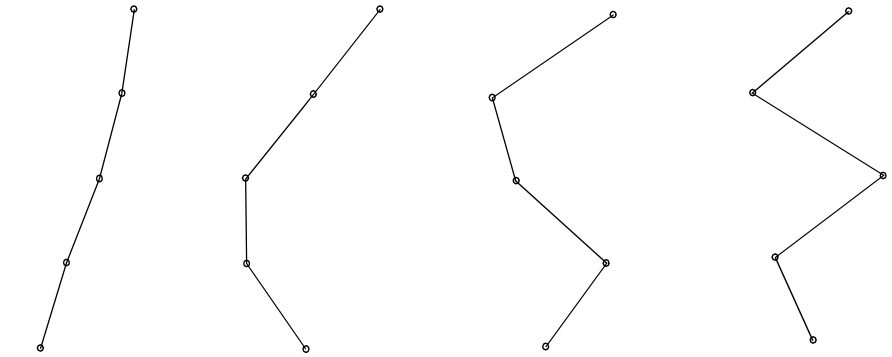

FIGURE 3-7. Identified Mode Shapes (*X*-direction, undamaged)

TABLE 3-3. Identified Natural Frequencies

Case	***X* - direction**				***Y* - direction**			
	ω_1 **(Hz)**	ω_2 **(Hz)**	ω_3 **(Hz)**	ω_4 **(Hz)**	ω_1 **(Hz)**	ω_2 **(Hz)**	ω_3 **(Hz)**	ω_4 **(Hz)**
Healthy	8.78	25.34	40.76	55.50	8.30	23.16	36.12	46.27
Damage 1	8.35	24.52	40.34	55.40	8.30	23.16	36.12	46.26
Damage 2	8.71	24.93	40.53	55.45	8.30	23.16	36.12	46.27
Damage 3	8.31	24.17	40.31	54.52	8.30	23.16	36.11	46.26

in the weak (*Y*) direction of the structure did not change during the various damage cases, indicating no damage occurred which affected the dynamics in this direction. However, the identified natural frequencies in the strong (*X)* direction changed for each damage case.

For each damage case the loss of stiffness at each floor, as compared to the healthy structure, was calculated and is shown in Table 3-4. Here the loss of stiffness is defined as

$$\Delta \mathbf{k} \;=\; 100 \times \frac{\mathbf{k}_{\text{undamaged}} - \mathbf{k}_{\text{damaged}}}{\mathbf{k}_{\text{undamaged}}}. \tag{3-2}$$

It is clear from these results that damage occurs on the first floor in the strong direction in the first and second damage cases, and on the first and second floor in the third damage case. The loss in identified stiffness in the first floor for the second damage case is approximately half the loss of stiffness in the second and third cases, consistent with the damage induced as described in the benchmark problem statement. No damage is found in the *Y* direction. Relatively negligible stiffness variations are observed in the undamaged floors, due to noise included in the numerical simulations and modeling errors (0.29% maximum).

Further examination of the strong direction of the structure to more precisely locate the damage was performed using the 12 DOF model. This more refined model allowed for determination of the side(s) of the structure that were damaged. For this analysis the

TABLE 3-4. Stiffness Reduction (8 DOF model)

Case	***X* - direction**				***Y* - direction**			
	$\Delta\mathbf{k}_1$ **(%)**	$\Delta\mathbf{k}_2$ **(%)**	$\Delta\mathbf{k}_3$ **(%)**	$\Delta\mathbf{k}_4$ **(%)**	$\Delta\mathbf{k}_1$ **(%)**	$\Delta\mathbf{k}_2$ **(%)**	$\Delta\mathbf{k}_3$ **(%)**	$\Delta\mathbf{k}_4$ **(%)**
Damage 1	13.29	-0.33	0.17	-0.06	0.18	-0.18	0.04	-0.06
Damage 2	6.44	0.11	-0.11	0.16	0.10	-0.08	0.02	-0.03
Damage 3	12.75	-0.34	7.11	0.02	0.29	-0.27	0.07	-0.11

acceleration records were not averaged using Eq. 3-1. Table 3-5 provides the identified loss in stiffness in the left and right frames. It was found that the stiffness loss is similar in both frames, which agrees with the benchmark problem statement. For the first case a loss of stiffness of 13.24% and 13.66% was found at the first floor. These values agree with the 13.29% stiffness loss found with the 8 DOF model. Similar results are observed in the other damage cases.

TABLE 3-5. Stiffness Reduction (12 DOF model - *X* direction)

Case	$\Delta\mathbf{k}_{1L}$ (%)	$\Delta\mathbf{k}_{1R}$ (%)	$\Delta\mathbf{k}_{2L}$ (%)	$\Delta\mathbf{k}_{2R}$ (%)	$\Delta\mathbf{k}_{3L}$ (%)	$\Delta\mathbf{k}_{3R}$ (%)	$\Delta\mathbf{k}_{4L}$ (%)	$\Delta\mathbf{k}_{4R}$ (%)
Damage 1	13.24	13.66	0.29	-0.95	1.02	-0.76	-0.13	0.02
Damage 2	6.38	6.67	0.45	-0.23	0.41	-0.68	0.13	0.20
Damage 3	12.64	13.05	-0.08	-0.56	7.95	6.16	0.10	-0.02

L = Left side frame; R = Right side frame

In the case of limited sensors (2nd and 4th floor only), the ϕ_i vector cannot be completely defined in the modal identification step. In this case the following iterative procedure can be used: *i*) assume a vector of stiffnesses $\mathbf{k}_i$; *ii*) using $\mathbf{k}_i$ and the approximated mass matrix, calculate the theoretical natural frequencies and mode shapes; *iii*) fix the known parts of the mode shapes using the data from NExT and ERA; *iv*) calculate a new stiffness $\mathbf{k}_s$ using the least squares solution of the eigenvalue problem (see chapter 2) with the identified natural frequencies and the fixed mode shapes; *v*) obtain $\Delta\mathbf{k} = \mathbf{k}_s - \mathbf{k}_i$; and, *v*i) calculate an updated $\mathbf{k}_{i+1} = \mathbf{k}_i + \Delta\mathbf{k}$ and iterate (go to step *ii*). The solution is obtained when $\Delta\mathbf{k}$ reaches an appropriate convergence level defined by the user. Figure 3-8 shows a flow diagram of the iterative procedure. Although this methodology is not guaranteed to converge, it was found effective in the cases that were studied.

The natural frequencies obtained were approximately equal to those obtained with the full set of sensors. The maximum variation of these values with respect to the values shown in

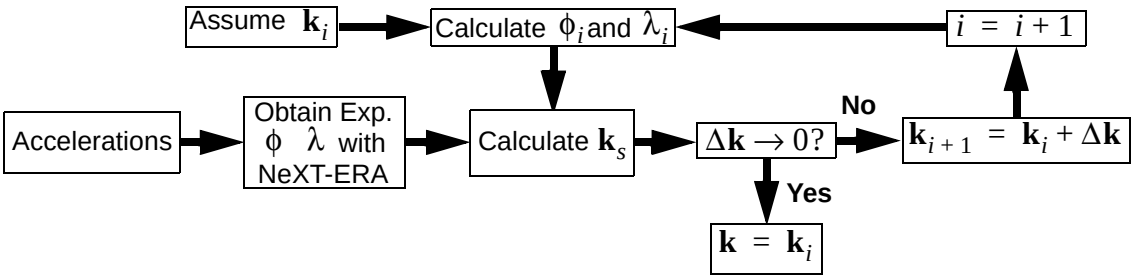

FIGURE 3-8. Iterative Procedure

TABLE 3-6. Stiffness Reduction (8 DOF model, limited sensors)

Case	*X* - direction				*Y* - direction			
	$\Delta\mathbf{k}_1$ (%)	$\Delta\mathbf{k}_2$ (%)	$\Delta\mathbf{k}_3$ (%)	$\Delta\mathbf{k}_4$ (%)	$\Delta\mathbf{k}_1$ (%)	$\Delta\mathbf{k}_2$ (%)	$\Delta\mathbf{k}_3$ (%)	$\Delta\mathbf{k}_4$ (%)
Damage 1	15.03	-0.98	1.19	-0.40	-0.19	0.03	-0.02	0.06
Damage 2	7.28	-0.52	0.78	-0.15	-0.06	0.01	-0.01	0.03
Damage 3	8.46	0.15	9.07	0.76	-0.35	0.11	-0.09	0.09

TABLE 3-7. Stiffness Reduction (12 DOF model - *X* direction limited sensors)

Case	$\Delta\mathbf{k}_{1L}$ (%)	$\Delta\mathbf{k}_{1R}$ (%)	$\Delta\mathbf{k}_{2L}$ (%)	$\Delta\mathbf{k}_{2R}$ (%)	$\Delta\mathbf{k}_{3L}$ (%)	$\Delta\mathbf{k}_{3R}$ (%)	$\Delta\mathbf{k}_{4L}$ (%)	$\Delta\mathbf{k}_{4R}$ (%)
Damage 1	8.90	9.80	1.14	1.64	0.64	-1.16	0.64	0.59
Damage 2	3.94	5.08	0.70	0.69	0.37	-0.46	0.12	0.42
Damage 3	5.94	6.81	2.83	3.37	5.51	4.07	1.40	1.19

L = Left side frame; R = Right side frame

Table 3-3 is 0.65%. Table 3-6 shows the identified stiffness loss using the 8 DOF identification model. The lack of complete mode shapes increased the errors in the stiffnesses obtained at the undamaged floors (from 0.34% to 1.19%). Nevertheless, the method accurately identified the damage in each of the 3 damage cases. Table 3-7 shows the stiffness loss in the strong (*X*) direction for the 12 DOF model. The results obtained with this model agree with the results obtained with the 8 DOF model. With this identification model the errors shown in the undamaged elements also increased, especially in case 3 where the identified loss in stiffness in the second floor elements

might be interpreted as false damage. However, simultaneously using the information obtained using both identification models, one could determine all three damage cases.

3.3.3 Blind Test

A blind case, called "phase IIe" was created in the second phase of the numerical benchmark problem including two blind damage patterns. Dr. Lam at the Hong Kong University of Science and Technology selected damage patterns which were unknown to the benchmark participants [59]. The results obtained by the different groups participating in the blind case, as well as the correct solution, were presented at the XXI IMAC Conference in Kissimmee, Florida (February 3-6, 2003).

Table 3-8 shows the identified natural frequencies for the blind cases. No change is present in the *Y* direction of blind pattern 1, indicating that this direction is free of damage. Damage was identified in the second floor, *X* direction for blind pattern 1 using the 8 DOF structure. The identification procedure indicated damage in the first floor in the *X* direction, and the third and fourth floor in the *Y* direction for blind pattern 2. As expected the methodology did not identify any damage for the *Y* direction of blind pattern 1.

TABLE 3-8. Identified Natural Frequencies (Blind Case)

Case	***X* - direction**				***Y* - direction**			
	ω_1 **(Hz)**	ω_2 **(Hz)**	ω_3 **(Hz)**	ω_4 **(Hz)**	ω_1 **(Hz)**	ω_2 **(Hz)**	ω_3 **(Hz)**	ω_4 **(Hz)**
Healthy	8.78	25.32	40.85	55.49	8.37	23.19	36.06	46.12
Blind 1	8.60	25.32	40.46	55.19	8.37	23.19	36.06	46.12
Blind 2	8.67	25.14	40.76	55.46	8.24	22.54	35.20	45.12

TABLE 3-9. Stiffness Reduction (8 DOF Model - Blind Case)

Case	***X* - direction**				***Y* - direction**			
	$\Delta\mathbf{k}_1$ **(%)**	$\Delta\mathbf{k}_2$ **(%)**	$\Delta\mathbf{k}_3$ **(%)**	$\Delta\mathbf{k}_4$ **(%)**	$\Delta\mathbf{k}_1$ **(%)**	$\Delta\mathbf{k}_2$ **(%)**	$\Delta\mathbf{k}_3$ **(%)**	$\Delta\mathbf{k}_4$ **(%)**
Blind 1	0.05	3.51	0.09	0.47	-0.01	0.00	-0.00	-0.00
Blind 2	2.96	-0.22	0.12	-0.02	0.33	-1.70	6.78	8.82

The 12 DOF identification model is used to determine the side where damage occurred. Table 3-10 shows the results for the *X* direction. Here a loss of stiffness of 8.92% was identified on the left side of the second floor for blind pattern 1. The left side of the first floor presented a loss of stiffness of 5.58% for blind pattern 2. Table 3-11 shows the identification of the different frames for the *Y* direction. A loss of 12.27% in the stiffness of the left side of the third floor and 19.53% was identified in blind pattern 2. Note that in this table the left side of the first floor presented a loss of 5.49%, but this was ruled out as a false positive because the 8 DOF model did not present any damage in the first floor. This demonstrates the main advantage of using different identification models for the same structure. This work was presented at the IMAC conference [13], and the results agreed with the numerical solution of the problem [59].

3.4 Experimental Phase

Following the studies done with the numerical models, the committee decided to again test the physical structure. As in the numerical phases, damage was simulated by removing bracing within the structure or loosening bolts connecting beams to columns. Three sources of excitation were considered: ambient vibrations, impact hammer tests, and electrodynamic shaker tests. Accelerometers placed throughout the structure provided

TABLE 3-10. Stiffness Reduction (12 DOF Model - *X* Direction - Blind Case)

Case	$\Delta\mathbf{k}_{1L}$ (%)	$\Delta\mathbf{k}_{1R}$ (%)	$\Delta\mathbf{k}_{2L}$ (%)	$\Delta\mathbf{k}_{2R}$ (%)	$\Delta\mathbf{k}_{3L}$ (%)	$\Delta\mathbf{k}_{3R}$ (%)	$\Delta\mathbf{k}_{4L}$ (%)	$\Delta\mathbf{k}_{4R}$ (%)
Blind 1	-0.03	0.28	8.92	-2.14	0.50	0.52	0.70	0.80
Blind 2	5.58	1.97	-0.01	-1.48	0.01	0.47	-0.16	-1.32

L = Left side frame; R = Right side frame

TABLE 3-11. Stiffness Reduction (12 DOF Model - *Y* Direction - Blind Case)

Case	$\Delta\mathbf{k}_{1L}$ (%)	$\Delta\mathbf{k}_{1R}$ (%)	$\Delta\mathbf{k}_{2L}$ (%)	$\Delta\mathbf{k}_{2R}$ (%)	$\Delta\mathbf{k}_{3L}$ (%)	$\Delta\mathbf{k}_{3R}$ (%)	$\Delta\mathbf{k}_{4L}$ (%)	$\Delta\mathbf{k}_{4R}$ (%)
Blind 1	0.00	0.14	0.07	-0.12	-0.05	0.09	0.06	0.04
Blind 2	5.49	-4.69	-2.10	0.49	12.27	1.74	-1.59	19.53

L = Left side frame; R = Right side frame

measurements of the structural responses. The data recorded during the testing of the UBC structure, a video of the experiment, and a complete description of the experimental setup are available on the ASCE Structural Health Monitoring Task Group's web page [44].

3.4.1 Experimental Setup

The structure was positioned so that the strong side is parallel to the North-South direction as shown in Fig. 3-1. In each bay the bracing system consists of two 12.7mm (0.5 in) diameter threaded steel rods placed in parallel along the diagonal (see Fig. 3-1). To make the mass distribution reasonably realistic, one floor slab is placed in each bay per floor: four 1000 kg slabs at each of the first, second and third levels, four 750 kg slabs on the fourth floor. On each floor two of the masses were placed off-center to increase the degree of coupling between the translational motions of the structure.

Ambient vibration and two types of forced excitations are considered in the tests. Ambient vibration includes excitations present from the environment due to wind, pedestrians, and traffic. The forced excitation cases consider both impact hammer tests, and broadband excitations provided by an electrodynamic shaker.

The overall mass of the body of the shaker is 81.6 kg, The moving mass of the shaker includes the armature (0.426 kg, included in the 81.6 kg) and the supplemental masses attached to the end of the shaker (2.95 kg, not included in the 81.6 kg). The shaker is placed on the top floor of the structure along the diagonal in the center of the SW bay. The command to the shaker is a band-limited white noise with components between 5–50 Hz. Additionally, in a few configurations, a sine sweep input was employed. To record the shaker force excitation, one accelerometer was placed on the shaker to measure the acceleration of the moving mass.

The impact hammer has a force transducer, and this measurement was recorded during the hammer tests. The maximum force that can be provided with this hammer is 5000lbf, and a medium/soft tip was used on the hammer head during the tests. This tip was selected because it excites the frequency of the structure. In each test a series of 3–5 hammer hits were recorded. Two impact locations were selected including a hit on the south face in the north direction, and a hit on the east face in the west direction (see Fig. 3-1). Both impacts were placed at the first floor of the structure in the southeast corner.

Fifteen accelerometers were placed throughout the frame to measure the responses of the test structure and on the base of the frame. FBA sensors were placed along the east and west frames of the structure to measure the motion in the north-south direction (along the strong axis). EPI sensors were placed near the center column of the frame, and oriented to measure the east-west motion of the structure (along the weak axis).

A 16-channel DasyLab acquisition system was used to record the structural responses. Anti-aliasing filters were used in the shaker tests and the ambient tests. In these two types of tests, the data was sampled at 250 Hz. In the hammer tests, a sampling rate of 1000 Hz was used, the anti-aliasing filters were turned off on the channel recording the impact force.

During the shaker testing, data acquisition was started several seconds after the excitation was turned on to ensure that the system had reached a steady state condition. In the hammer tests, the data acquisition system was started prior to the first impact. Each test consisted of recording a series of three to five hits. Several tests were also conducted by placing extra accelerometers on the base to which the structure is fixed.

TABLE 3-12. Characteristics of the Instrumentation

Sensor Model		Sensor Characteristics		
		Frequency Range	**Conditioner Antialiasing Filter Cutoff**	**Sensitivity**
Accelerometers	FBA	DC–50 Hz	50 Hz	5 Volts/g
	EPI Sensor	DC–200 Hz	50 Hz	5 Volts/g
	IC Sensors (on Shaker)	DC–1 kHz	50 Hz	0.222 V/g
Hammer	Dytran 5803A Impact Hammer (force transducer)	DC–1 kHz (med-soft tip)	–	1.12 mV/lbf

3.4.2 Damage Patterns

A series of tests were conducted on the structure with various damage scenarios. In the tests, damage is simulated by removing braces in the structure or by loosening bolts at beam-column connections. Table 3-13 shows the damage patterns studied in this dissertation. A complete description of the tests realized can be found in reference [31] or at the Task Group on SHM web page (http://wusceel.cive.wustl.edu/asce.shm).

TABLE 3-13. Description of Damage Patterns

Pattern	Description
1	Undamaged structure. All braces present.
2	All braces on the east side are removed.
3	Braces on the south half of the east side are removed.
4	Braces on the first and fourth floor of the south half of the east side are removed.
5	Braces on the first floor of the south half of the east side are removed.
6	Braces on the second floor of the north side are removed.

3.4.3 Benchmark Results

To improve the accuracy of the NExT and ERA techniques, different sets of data are employed to obtain an averaged and more representative model of the structure that is being identified. When dealing with hammer tests, for instance, results obtained from applying the ERA to all impacts can be used to obtain a more reliable average. In the case of ambient vibration records, several channels can be used as reference, obtaining, for each, a similar but distinct set of free response data and consequently different modal parameters. The three acceleration channels on the roof were each used as reference channels. Because two of those channels measure north-south accelerations and only one measures east-west accelerations, different weights were applied to the modal properties identified [40]. The averaged modal properties are calculated as

$$\lambda_i = \frac{\lambda_{i_1} + (\lambda_{i_2} + \lambda_{i_3})/2}{2} \text{ and } \phi_i = \frac{\phi_{i_1} + (\phi_{i_2} + \phi_{i_3})/2}{2}, \tag{3-3}$$

where λ_i and ϕ_i are the averaged *i*-th natural frequency and mode shape of the system, and λ_{i_r} and ϕ_{i_r} are the ones identified with the r reference channel.

To identify repeated mode shapes and readily reject the incorrect pair, the modal assurance criteria (MAC) was computed. The same parameters are used when averaging natural frequencies and mode shapes from different sets of data input to NExT and ERA. In this case, high correlation between two modes indicates that they are associated with the same frequency and should be averaged. In general, values between 0.9 and 1 indicate high correlation, and values between 0 and 0.1 indicate low correlation.

Tables 3-14 and 3-15 contain the identified natural frequencies for ambient vibration and hammer tests respectively. Note that compatible natural frequencies were detected with both ambient vibration and hammer tests for all damage scenarios. Note the increase

obtained in some of the frequencies after damaged is introduced to the structure. For instance, when all braces of the east side were removed (damage case 2), the identified frequency associated with the first mode increases by 3% and 6% for ambient vibration records and hammer tests, respectively. Because this frequency is associated with east-west motion of the structure, and the change of mass when removing the braces constitutes less than 1% of the total mass, no significant changes in this frequency were expected. The difference can be attributed, in part, to noise in sensors or nonlinearities of the structure. However, when the results have been obtained from several averages and the length of the data records are as long as those used for this study, it becomes clear that other factors such as experimental errors, variability of the disturbance, and changing ambient conditions can also be associated with this phenomenon. A more in depth analysis in this matter would be necessary to determine the causes.

TABLE 3-14. Identified Natural Frequencies Using Ambient Vibration

Damage Pattern	Mode 1 E-W motion	Mode 2 N-S motion	Mode 3 Torsion	Mode 4 E-W motion	Mode 5 N-S motion
1	7.50	7.77	14.48	19.88	21.01
2	7.73	5.66	12.74	20.13	15.02
3	7.65	6.65	13.48	20.02	18.91
4	7.60	7.35	13.97	20.12	19.71
5	7.56	7.45	14.03	19.89	20.63
6	5.96	7.79	13.19	19.87	20.99

TABLE 3-15. Identified Natural Frequencies Using Hammer Tests

Damage Pattern	Mode 1 E-W motion	Mode 2 N-S motion	Mode 3 Torsion	Mode 4 E-W motion	Mode 5 N-S motion	Mode 6 Torsion
1	7.47	7.64	14.45	19.90	20.87	22.52
2	7.94	5.11	12.69	19.97	14.91	22.14
3	7.56	6.50	13.39	19.90	18.76	22.22
4	7.53	7.25	13.94	20.02	19.65	22.41
5	7.53	7.37	13.99	19.83	20.46	22.56
6	--	7.67	13.06	19.80	20.79	22.34

Note that, for each damage case, six natural frequencies were detected when using the data acquired with hammer tests and only five were detected from ambient vibration data. In general, this difference is an indication of the bandwidth of the ambient vibrations exciting the structure and the small amplitudes in the motion of the structure.

Note also that the frequency associated with the first mode of vibration of the sixth damage case could not be detected with the data acquired from the hammer impacts. The hammer impacts were all located in the southeast corner of the first floor (between first and second stories) in both south-north and east-west directions. According to the mode shape detected for this damage case using ambient vibration, the hammer hit was at the location corresponding to the lowest amplitude of that particular mode shape (due to some torsion effects generated by the removal of some braces of the second floor). As a result, this mode was not excited significantly by the hammer. Although five other modes were detected for this damage case, important information is missing and the chances of successfully detecting the damaged members decreased.

Considerable differences are consistently observed between the mode shapes detected with ambient vibration and hammer tests (see undamaged cases in Fig. 3-9). Because a large amount of information was analyzed and averages from different sets of data were obtained, this phenomenon cannot be attributed to noise in the sensors. Although the sources are not precisely known, it is likely that these changes are due to a nonlinearity in the structure (friction between elements perhaps) that affects the behavior of the building mainly when the amplitude of the displacements is small (i.e. ambient vibration).

Although the inconsistencies in the mode shapes identified with ambient vibration and hammer tests were important for most damage cases, the greatest impact on the stiffness identification process was noticed in the undamaged case. Additionally, notice in Fig. 3-9 that elements of the second floor are most affected by this phenomenon. As a result, when detecting elemental stiffness values of the different damage cases, elements opposing the

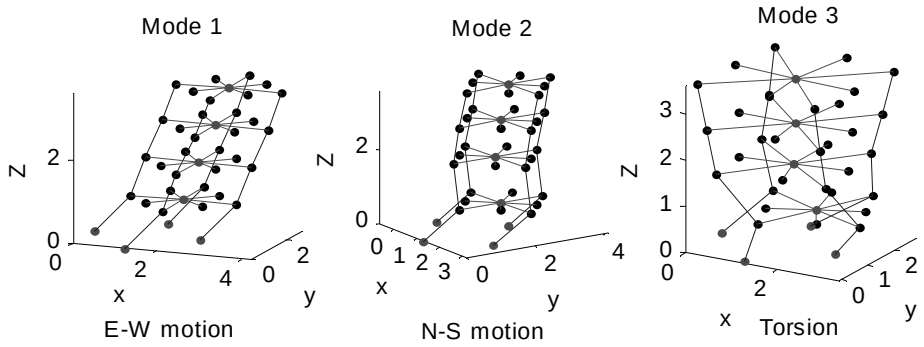

(a) Ambient Vibration Excitation

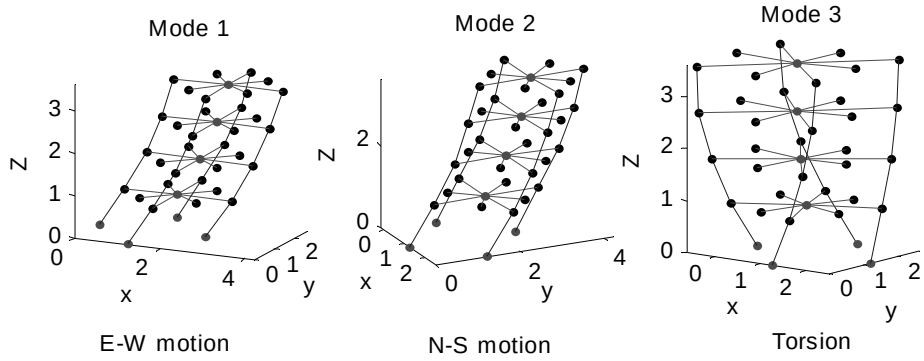

(b) Hammer Tests

FIGURE 3-9. Identified Mode Shapes for the Undamaged Case

north-south displacement of the second floor had higher values than those detected on the undamaged case.

The 12 DOF identification model was used in this exercise [40]. The masses of the identification model were changed to obtain a better representation of the physical model. Figure 3-10 displays the members of the identification model that are associated with the members of the experimental structure in which damage was induced. Tables 3-16 and 3-17 contain the identified elemental stiffness of all 16 members of the identification model as a percentage of their initial stiffness values (undamaged case) for ambient vibration and hammer tests respectively. Herein, members with less than 10% stiffness loss are considered to be healthy. Bolded values indicate members whose stiffnesses were expected to be reduced. Note that with the exception of member 7 of the sixth damage

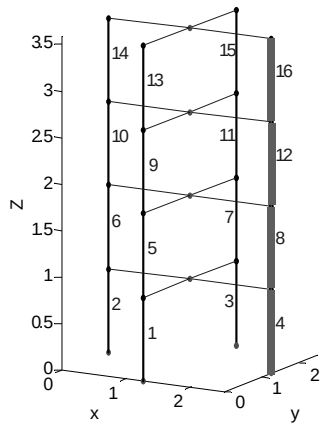

(a) Damage patterns 2 and 3

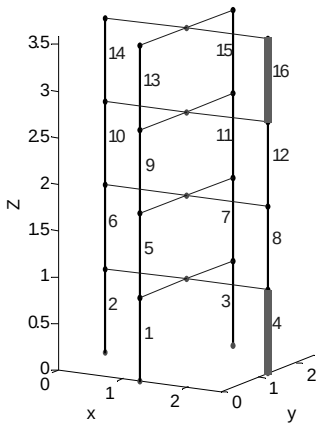

(b) Damage pattern 4

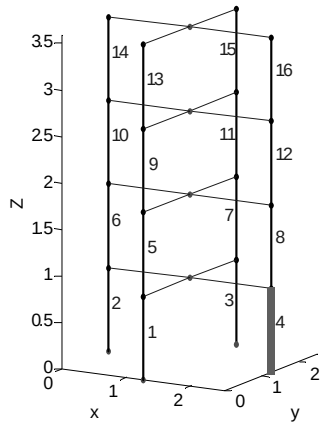

(c) Damage pattern 5

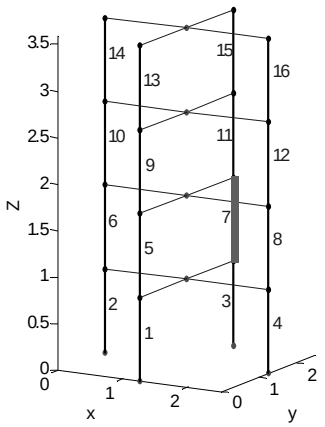

(d) Damage pattern 6

FIGURE 3-10. Members Expected to be Damaged

pattern for ambient vibration, all expected reductions are detected. As mentioned before, especially in the undamaged case, the structure behaves differently for small amplitudes, greatly decreasing the identified elemental stiffness values of members 5 and 7. As a result, a gain of stiffness for these members was detected for all damage scenarios.

In a few cases, losses in the stiffness values were detected when they were not present (false positives), the most critical case being element 5 of damage pattern 6 of the hammer tests, whose identified stiffness had a value below zero. This false positive is most likely due to the lack of vital information regarding this damage scenario (the first natural

TABLE 3-16. Stiffness Reduction Using Ambient Vibration

Element number	Pattern 1 (%)	Pattern 2 (%)	Pattern 3 (%)	Pattern 4 (%)	Pattern 5 (%)	Pattern 6 (%)
1	0	0	0	0	0	0
2	0	0	0	0	0	0
3	0	0	0	0	0	0
4	0	***66***	***23***	***32***	***33***	0
5	0	0	0	0	0	0
6	0	0	2	22[a]	7	2
7	0	0	0	0	0	***0***[b]
8	0	***36***	***32***	10	1	5
9	0	0	12	2	4	0
10	0	0	0	20[a]	2	0
11	0	4	4	1	0	0
12	0	***77***	***42***	0	0	0
13	0	0	4	0	0	0
14	0	0	0	0	0	0
15	0	4	0	0	0	5
16	0	***88***	***38***	***41***	0	4

a. False positive (damage detected when not present)

b. False negative (stiffness reduction not detected)

frequency is missing). In all other cases the loss in stiffness values ranged between 10 and 23%, and damage can be arguable for the types of damage induced in this experimental structure.

Although, for purposes of damage detection, it is preferable to obtain false positives than false negatives (*i.e.*, detect all damaged members and probably a few more, rather than not detecting some damage), it is desirable for any SHM technique to be accurate enough to detect only the damaged components. However, because damage in this particular structure was induced by removing some of the elements, it is possible that the connections had also been influenced by the changes of the structure, slightly reducing the effective stiffness of the adjacent members. As a result, false positives may be obtained.

TABLE 3-17. Stiffness Reduction Using Hammer Tests

Element number	Pattern 1 %	Pattern 2 %	Pattern 3 %	Pattern 4 %	Pattern 5 %	Pattern 6 %
1	0	0	0	0	0	0
2	0	0	0	0	0	3
3	0	0	0	0	0	0
4	0	***83***	***38***	***39***	***42***	5
5	0	0	0	0	0	0[a]
6	0	0	0	0	0	0
7	0	0	0	0	0	***41***
8	0	***79***	***37***	2	2	0
9	0	23[a]	0	8	0	8
10	0	0	0	10	2	0
11	0	0	0	0	0	0
12	0	***71***	***37***	0	0	0
13	0	16[a]	0	0	0	0
14	0	0	0	0	0	0
15	0	0	0	0	0	0
16	0	***79***	***32***	***35***	0	0

a. False positive (damage detected when not present)

As mentioned before, several identification models can be employed to detect damage and improve the performance of the damage detection technique.

3.5 Summary

A review of the work accomplishments when applying the proposed SHM methodology to the IASC-ASCE SHM benchmark problem during the last four years has been presented in this section. The first numerical phase of this problem was studied extensively in [12] using an early version of the methodology presented in this dissertation. Here it was found that the methodology was relatively insensitive to noise in the sensors and that the modeling errors between a 12 DOF identification model and the 120 structural model were not significant for the benchmark structure.

The effect of uncertainty in the information known by the researchers was studied in the second analytical phase of the benchmark problem. Here, the 120 DOF structural model was used to produce the acceleration measurements for the identification. The mass and stiffness values of the structural model deviated from their nominal value by a random number. The participants of the benchmark problem did not have access to this random number increasing the uncertainties in the model. The SHM based on NExT, ERA and the least squares solution of the eigenvalue problem performed well in this second phase indicating that the methodology is effective even though the mass matrix used in the identification process deviates from the true value. The methodology was also tested on two blind cases of this second numerical phase. In this case the participants did not have any knowledge of the damage in the structure. By using two different identification models, and comparing the information of these two models the methodology was used to correctly identify the existence, location and amount of damage in the structure.

In the last part of this chapter the experimental benchmark problem was discussed. Here acceleration records of the real structure were used for the damage identification. In this phase different excitation cases were considered, including ambient excitation and hammer testing. The results demonstrated the potential of using ambient excitations for the identification of modal parameters. Five natural frequencies and mode shapes were identified using ambient vibration. These agreed with the modal parameters obtained using hammer testing. In the identification of the change of stiffness some false positives cases were identified. These results were probably due to leakage in the stiffness reduction in neighbor members.

In summary, it has been shown that the presented methodology has the potential to work in real case scenarios. The IASC-ASCE SHM benchmark problem has been an excellent tool for the development and implementation of this methodology and future benchmark studies should be encouraged to continue the evolution of the SHM methodology and to develop a better understanding of the difficulties faced in SHM.

Chapter 4

Sensitivity of Structural Behavior to Damage in Flexible Structures

This chapter examines the effects of structural damage on the overall behavior of a cable-stayed bridge deck. Sensitivity of the static displacement and the dynamic properties of the structure are studied when different levels of damage are imposed. The first section of this chapter discusses the modeling of cable-stayed bridges. Next, the Bill Emerson Memorial Bridge (Cape Girardeau, Missouri, U.S.A.) is discussed followed by a description of the finite element model of the bridge. Finally, a parametric study is performed to determine the sensitivity of the static displacement, natural frequencies and mode shapes to damage in the deck of the structure.

4.1 Modeling of Cable-Stayed Bridges

Cable-stayed bridges are the best solution for medium to long span bridges due to their aesthetic appearance and their economy in construction. In addition, advances in the materials used in their construction and the methodologies used in their analysis are making cable-stayed bridges with main spans ranging from 200m to 500m very popular. In these structures cables are used to suspend the deck of the bridge reducing the moments applied to the deck girders, and thus reducing the size of the members needed in the deck. The static and dynamic loads travel through the cables to the piers, creating enormous compression loads. The deck is also subject to compression loads due to the inclination of the cables. Even though the materials in cable-stayed bridges remain within the linear

range, nonlinearities due to the sag in the cables, beam-column effects due to large compressive loads, and changes in the geometry of the structure should be considered in modeling this class of structures.

The following two sections will describe the methodology followed to obtain a nonlinear static model of a cable-stayed bridge. This nonlinear model is obtained using dead loads and pre-tension in the cables.

4.1.1 Nonlinear Static Analysis

Cable-stayed bridges behave nonlinearly under dead loads even when the material is in the linear range. This nonlinearities are due to three major factors: i) nonlinear behavior in the cables; ii) beam-column effects due to large compression forces; and iii) large displacements producing changes in geometry [57, 65, 85].

Tension in the Cables

The first source of nonlinearitys in cable-stayed bridges is the nonlinear behavior of the cables. When the axial load in the cables is small, a small apparent tangent stiffness is obtained due to the sag produced by the cable's self-weight. When the tension is increased the sag in the cable is reduced, and the apparent stiffness of the cable increases, as shown in the strain-stress curve in Fig. 4-1. In modeling the cables, the catenary shape and its variation with the axial force in the cable are modeled using an equivalent elastic modulus [35]. The cable element has a modified modulus of elasticity, E_{eq}, given by

$$E_{eq} = \frac{E_c}{1 + \left[\frac{(wL_x)^2 A_c E_c}{12 T_c^{\,3}}\right]} \tag{4-1}$$

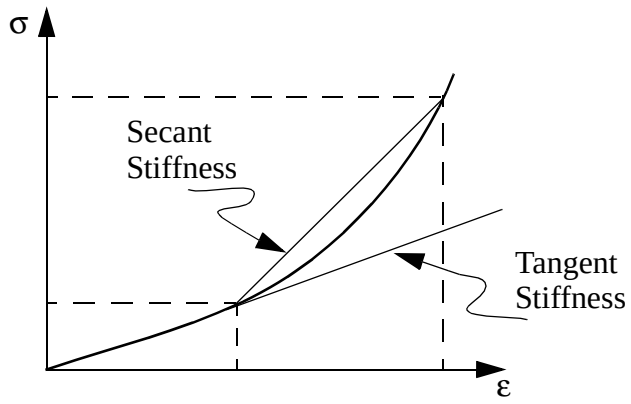

FIGURE 4-1. Tangent and Secant Equivalent Stiffness for Cable Stays

where A_c is area of the cross-section, T_c is the tension in the cable, w is its weight per unit length, L_x is the projected length in the horizontal plane, and E_c is the modulus of elasticity of the material. The cable stiffness contribution to the global stiffness matrix is only applied when the cable is under tension and is omitted otherwise.

The value of E_{eq} obtained in Eq. 4-1 is the tangential stiffness of the cable (See Fig. 4-1). When the cable changes from an initial tension T_i to a final tension T_f, the secant stiffness of the cable is given by the equation

$$E_{eq} = \frac{E_c}{1 + \left[\frac{(wL_x)^2(T_i + T_f)A_cE_c}{24T_i^2T_f^2}\right]} \tag{4-2}$$

Second Order Effects

Axial forces and bending moments are often treated separately in a finite element model. In the case of cable-stayed bridges, second order effects need to be considered due to the high compression forces in the deck and the towers. The bending stiffness of a member

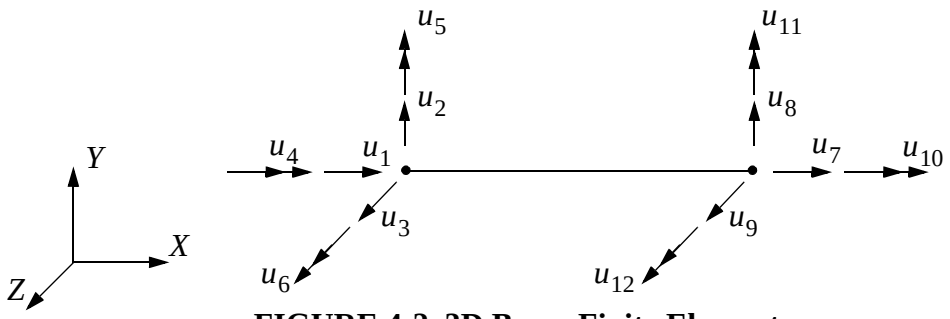

FIGURE 4-2. 3D Beam Finite Element

will decrease when subjected to compression loads. Similarly the axial stiffness of the member is affected by the bending moments and this effect must be considered when the stiffness matrix is formed.

Stability functions can be used to model the reduction or increase in the stiffness due to large internal loads. The elemental stiffness matrix for the 3D beam element shown in Fig. 4-2 is [65]

$$k = \begin{bmatrix}
\frac{AE}{L}S_5 & 0 & 0 & 0 & 0 & 0 & -\frac{AE}{L}S_5 & 0 & 0 & 0 & 0 & 0 \\
 & \frac{12EI_z}{L^3}S_{1z} & 0 & 0 & 0 & \frac{6EI_z}{L^2}S_{2z} & 0 & -\frac{12EI_z}{L^3}S_{1z} & 0 & 0 & 0 & \frac{6EI_z}{L^3}S_{2z} \\
 & & \frac{12EI_y}{L^3}S_{1y} & 0 & -\frac{6EI_y}{L^2}S_{2y} & 0 & 0 & 0 & -\frac{12EI_y}{L^3}S_{1y} & 0 & -\frac{6EI_y}{L^2}S_{2y} & 0 \\
 & & & \frac{GJ}{L} & 0 & 0 & 0 & 0 & 0 & -\frac{GJ}{L} & 0 & 0 \\
 & & & & \frac{4EI_y}{L}S_{3y} & 0 & 0 & 0 & \frac{6EI_y}{L^2}S_{2y} & 0 & \frac{2EI_y}{L}S_{4y} & 0 \\
 & & & & & \frac{4EI_z}{L}S_{3z} & 0 & \frac{6EI_z}{L^2}S_{2z} & 0 & 0 & 0 & \frac{2EI_y}{L}S_{4y} \\
 & & & & & & \frac{AE}{L}S_5 & 0 & 0 & 0 & 0 & 0 \\
 & & & & & & & \frac{12EI_z}{L^3}S_{1z} & 0 & 0 & 0 & -\frac{6EI_z}{L^2}S_{2z} \\
 & & \text{Symmetric} & & & & & & \frac{12EI_y}{L^3}S_{1y} & 0 & -\frac{6EI_y}{L^2}S_{2y} & 0 \\
 & & & & & & & & & \frac{GJ}{L} & 0 & 0 \\
 & & & & & & & & & & \frac{4EI_y}{L}S_{3y} & 0 \\
 & & & & & & & & & & & \frac{4EI_z}{L}S_{3z}
\end{bmatrix} \quad (4\text{-}3)$$

where E is Young's modulus; G is the shear modulus; A is the cross sectional area of the beam; L is the length of the beam; I_y and I_z are the moment of inertia of the cross-section with respect to the Y and Z axes, respectively; and J is the polar moment of inertia of the cross-section area. The stability functions S_{1z} to S_{4z} for an element in tension are [65]

$$S_{1z} = \upsilon_z^3 \frac{\sinh \upsilon_z}{12R_t}; \tag{4-4}$$

$$S_{2z} = \upsilon_z^2 \frac{\cosh \upsilon_z - 1}{6R_t}; \tag{4-5}$$

$$S_{3z} = \upsilon_z \frac{\upsilon_z \cosh \upsilon_z - \sinh \upsilon_z}{4R_t}; \tag{4-6}$$

$$S_{4z} = \upsilon_z \frac{\sinh \upsilon_z - \upsilon_z}{2R_t}; \tag{4-7}$$

where

$$R_t = 2 - 2\cosh \upsilon_z + \upsilon_z \sinh \upsilon_z, \tag{4-8}$$

and

$$\upsilon_z = L\sqrt{\frac{P}{EI_z}}. \tag{4-9}$$

The stability functions S_{1y} to S_{4y} are calculated similarly by changing I_z to I_y. The stability function S_5 for a member in tension is calculated as

$$S_5 = \frac{1}{1 - \frac{EA(R_{tmy} + R_{tmz})}{4P^3L^2}} \tag{4-10}$$

where

$$R_{tmy} = \upsilon_y(M_{1y}^2 + M_{2y}^2)(\coth\upsilon_y + \upsilon_y \operatorname{csch}^2\upsilon_y) - 2(M_{1y} + M_{2y})^2 + M_{1y}M_{2y}(1 + \upsilon_y \coth\upsilon_y)(2\upsilon_y \operatorname{csch}\upsilon_y) \quad , \tag{4-11}$$

$$R_{tmz} = \upsilon_z(M_{1z}^2 + M_{2z}^2)(\coth\upsilon_z + \upsilon_z \operatorname{csch}^2\upsilon_z) - 2(M_{1z} + M_{2z})^2 + M_{1z}M_{2z}(1 + \upsilon_z \coth\upsilon_z)(2\upsilon_z \operatorname{csch}\upsilon_z) \quad . \tag{4-12}$$

M_{1y} and M_{2y} are the moments at nodes 1 and 2 with respect to the Y axis, and M_{1z} and M_{2z} are the moments at nodes 1 and 2 with respect to the Z axis.

For a member in compression the stability functions S_{1z} to S_{4z} are

$$S_{1z} = \upsilon_z^3 \frac{\sinh\upsilon_z}{12R_c}; \tag{4-13}$$

$$S_{2z} = \upsilon_z^2 \frac{1 - \cosh\upsilon_z}{6R_c}; \tag{4-14}$$

$$S_{3z} = \upsilon_z \frac{\sin\upsilon_z - \upsilon_z \cos\upsilon_z}{4R_c}; \tag{4-15}$$

$$S_{4z} = \upsilon_z \frac{\upsilon_z - \sin\upsilon_z}{2R_c}, \tag{4-16}$$

where υ_z is defined by Eq. 4-9 and

$$R_c = 2 - 2\cos\upsilon - \upsilon\sin\upsilon . \tag{4-17}$$

The stability functions S_{1y} to S_{1z} for a member in compression are obtained replacing I_z by I_y. For a member in compression S_5 is defined as

$$S_5 = \frac{1}{1 - \dfrac{EA(R_{cmy} + R_{cmz})}{4P^3L^2}}, \tag{4-18}$$

where

$$\begin{aligned} R_{cmy} = {} & \upsilon_y(M_{1y}^2 + M_{2y}^2)(\cot\upsilon_y + \upsilon_y\csc^2\upsilon_y) - 2(M_{1y} + M_{2y})^2 \\ & + (M_{1y}M_{2y})(1 + \upsilon_y\cot\upsilon_y)(2\upsilon_y\csc\upsilon_y) \end{aligned} , \tag{4-19}$$

$$\begin{aligned} R_{cmz} = {} & \upsilon_y(M_{1z}^2 + M_{2z}^2)(\cot\upsilon_z + \upsilon_z\csc^2\upsilon_z) - 2(M_{1z} + M_{2z})^2 \\ & + (M_{1z}M_{2z})(1 + \upsilon_z\cot\upsilon_z)(2\upsilon_z\csc\upsilon_z) \end{aligned} . \tag{4-20}$$

For small values of axial force the stability functions S_1 to S_4 are numerically unstable [57]. To avoid this instability these values are set to one when $P/(EI) < 1\times10^{-9}$. Figure 4-3 shows the variation of S_1 to S_4 with respect to υ^2. Positive values of υ^2 are for members under tension and negative values are for members under compression.

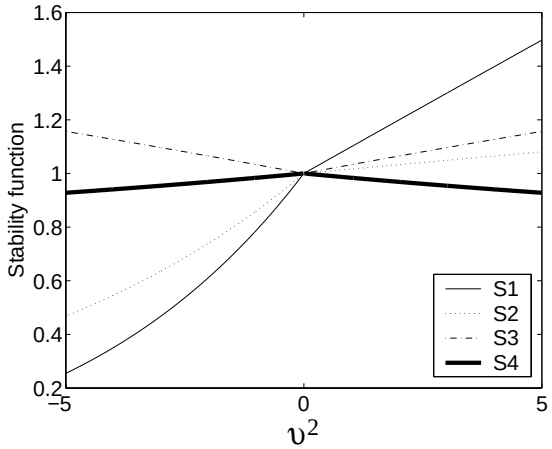

FIGURE 4-3. Stability Functions

Geometry Change

The final source of nonlinearitys in cable-stayed bridges are due to changes in the geometry of the structure. Linear analysis assumes that the geometry of the structure is the same before and after the application of static loads. Cable-stayed bridges can exhibit large displacements due to static loads, changing the geometry of the elements and affecting the stiffness of the structure.

4.1.2 Solution of the Nonlinear Problem

Several approaches can be taken to solve nonlinear static problems [25, 38]. A very basic method is the incremental approach, which consists of applying the load in incremental steps as shown in Fig. 4-4a. For every step the tangent stiffness matrix of the structure is calculated, and a new portion of the dead load is applied to the structure. This method is simple, and convergence to a solution is guaranteed. However, significant errors are obtained if the step sizes are chosen incorrectly. For example, consider the load displacement curve shown in Fig. 4-4a. In this figure the actual load-displacement curve is shown as a thick line, and the displacements for each load increment are shown by the

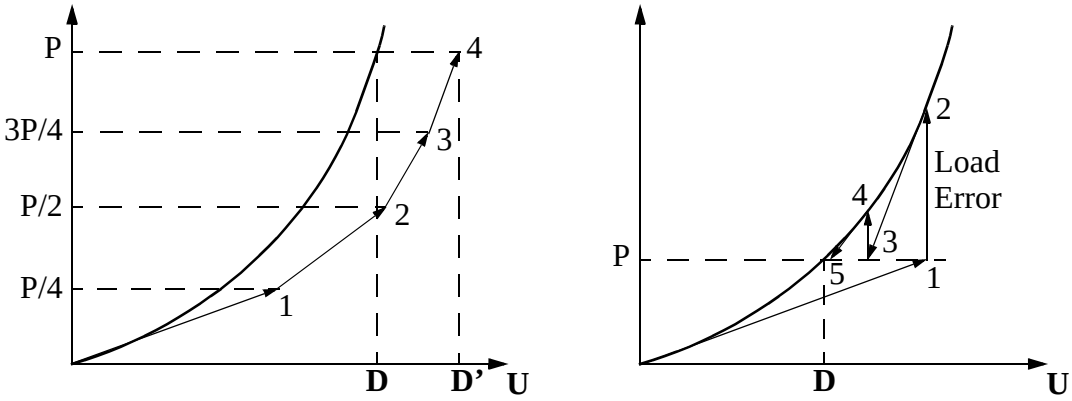

(a) Incremental Approach (b) Newton-Raphson Method

FIGURE 4-4. Methods to Solve Nonlinear Problems

arrows. By dividing the load in four the method will show that the final displacement **D'** is the solution, where the actual solution is the displacement **D**. To obtain an accurate solution for complex nonlinear problems a large number of steps might be needed, increasing the computational resources needed to solve the problem. Another disadvantage of this method is the lack of an indication of the accuracy of the solution.

One of the most commonly used methods to solve nonlinear problems is the Newton-Raphson method. The method starts by calculating the tangent stiffness matrix of the structure and obtaining the corresponding displacement for the load **P** (See point 1 in Fig. 4-4b). Then, a new stiffness matrix is calculated with the deformed structure. Point 2 is obtained by calculating the external forces needed to obtain the displacement of point 1. The error in the load is obtained by subtracting **P** from the forces at point 2. A new iteration is performed by applying a new force to the structure equal to the force error using the new tangent stiffness. The process is repeated until the load error is small. Figure 4-5 shows a flow diagram of the methodology.

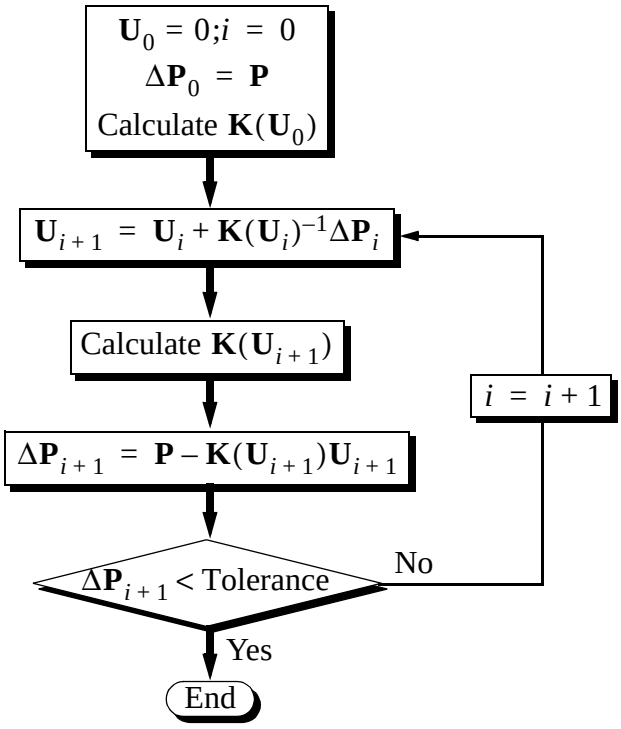

FIGURE 4-5. Flow Diagram for the Newton-Raphson Method

Unlike the incremental approach, with the Newton-Raphson method it is possible to measure the error at the end of every iteration, and decrease the error in every iteration. A drawback of the Newton-Raphson method is that convergence is not guaranteed in some problems. For instance, Fig. 4-6 shows a case in which the method will not converge to a solution and it will "jump" back and forth between points 1 and 2 of the force displacement curve. To improve the convergence of the method, several variations have been proposed. One of these solutions is a hybrid approach between the incremental approach and the Newton-Raphson method. In this case the load is divided and applied in several steps similar to the incremental approach. The Newton-Raphson method is used to reach the solution for each step. Another variation is to use a portion of the load error in every step. This will increase the number of iterations needed to reach a solution but will increase the convergence of the algorithm.

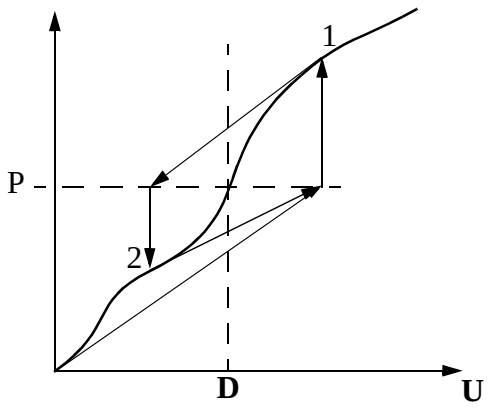

FIGURE 4-6. Convergence Problems for the Newton-Raphson Method

The nonlinear static procedure was included in the FEM toolbox developed for this dissertation. The variation of the Newton-Raphson method with the incremental approach was selected for implementation. In addition, a fraction of the error load can be applied in every iteration.

4.2 Bill Emerson Memorial Bridge Model

Previously, the sources of nonlinearities in cable-stayed bridges and methods to solve the nonlinear static problem were presented. In this section a description of the Bill Emerson Memorial Bridge is discussed. This bridge was selected to perform the sensitivity studies to damage in the deck discussed at the end of this chapter. Following this discussion the formulation of a static nonlinear finite element model is presented based on the previous section.

4.2.1 Bridge Description

The cable-stayed bridge used for this numerical study is the Bill Emerson Memorial Bridge spanning the Mississippi River (on Missouri 74–Illinois 146) near Cape Girardeau, Missouri, designed by the HNTB Corporation [41]. The bridge is currently under construction and is to be completed in fall 2003 with a total cost of $100 million U.S.

Source:<http://www.modot.state.mo.us/local/d10/emersonbridge/Emerson-index.html>

FIGURE 4-7. Construction of the Emerson Bridge

dollars. Instrumentation is being installed on the Emerson Bridge and surrounding soil during the construction process to evaluate the structural behavior and seismic risk [18].

Seismic considerations were strongly considered in the design of this bridge due to its location (in the New Madrid seismic zone) and its critical role as a principal crossing of the Mississippi River. In early stages of the design process, the seismic loading cases governed. Earthquake load combinations in accordance with American Association of State Highway and Transportation Officials (AASHTO) Division I-A specifications were used in the design. Various designs were considered, including full longitudinal restraint at the tower piers, no longitudinal restraint, and passive isolation. When temperature effects were considered, it was found that fully restraining the deck in the longitudinal direction would result in unacceptably large stresses. Based on examination of the various designs, it was determined that incorporating force transfer devices would provide the most efficient solution.

Sixteen 6.67 MN (1,500 kip) shock transmission devices are employed in the connection between the tower and the deck. These devices are installed in the longitudinal direction to allow for expansion of the deck due to temperature changes. Under dynamic loads these

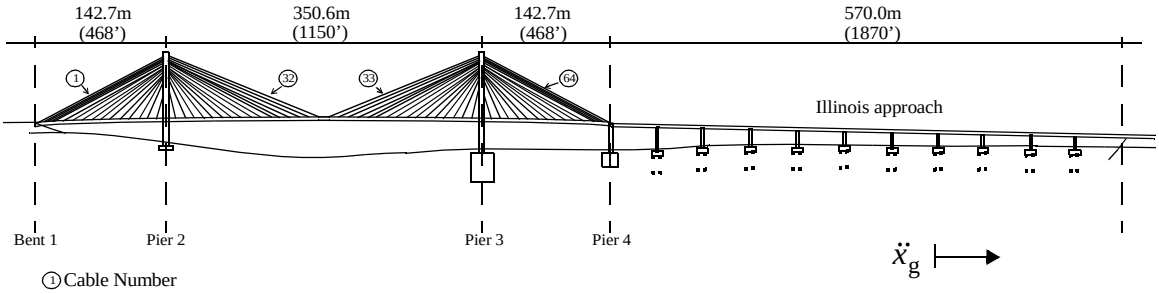

FIGURE 4-8. Drawing of the Cape Girardeau Bridge

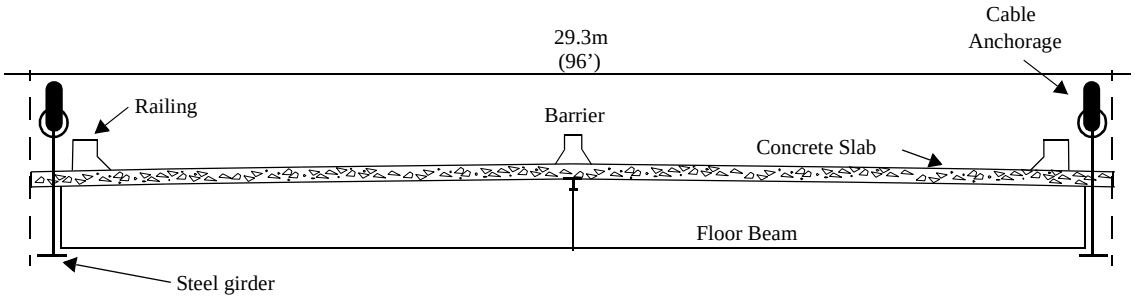

FIGURE 4-9. Cross Section of Bridge Deck

devices are extremely stiff and are assumed to behave as rigid links. Additionally, in the transverse direction earthquake restrainers are employed at the connections between the tower and the deck, and the deck is constrained in the vertical direction at the towers. The bearings at bent 1 and pier 4 are designed to permit longitudinal displacement and rotation about the transverse and vertical axis. Soil-structure interaction is not expected to be an issue with this bridge as the foundations of the cable-stayed portion is attached to bedrock.

The bridge is composed of two towers, 128 cables, and 12 additional piers in the approach bridge from the Illinois side as shown in Fig. 4-8. It has a total length of 1205.8 m (3956 ft) with a main span of 350.6 m (1150 ft) and side spans of 142.7 m (468 ft) in length. The approach on the Illinois side is 570 m (1870 ft). A cross-section of the deck is shown in Fig. 4-9. The bridge has four lanes plus two narrower bicycle lanes, for a total width of 29.3 m (96 ft). The deck is composed of steel beams and prestressed concrete slabs. Steel,

ASTM A709 grade 50W, is used, with an f_y of 344 MPa (50 ksi). The concrete slabs are made of prestressed concrete with a f_c' of 41.36 MPa (6 ksi). Additionally, a concrete barrier is located in the center of the bridge, and a railing is located along the edges of the deck.

The 128 cables are made of high–strength, low–relaxation steel (ASTM A882 grade 270). The smallest cable area is 28.5 cm^2 (4.41 in^2) and the largest cable area is 76.3 cm^2 (11.83 in^2). The cables are covered with a polyethylene piping to resist corrosion. The H-shaped towers have a height of 102.4 m (336 ft) at pier 2 and 108.5 m (356 ft) at pier 3. Each tower supports a total 64 cables. The towers are constructed of reinforced concrete with a resistance, f_c', of 37.92 MPa (5.5 ksi). The cross-section of each tower varies five times over the height of the tower, as shown in Fig. 4-10. Section A is used in the top of the legs, section B in the middle of the legs, and section E in the bottom of the towers. Some of these elements have variable sections. Section D shows the cross-section in the bottom

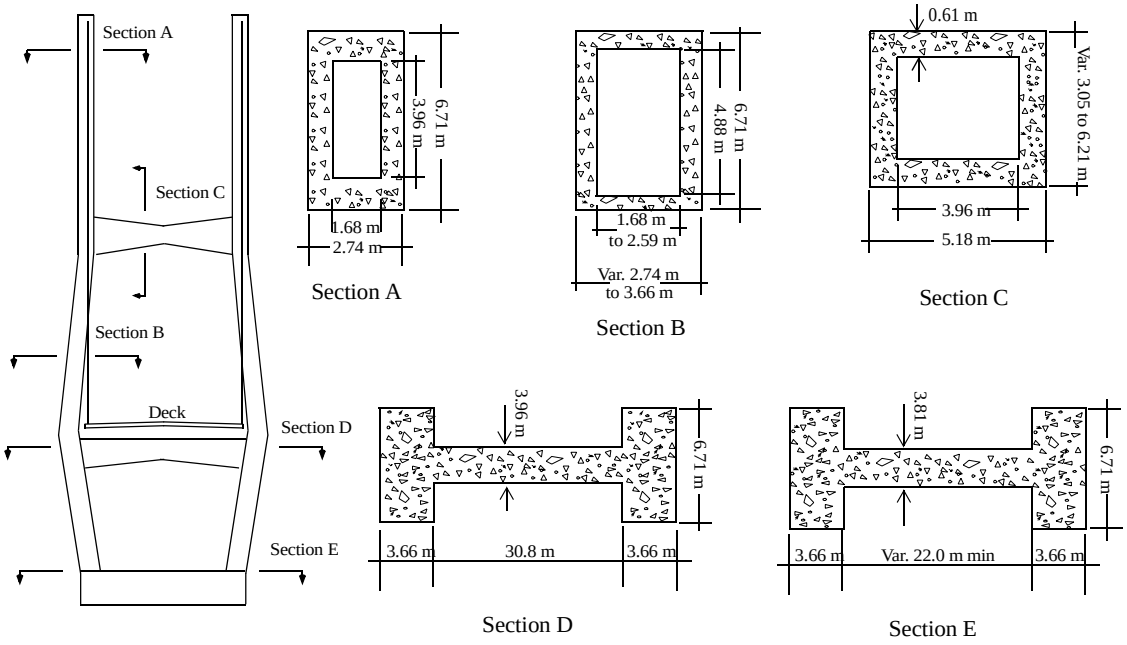

FIGURE 4-10. Cross Sections of the Towers

TABLE 4-1. Material Density

Material	Density (Kg/m^3)	Density (PCF)
Reinforced concrete	2402.77	150
Prestressed concrete	2482.86	155
Seal Concrete	2306.66	144
Stay cable grout	2322.68	145
Structural Steel	7849.08	490
Cables (Steel)	7849.08	490

TABLE 4-2. Mass of the Elements for the Cross Section of the Deck

Item	Weight per unit length	
	(Kg/m)	(lb/inch)
Silica fume concrete layer	34.15	75.29
Precast concrete deck	125.21	276.05
Steel girder	11.67	25.74
Floor beam	0.87	1.93
Railing	8.61	18.98
Barrier	7.73	17.05
Total	188.41	415.37

strut, and section C shows the cross section of the strut located in the middle of the tower. The approach bridge from the Illinois side is supported by 11 piers and bent 15 which are made of concrete. The deck consists of a rigid diaphragm made of steel with a slab of concrete at the top. The density of the materials as specified in the drawings are summarized in Table 4-1. Detailed dimensions for the elements of the cross sectional of the deck and the calculation of the mass are shown in Table 4-2.

4.2.2 Finite Element Model

Based on the description of the Emerson Bridge provided in the previous section, a three-dimensional finite element model of the bridge was developed in Matlab [64]. The model was originally developed for the benchmark problem in structural control of cable-stayed bridges under seismic excitation [34, 83] and has been modified to study the advantages

and disadvantages of different SHM techniques. A linear model is used in this chapter. However, the stiffness matrices used in this linear model are those of the structure determined through a nonlinear static analysis corresponding to the deformed state of the bridge with dead loads [86] as described in section 4.1. Additionally, the bridge is assumed to be attached to bedrock, and the effects of soil–structure interaction are neglected.

The finite element model employs beam elements, cable elements, rigid link elements and lumped mass elements. The nonlinear static analysis is performed in Matlab [64] using a finite element toolbox developed in-house. The finite element model, shown in Fig. 4-11, has a total of 572 nodes, 418 rigid links, 156 beam elements, 198 nodal masses and 128 cable elements. The towers are modeled using 224 nodes, 80 beam elements and 144 rigid links. Constraint equations are applied to restrict the deck from moving in the lateral and vertical directions and rotate with respect to the *X* axis at piers 2, 3 and 4. Boundary conditions restrict the motion at pier 1 to allow only longitudinal displacement (*X*) and rotations about the *Y* and *Z* axes. Because the attachment points of the cables to the deck are above the neutral axis of the deck, and the attachment points of the cables to the tower are outside the neutral axis of the tower, rigid links are used to connect the cables to the tower and to the deck (see Fig. 4-12). The use of the rigid links ensures that the length and inclination angles of the cables in the model agree with the drawings. Additionally, the moment induced in the towers by the movement of the cables is taken into consideration in this approach. In the case of variable sections, the average of the section is used for the finite element.

Note that the Illinois approach is not included in this model (see Fig. 4-8). Because the bearing at pier 4 does not restrict either longitudinal motion or rotation about the *X* axis of the bridge, the Illinois approach was found to have a negligible effect on the dynamics of the cable-stayed portion of the bridge.

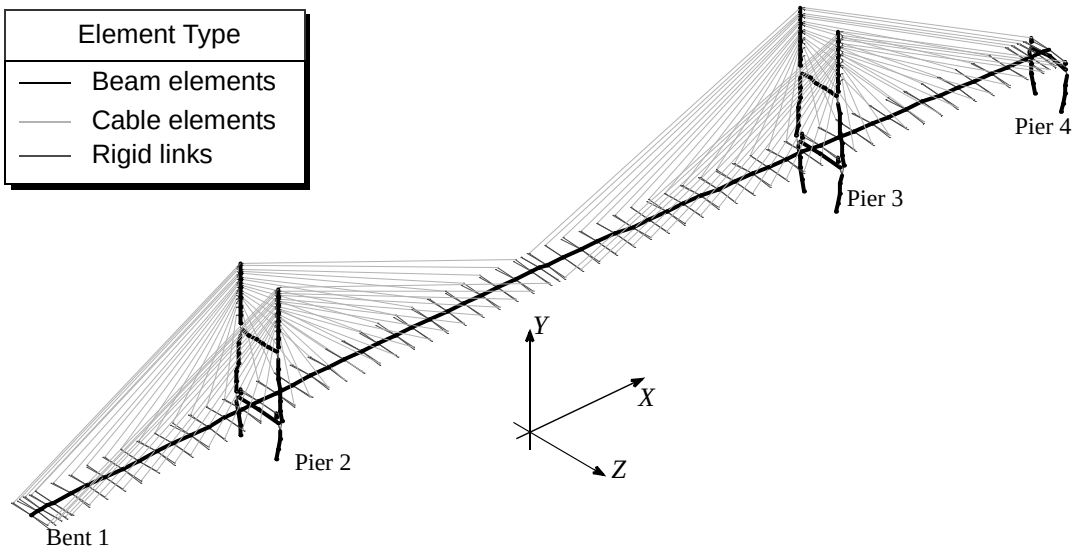

FIGURE 4-11. Finite Element Model

The deck was modeled using the method described by Wilson and Gravelle [86]. In this approach the deck is modeled as a central beam (the spine) which has no translational mass. Lumped masses are employed to model the mass of the deck, and are connected to the spine using rigid links (see Fig. 4-14). The masses are included to more realistically model the torsional response of the deck to lateral loads, and have been shown to be important in the modeling of this structure [16].

The deck is comprised of two main steel girders along each longitudinal edge of the deck supporting the concrete slab (see Fig. 4-9). Thus, the deck is treated as a C-shaped section as shown in Fig. 4-13 [86]. Here the steel beams are represented by the flanges of the section, and the concrete slab is represented by the web of the C-shaped section. The axial stiffness of the deck is calculated by converting the area of the concrete slab into an equivalent area of steel using the ratio of the two elastic moduli. The area of the equivalent section is $1.844 m^2$. The moments of inertia about the vertical and transverse axes are also obtained converting the concrete slab to an equivalent steel structure. The barriers and

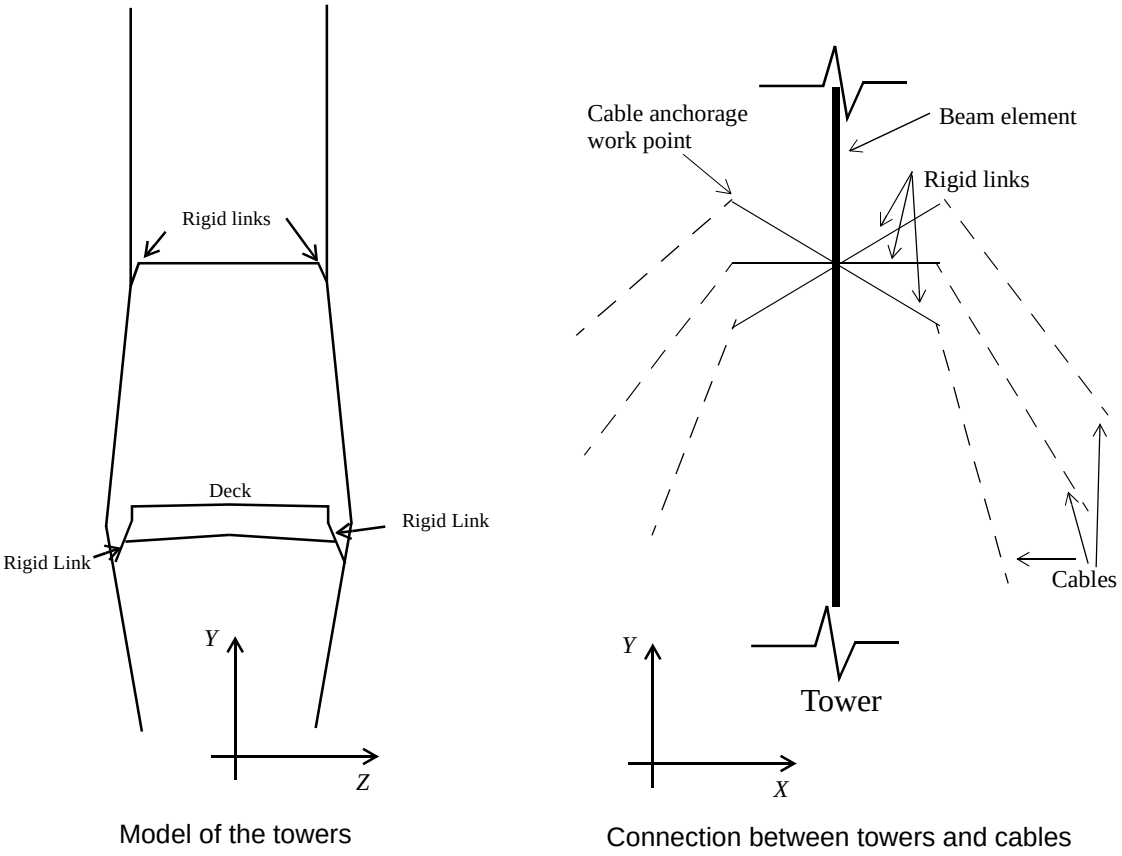

FIGURE 4-12. Finite Element Model of the Towers

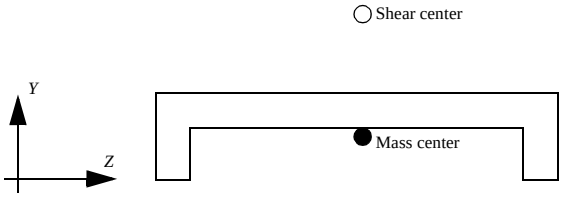

FIGURE 4-13. C-Shaped Section Used to Determine Properties of Deck

railings were not taken into consideration because they are not structural elements. The moment of inertia of the typical deck section have values of I_{yy}=160.67m^4, I_{zz}=0.6077m^4, and J_{eq}=0.0677 m^4. The neutral axis is located at 1.77m above the bottom of the steel beams.

The calculation of the torsional stiffness of the deck section takes into consideration both pure and warping torsional constants. The pure torsion constant is determined by [86]

$$J_t = \sum_{i=1}^{n} \frac{b_i t_i^3}{3} \tag{4-21}$$

where b_i and t_i are the length and thickness of thin sections which make up the deck cross-section. The warping constant is calculated as [10]

$$\Gamma_w = \frac{d^2}{4}\left\{ I_{zz} + e^2 A\left(1 - \frac{d^2 A}{4 I_{yy}}\right)\right\} \tag{4-22}$$

where d is the distance between the webs of the two steel beams located along the edges of the deck, e is the distance between the neutral axis and the middle of the concrete slab, and A is the equivalent cross-sectional area. I_{yy} and I_{zz} are the moments of inertia of the deck about the *Y* and *Z* axes, as determined previously. The torsional stiffness of the deck was obtained using the formula [86]

$$G_s J_{eq} = G_s\left[J + \frac{E_s \Gamma_w \pi^2}{G_s L^2}\right] \tag{4-23}$$

where G_s is the steel shear modulus of elasticity, J_{eq} is the equivalent torsional constant, J is the pure torsion constant, E_s is the modulus of elasticity of steel, and L is the length of the main span.

Calculation of the mass of the deck considers the steel beams, rigid concrete slab, barriers and railings. To portray the behavior of the C-shaped section, the deck is represented as

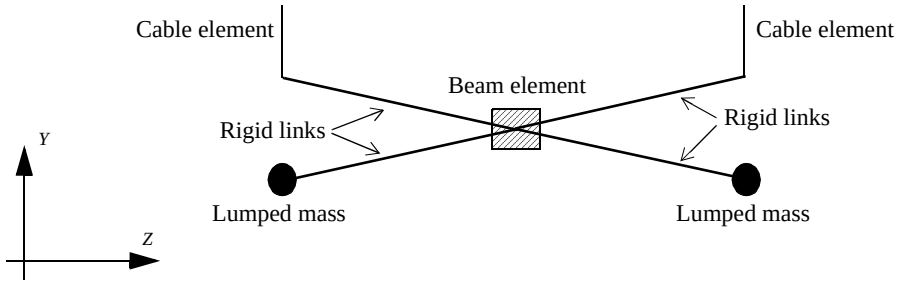

FIGURE 4-14. Finite Element Modeling of the Cross Section of the Deck

two lumped masses, each having a mass equal to half of the total mass of the deck. The masses are joined to the beam element by a rigid link as shown in Fig. 4-14. The vertical distance between the lumped mass and the center of the beam is equal to the distance between the shear center and the mass center of the C-shaped section shown in Fig. 4-13.

Because the mass moment of inertia of the main deck is different than the one induced by the lumped masses, it is necessary to make corrections to those quantities. In the calculation, the correction consists of finding the difference between the mass moment of inertia of the lumped masses and that of the actual deck section's mass moment of inertia. This difference in the mass moment of inertia is added to the node at the center of the deck to achieve the correct value of mass moment of inertia in the section model. The mass moment of inertia of the lumped masses with respect to the *j*-th axis (either the *X*, *Y*, or *Z* axis), I_j, is calculated using the formula

$$I_j = 2M_l r^2 \tag{4-24}$$

where M_l is the mass of each lumped mass, and r is the perpendicular distance from the mass to each axis. The actual mass moment of inertia of the deck with respect to the *j*-th axis, I_{mj}, is calculated using the equation

$$I_{mj} = \sum_{i=1}^{n} (I_{mi} + m_i r_i^2) . \tag{4-25}$$

where I_{mi} is the mass moment of inertia of each of the component of the deck with respect to its own centroidal axis, m_i is the mass of each component, and r_i is the perpendicular distance between the centroid of each component and the *j*-th axis. Thus, the corrected mass moment of inertia of the section becomes

$$\Delta_j = I_{mj} - I_j \tag{4-26}$$

The values of this parameter about each axis for a typical section of the deck are $\Delta_X = -4.43 \cdot 10^6 \text{ kg} \cdot \text{m}^2$, $\Delta_Y = -4.45 \cdot 10^6 \text{ kg} \cdot \text{m}^2$, and $\Delta_Z = 18.3 \cdot 10^3 \text{ kg} \cdot \text{m}^2$. Negative values indicate that the contribution of the lumped masses to the mass moment of inertia of the section is larger than the mass moment of inertia of the actual section. Thus, to achieve the correct mass moment of inertia for the section, a negative value is assigned to the spine to balance the larger value included by the lumped masses when the rigid links are condensed out. Reference [16] shows the importance of considering the C-shaped section of the deck for dynamic simulations.

Table 4-3 shows the first 10 natural frequencies of two models of the cable stayed bridge. The first model considers the C-shaped section of the deck and the second as described above and the second model consider lumped masses at the spine beam. Both models are deformed under dead loads before the modal parameters were obtained as discussed in section 4.1. By considering the C-shaped section, rotational modes decrease in frequency as shown by the 3th and 4th modes in table 4-3. In contrast vertical modes remain almost unchanged.

TABLE 4-3. Natural Frequencies of Lumped vs. C-shaped Sections

Nodal mass in the spine beam			C-Shaped section		
Freq No.	**Freq (Hz)**	**Mode Type**	**Freq No.**	**Freq (Hz)**	**Mode Type**
1	0.3328	Vertical	1	0.3317	Vertical
2	0.4285	Vertical	2	0.4266	Vertical
3	0.6103	Vertical	3	0.5086	Deck Rotational
4	0.6763	Vertical	4	0.5514	Deck Rotational
5	0.7328	Vertical	5	0.6108	Vertical
6	0.7418	Tower - Deck Torsion	6	0.6759	Vertical
7	0.7513	Tower - Deck Torsion	7	0.7324	Vertical
8	0.8589	Vertical	8	0.7634	Tower
9	0.9220	Transversal	9	0.7707	Tower - Deck Rotational
10	1.0278	Vertical	10	0.7786	Tower - Deck Rotational

To reproduce the effect of the shock absorbers installed in the bridge between the towers and the deck, constraint equations were used. The deck was allowed to displace in the longitudinal direction and rotate with respect to the vertical axis at the connections with the towers when the static loads where applied. For dynamic simulation these degrees of freedom were constrained to the movement of the towers. This reproduces the behavior of the shock absorbers which are locked by dynamic loads but allow movement under slow moving loads.

4.2.3 Nonlinear Static Analysis

The finite element model of the Emerson Bridge described in the last section was produced using the modified Newton-Raphson method as described in section 4.1. The typical load-displacement curve for a cable-stayed bridge is shown in Fig. 4-15. Due to the geometric configuration, the bridge deck *gains* stiffness when the dead load is applied [38]. When the original version of the Newton-Raphson method is used, the displacements

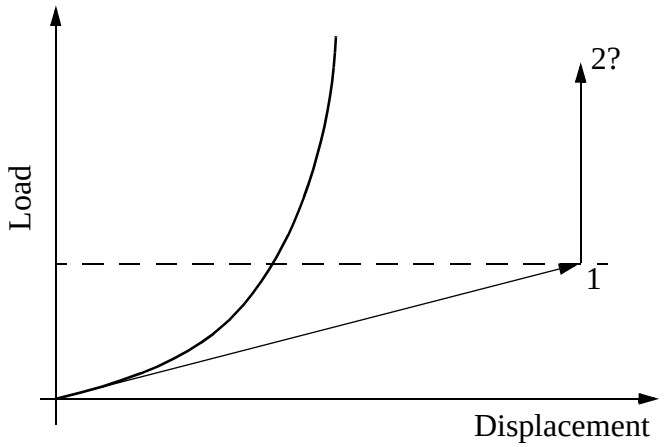

FIGURE 4-15. Load vs. Displacement Curve

obtained after the first iteration will produce displacements larger than what can be supported by the bridge (point 1 in Fig. 4-15). Thus, when calculating the stiffness matrix for the second iteration, instabilities are produced by the large internal forces produced by the displacements calculated in the first iteration (point 2 in Fig. 4-15).

To avoid these difficulties the modified version of the Newton-Raphson method was employed. Here 10% of the load error $\Delta\mathbf{P}_i$ is applied in each iteration (see Fig. 4-5), increasing the likelihood of convergence of the method. The drawback of this methodology is an increase in the number of iterations needed for convergence. The tolerance for convergence is

$$\text{Tolerance} = 100\frac{\Delta\mathbf{P}_i}{\max|\mathbf{P}|} \le 1, \tag{4-27}$$

where $\mathbf{P}$ is the loading vector and $\Delta\mathbf{P}_i$ is the loading error in the *i*-th iteration. This indicates that the iterations will be stopped when the maximum value of $|\Delta\mathbf{P}_i|$ is less than 1% the maximum value of $|\mathbf{P}|$. This procedure took approximately 80 iterations and 20 minutes of CPU time using a computer with Pentium 4 processor at 2 GHz.

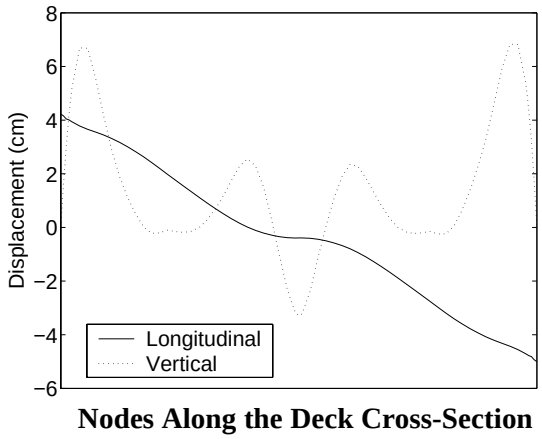

FIGURE 4-16. Deck Displacement

Figure 4-16 shows the displacements of the bridge under static loads. The vertical deflection at mid-span is 3.29cm (1.30in), and the maximum longitudinal deflection is 5cm (1.97in). The small vertical deflection in the deck shows good agreement between the dead loads and the pre-tension in the cables. The longitudinal displacement shown in Fig. 4-17 demonstrates that the deck is shortened by 9.23 cm (3.63 in), generating large axial forces in the structural members.

To demonstrate the approach, figure 4-17a shows the load vs. displacement at node 170 of the deck, located at 1/6th of the length of the main span. The vertical axis is the percentage of the dead load applied to the structure. Positive displacement is indicated when the deck displaces towards the ground. Negative displacements are obtained when less than 100% of the dead load is applied due to the pretension in the cables. The dotted line indicates the tangent stiffness at 90% of the dead load. Clearly, the stiffness of the deck increases when the dead load is applied, as mentioned in reference [38]. The load vs. longitudinal displacement of node 93 located at the top of one of the legs of Pier II is shown in Fig. 4-17b. In this graphic, positive displacement is toward the center of the bridge, and negative displacement is toward Bent 1. In contrast to the deck, the stiffness of the towers decreases

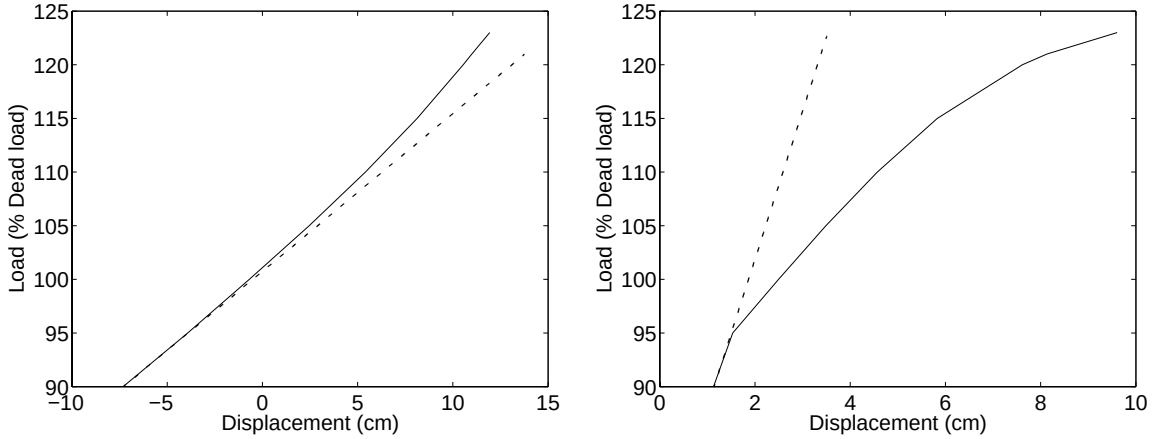

(a) Load vs. Vertical Displacement at node 170 (Deck)

(b) Load vs. Longitudinal Displacement at node 93 (Tower Top)

FIGURE 4-17. Load vs. Displacement

when the load is applied due to the effect of the large compressive forces generated by the cables.

The changes in the stiffness values play an important role in the dynamic properties of the structure. Table 4-4 shows the first 20 natural frequencies of the bridge before and after the nonlinear analysis. The first natural frequency is almost 13% higher after the nonlinear static analysis is performed clearly showing the increase in the stiffness of the bridge.

4.3 Damage Sensitivity

Using the finite element model of the Emerson Bridge discussed in the previous section, a study was performed to detect the variation of static and dynamic parameters to changes in the members of the deck. In this study damage is defined as a reduction in the Young's modulus of the material, which was reduced by 5%, 10%, 20% and 30%. Damage was induced in each of the 66 elements of the deck. After damage was induced in an element, a nonlinear static analysis was performed to obtain the new equilibrium position of the structure. The natural frequencies and the mode shapes of the new structure were

TABLE 4-4. Changes in the Natural Frequencies due to Nonlinearities

Nat. Freq.	Before (Hz)	After (Hz)	Difference (%)
1	0.2886 V	0.3317 V	12.98
2	0.3847 V	0.4266 V	9.81
3	0.4381 R	0.5086 R	13.87
4	0.4851 R	0.5514 R	12.02
5	0.5990 V	0.6108 V	1.93
6	0.6631 V	0.6759 V	1.90
7	0.6874 V	0.7324 V	6.14
8	0.6891 To	0.7634 To	9.73
9	0.7237 R	0.7707 R	6.09
10	0.7304 R	0.7786 R	6.19
11	0.7747 R	0.8457 R	8.39
12	0.8267 V	0.8582 V	3.66
13	0.8777 R	0.9202 R	4.62
14	0.9219 R	0.9206 R	-0.13
15	0.9226 T	0.9290 T	0.68
16	1.0038 R	1.0135 R	0.95
17	1.0290 V	1.0264 V	-0.25
18	1.0417 V	1.0741 V	3.01
19	1.0419 V	1.1060 V	5.7940
20	1.0701 R	1.1237 R	4.7663

V = Vertical; T = Transverse; R= Torsional; To = Tower

determined after the static nonlinear analysis and compared with the undamaged case. Although the nonlinear simulations and the modal analysis was performed with all the degrees of freedom of the bridge model, this study concentrates on the vertical degrees of freedom of the deck.

4.3.1 Sensitivity of Static Deflection to Damage

The sensitivity of the change of the deflection of the *r*-th node of the deck δ_r with respect to the change in the Young's modulus of the *s*-th element ΔE_s can be estimated numerically as

$$\frac{\Delta\delta_r}{\Delta E_s} = \frac{\delta_{r,\,\mathrm{u}} - \delta_{r,\,\mathrm{d}}}{\Delta E_s}, \tag{4-28}$$

where the subscript $(\ )_{\mathrm{u}}$ denotes the undamaged case and the subscript $(\ )_{\mathrm{d}}$ denotes the damaged case. The value of ΔE is 10GPa, 20GPa, 40GPa and 60GPa for the 5%, 10%, 20% and 30% reduction in the Young's modulus respectively. Figure 4-18 shows the sensitivity of the deck deflection for each damage case. These graphs show the sensitivity of the displacement of the *r*-th node of the deck with respect to changes in the Young's modulus in the *s*-th element. The peaks in every graph correspond to damage in elements 5 and 62, which produces a maximum displacement in nodes 6 and 62, respectively. Toward the middle of each plot, some peaks are observed for damage in members close to mid-span, which produce deflections at mid-span as well. In the 5% case the maximum displacement obtained from the original deformed shape is 0.07cms (0.03in) and in the 30% case 0.71cms (0.28 in). In a real application these values will be very difficult if not impossible to measure, particularly because the bridge will be in motion due to ambient excitation (e.g., wind, traffic). Note that the sensitivity plots are similar to the displacement plot shown in Fig. 4-16, indicating that displacements of the deck are particularly sensitive to changes in the Young's modulus of elements subject to higher moments.

Figure 4-19 shows the maximum absolute value of the sensitivity of the displacement for damage at each element. This is

$$\max\left|\frac{\Delta\delta}{\Delta E_s}\right|. \tag{4-29}$$

These plots are equivalent to observing the absolute value of the plots shown in Fig. 4-18 with respect to the "s" and vertical axis. In these graphs the sensitivity in the deflection of

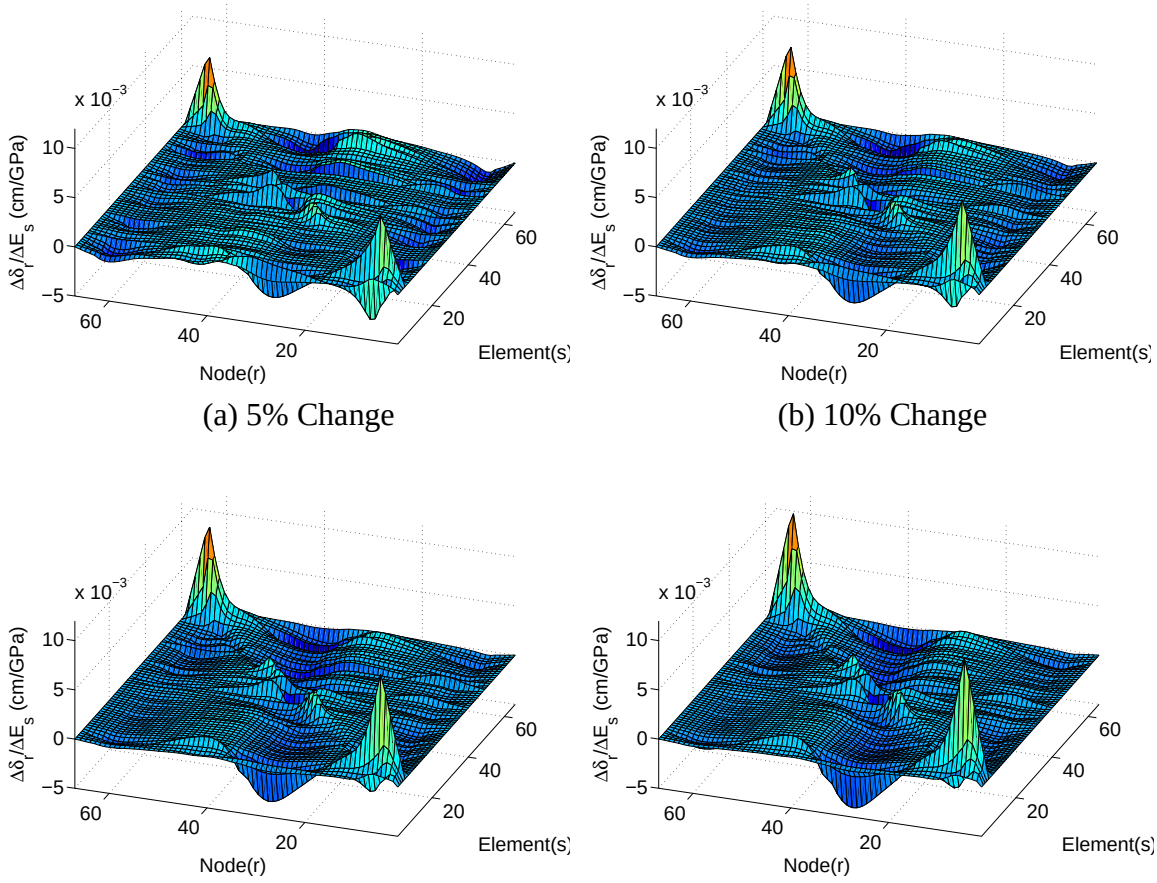

(a) 5% Change (b) 10% Change

(c) 20% Change (d) 30% Change

FIGURE 4-18. Sensitivity of the Static Displacement to Damage

elements 5 and 62 is more evident. Similarly the plots shown in Fig. 4-20 show the other side of figure 4-18. Here we can see the maximum sensitivity of each DOF in the deck due to changes in all the elements. In this graph, points 17 and 51 corresponding to the location of the two towers show no sensitivity to damage in the members because of the connection of the deck to the towers. From these plots we can observe that static displacement is more sensitive to damage when the displacement is measured further from the support of the deck. Thus, if a SHM technique based on static displacements is to be implemented, sensors should be located as far as possible from the supports.

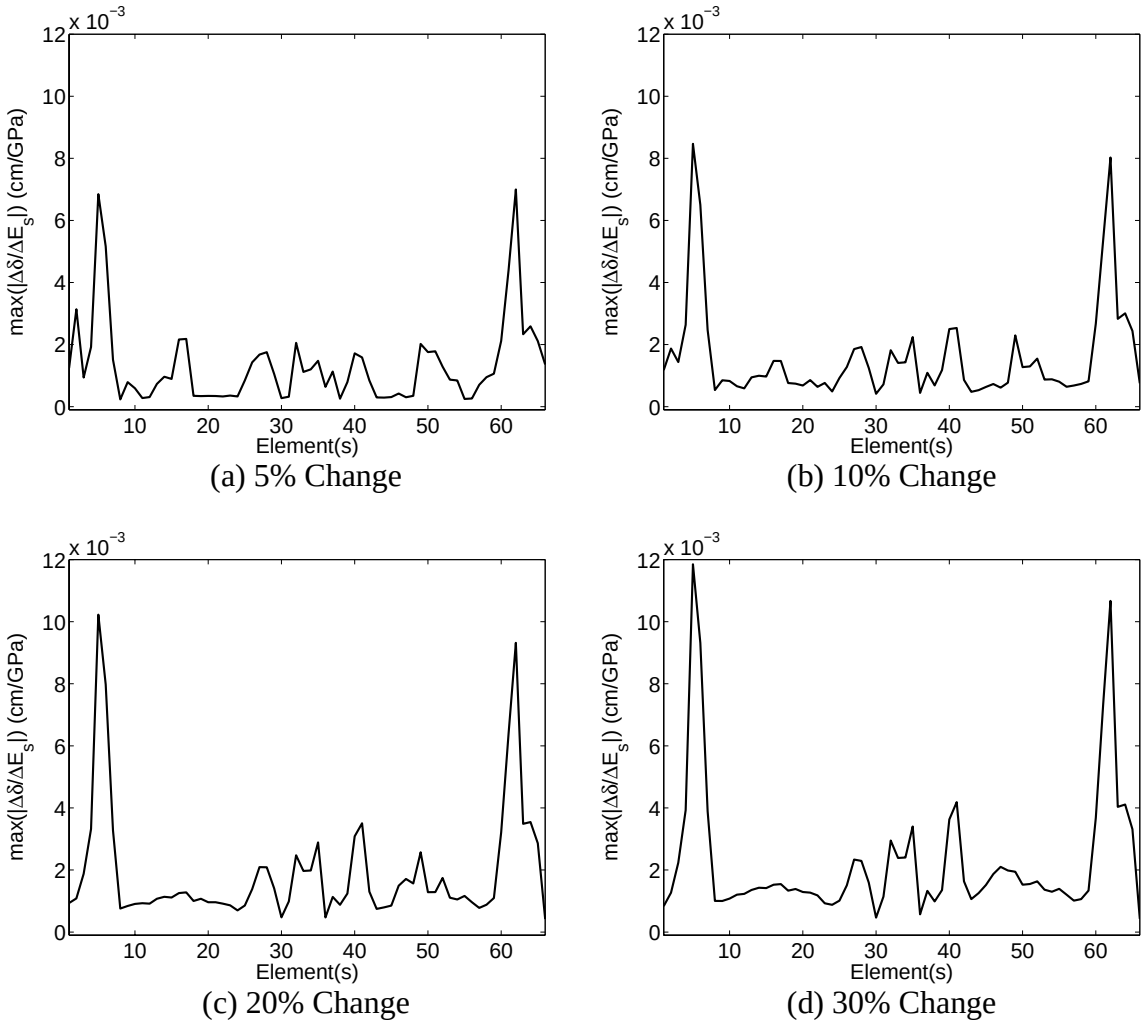

FIGURE 4-19. Sensitivity of the Static Displacement to Damage (Max Values per Element)

4.3.2 Sensitivity of Natural Frequencies to Damage

A sensitivity study is also performed to investigate the effect of damage on the natural frequencies. The sensitivity in the natural frequency is defined as

$$\frac{\Delta\omega_p}{\Delta E_s} = \frac{\omega_{p,\,\mathrm{u}} - \omega_{p,\,\mathrm{d}}}{\Delta E_s}, \tag{4-30}$$

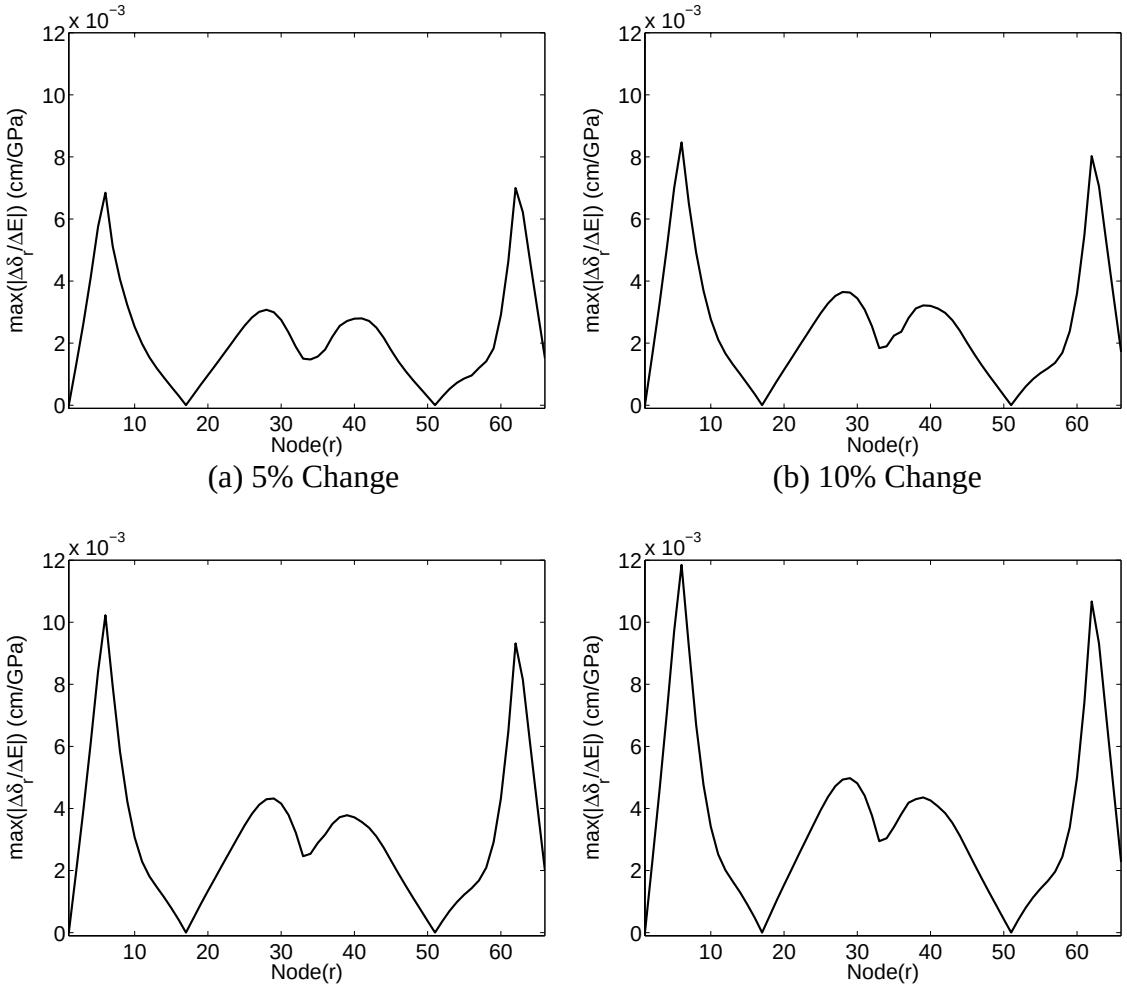

FIGURE 4-20. Sensitivity of the Static Displacement to Damage (Max Values per DOF)

where $\omega_{p,\,\mathrm{u}}$ is the *p*-th natural frequency of the undamaged model, and $\omega_{p,\,\mathrm{d}}$ is the *p*-th frequency of the damaged model. These values were calculated for the first 100 frequencies which are under 4Hz and are shown in Fig. 4-21. When damage occurs, the modes can change in order, and they may need to be sorted for a fair comparison. For the calculation of the sensitivity of the natural frequencies, special care was taken to compare

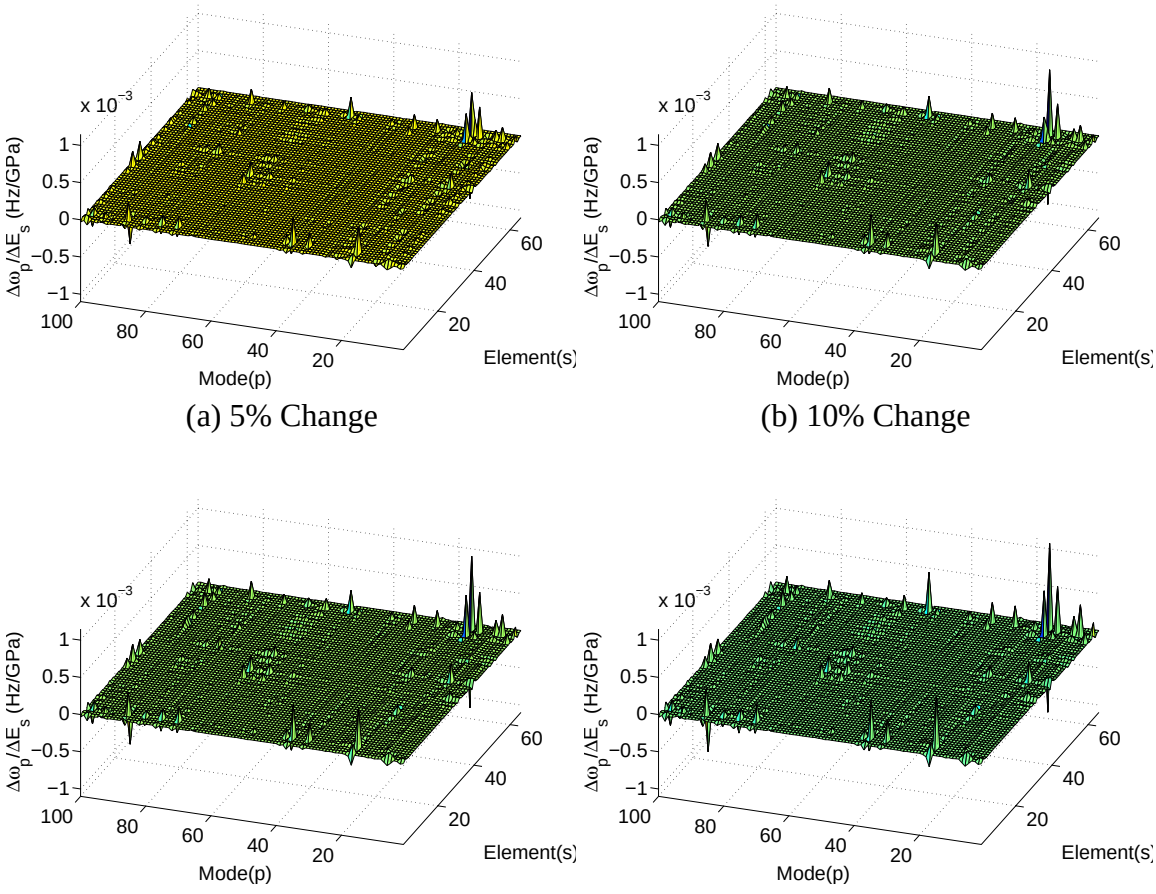

(a) 5% Change (b) 10% Change

(c) 20% Change (d) 30% Change

FIGURE 4-21. Sensitivity of the Natural Frequencies to Damage

the same mode shapes. The property of orthogonality of the mode shapes was used for this, as described in section 2.3.2.

Figures 4-22 and 4-23 show the maximum values per element and the maximum values per natural frequency of the sensitivity of the natural frequencies to changes in the Young's modulus. Based on these plots it is possible to state that the natural frequencies are not very sensitive to changes in Young's modulus. Only about 1×10^{-3} Hz/GPa is achieved. In the case of 5% change, a maximum variation of 0.008 Hz was found, and for

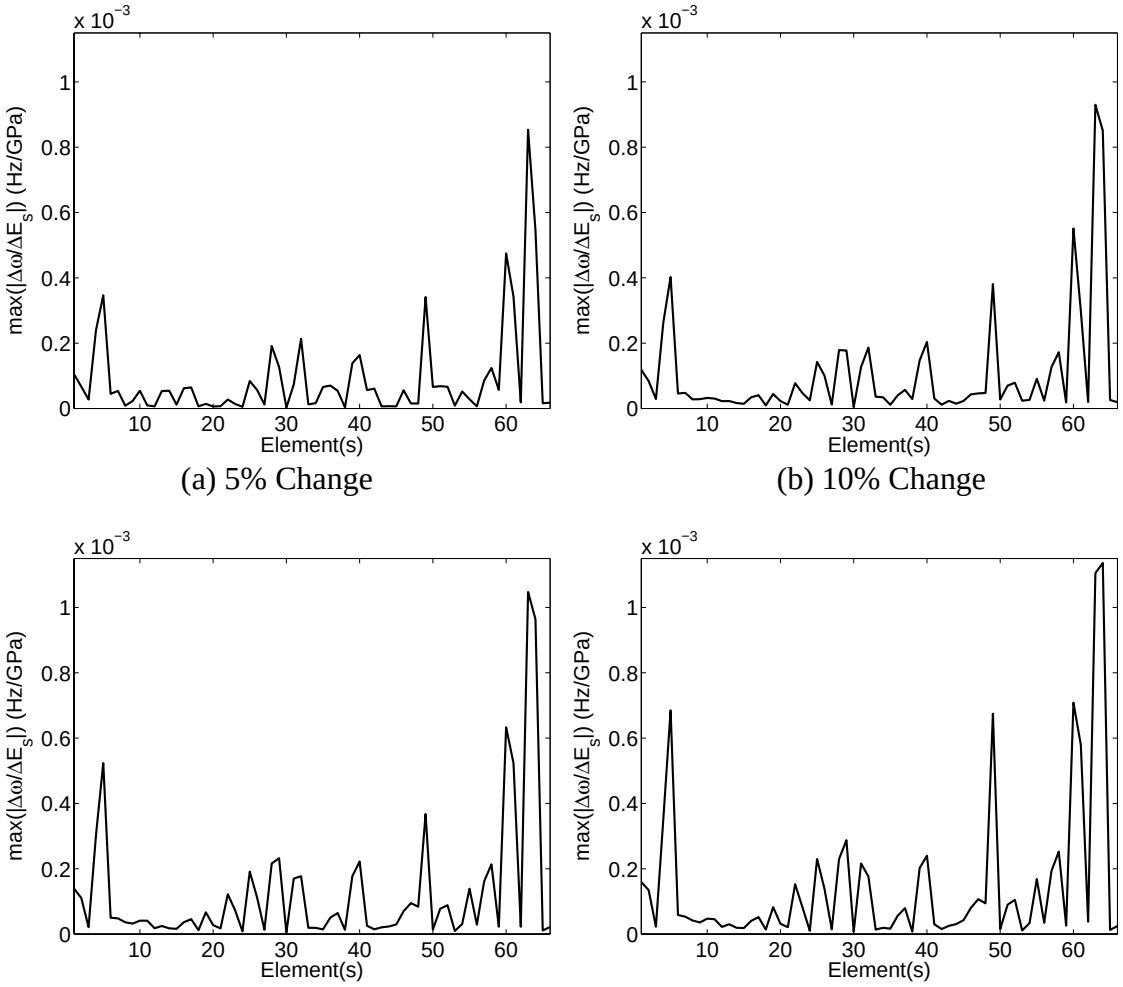

FIGURE 4-22. Sensitivity of the Natural Frequencies to Damage (Max Values per Element)

the 30% loss a maximum variation of 0.066 Hz was found. Thus, natural frequencies do not appear to be an appropriate parameter for damage detection in cable-stayed bridges.

Nevertheless we can observe in Fig. 4-23 that the sensitivity of the natural frequencies remains almost constant for all the damage scenarios studied. Thus, if a SHM technique based on the natural frequencies were to be developed, it would be possible to observe only the natural frequencies with higher sensitivity. This would be an important factor in placing sensors along the structure. Sensors could be located on the bridge to focus on

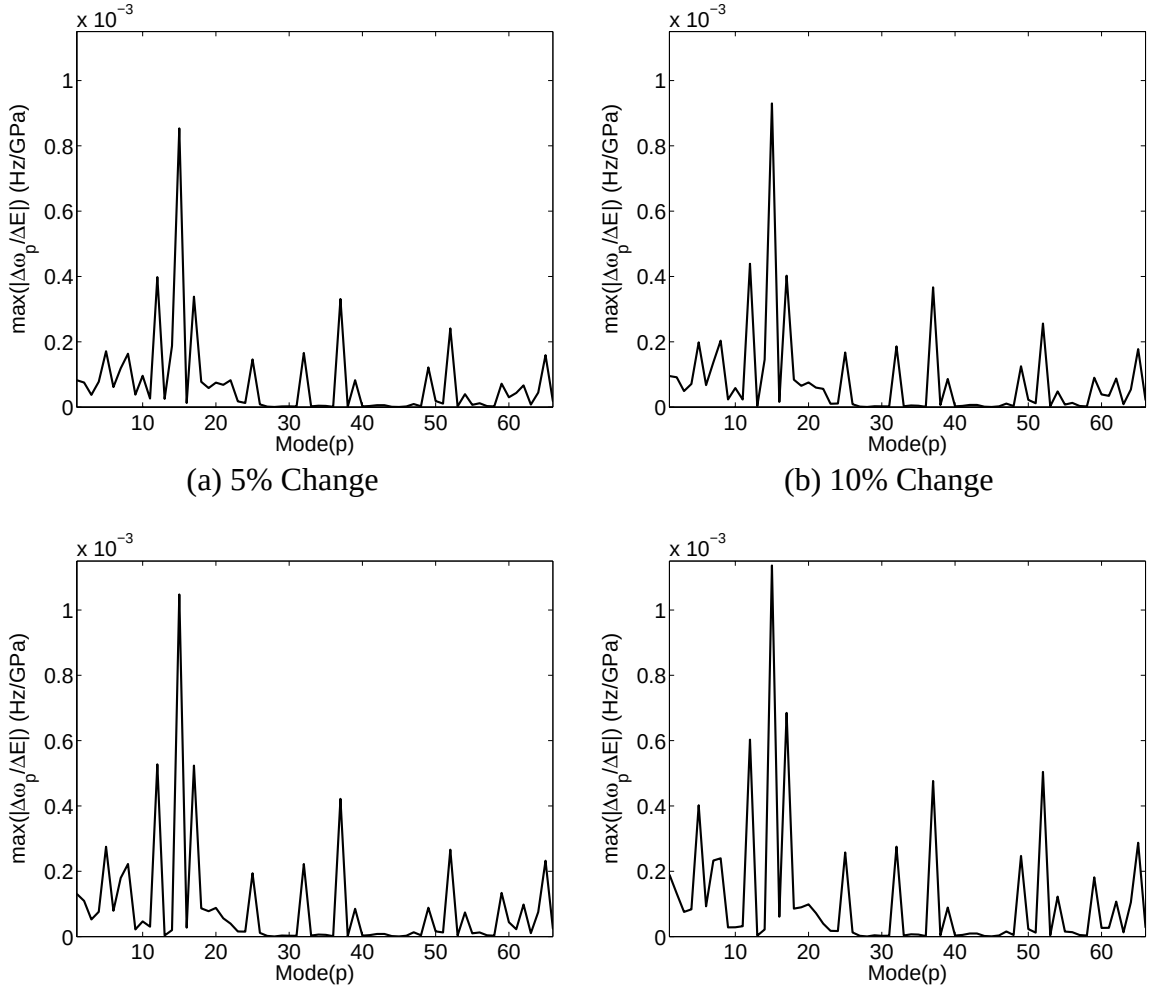

FIGURE 4-23. Sensitivity of the Natural Frequencies to Damage (Max Values per Natural Frequency)

these natural frequencies, which would reduce the number of sensors needed for the system.

4.3.3 Sensitivity of the Mode Shapes to Damage

The sensitivity of the mode shapes to changes in the Young's moduli of the sections of the deck is also studied. The sensitivity of the mode shape is defined as

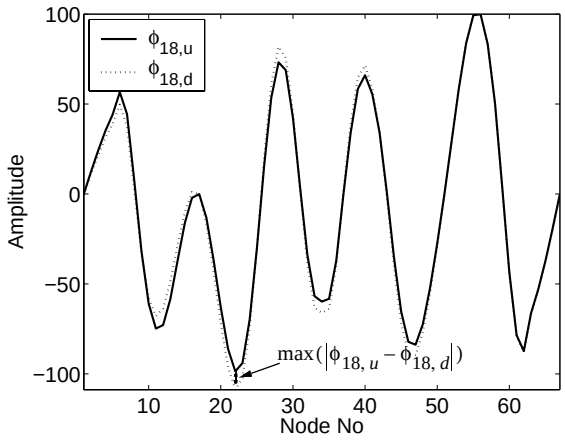

FIGURE 4-24. Mode 18 for the Undamaged and 10% Damage Cases

$$\frac{\Delta\phi_p}{\Delta E_s} = \frac{\max(|\phi_{p,u} - \phi_{p,d}|)}{\Delta E_s}, \tag{4-31}$$

where $\phi_{p,u}$ is the p-th mode shape for the undamaged structure and $\phi_{p,d}$ is the p-th mode shape for the damaged structure. The numerator of Eq. 4-31 will be the maximum difference between $\phi_{p,u}$ and $\phi_{p,d}$ as shown in Fig. 4-24. The mode shapes are normalized so the maximum value is equal to 100. Thus, the difference between the undamaged and damaged mode shapes is given as a percentage of the maximum displacement of the mode shape. In this study only modes corresponding to the vertical mode shapes of the deck for the first 100 natural frequencies are considered. These mode shapes correspond to modes 1, 2, 5, 6, 7, 12, 17, 18, 19, 25, 32, 37, 39, 49, 72, 77, 92, 98 and 100. These modes are selected because most of the excitation experienced by a cable-stayed bridge under ambient excitation is expected to be from traffic which will excite these modes. Although some of these are higher modes, the frequency range is between 0.33Hz for the first mode and 3.92Hz for the 100th mode, all of which are expected to be excited by ambient forces.

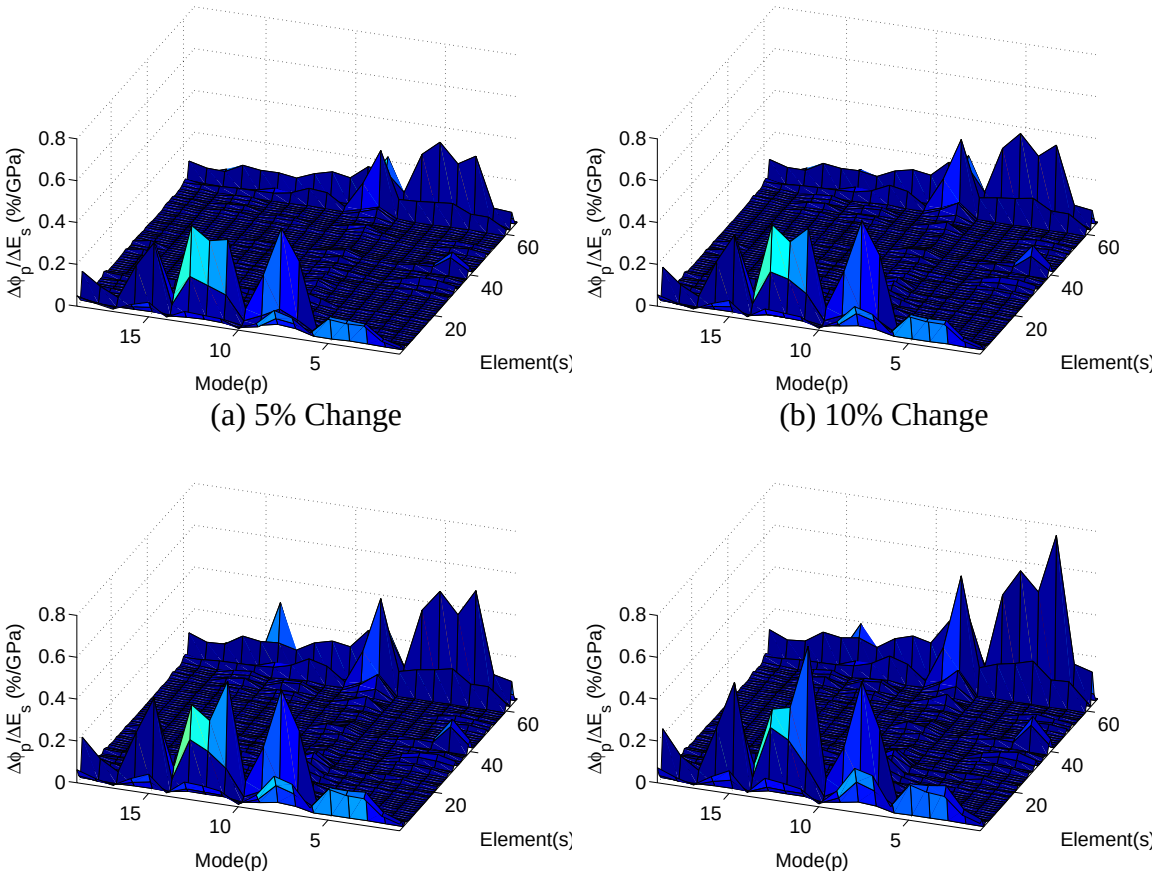

(a) 5% Change (b) 10% Change

(c) 20% Change (d) 30% Change

FIGURE 4-25. Sensitivity of the Mode Shapes to Damage

Figure 4-25 shows the sensitivity of the mode shapes to the changes in the Young's modulus. While the maximum value of the sensitivity for the static deflection and natural frequencies are approximately 6×10^{-3} cm/GPa and 8×10^{-4} Hz/GPa respectively, for the 5% damage case, the mode shapes have a maximum sensitivity of about 0.4%/GPa for the same case. Clearly the mode shapes are more sensitive than the frequencies and the static deflection. Thus, changes in the mode shapes appear to be the best indicators of damage for cable-stayed bridges.

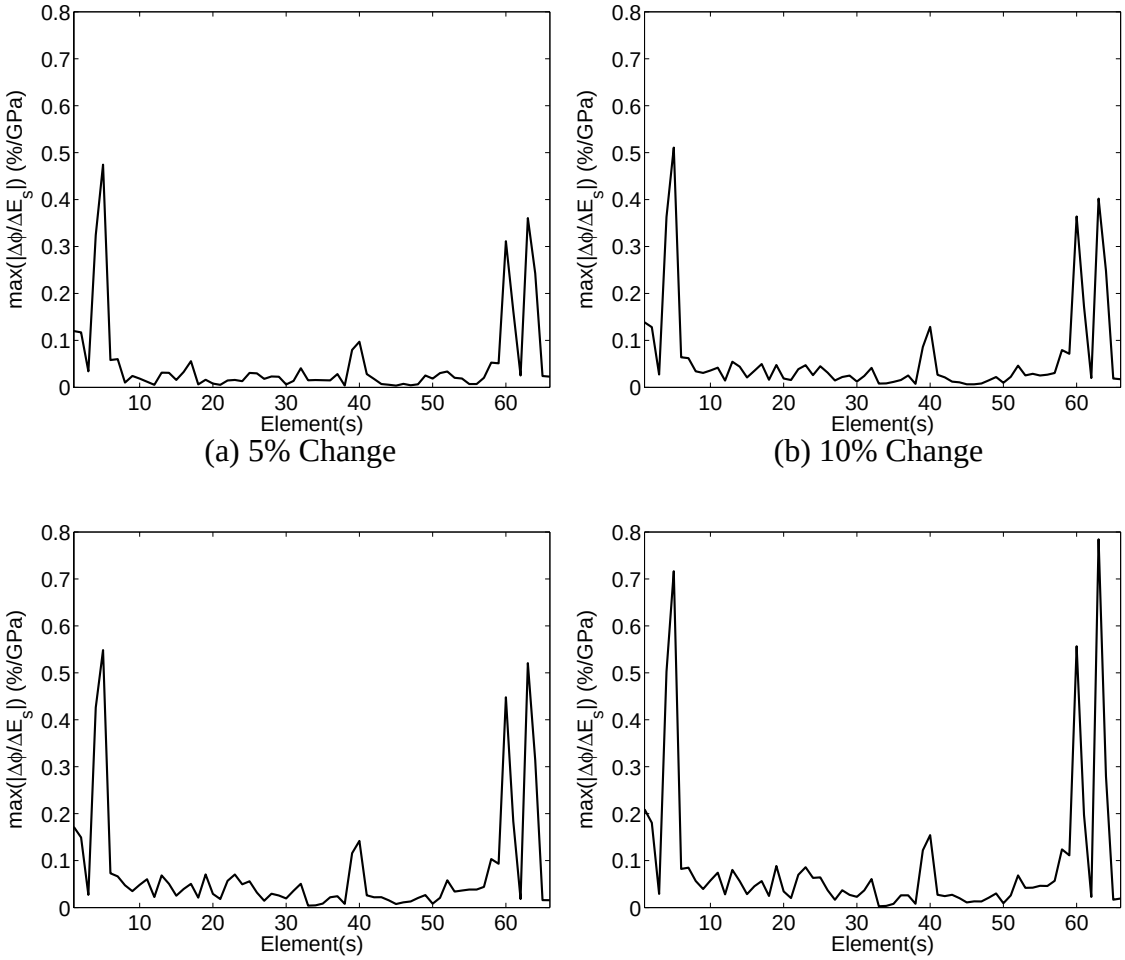

FIGURE 4-26. Sensitivity of the Mode Shapes to Damage (Max Values per Element)

Figure 4-26 shows the maximum values of Fig. 4-25 for each element on the deck. Similar to the static deflection, we can state that mode shapes are also more sensitive to damage in some elements than others. In the case studied, elements close to Bent I and Pier IV have a larger effect on the variation of the mode shapes of the structure. It was also found that the sensitivity is fairly constant for the different levels of damage studied.

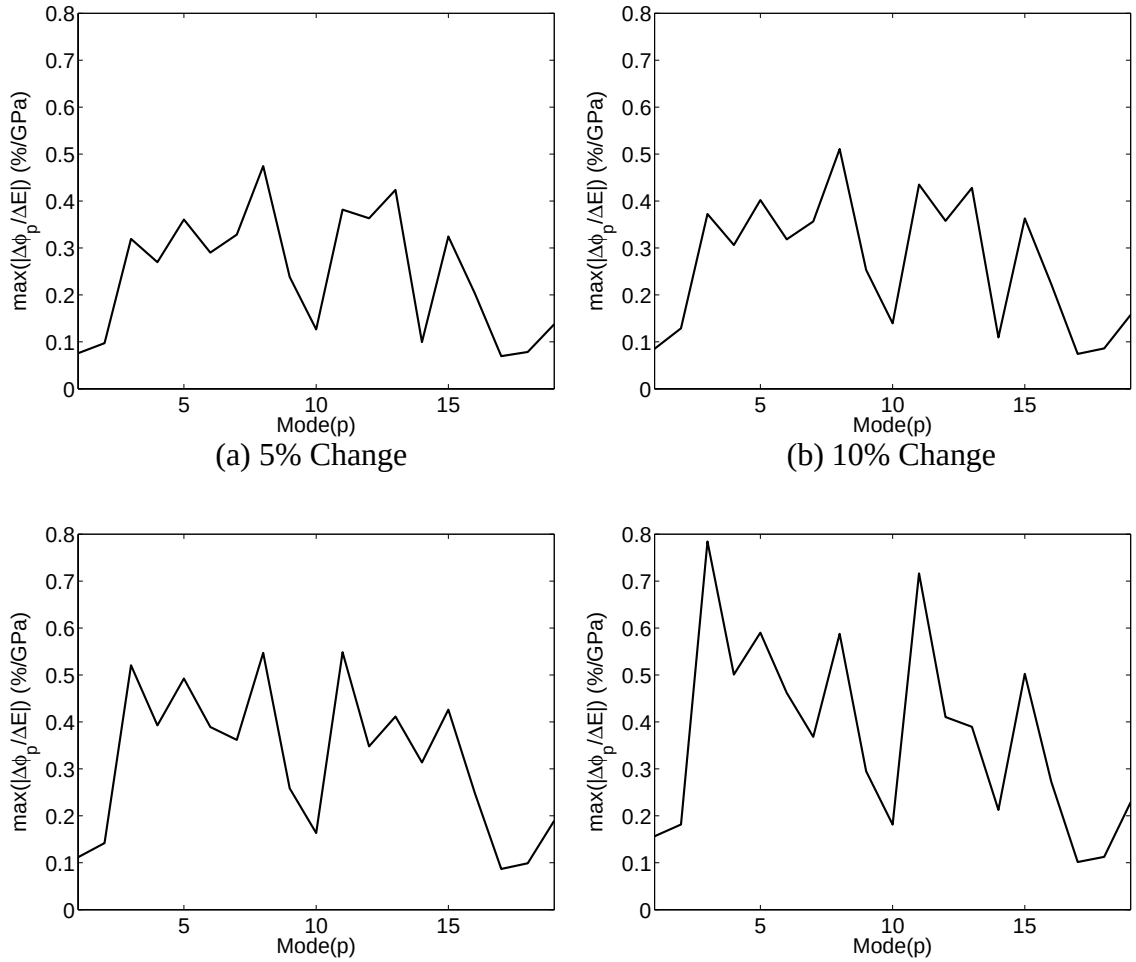

(a) 5% Change (b) 10% Change

(c) 20% Change (d) 30% Change

FIGURE 4-27. Sensitivity of the Mode Shapes to Damage (Max Values per Mode Shape)

Figure 4-27 shows the maximum values of Fig. 4-25 for each mode shape. In this graph we can observe that some mode shapes are more sensitive to the change in stiffness than others. For example, the 10th vertical mode shape is not as sensitive as the 11th mode shape. Consequently, the location of the sensors along the bridge deck should be optimized to obtain these mode shapes.

4.4 Summary

This chapter reviewed the methodology for the development of nonlinear static models of cable-stayed bridges due to sag in the cables, beam-column interaction, and changes in the geometry of the structure. A nonlinear static model of the Emerson Bridge was developed. For the construction of this model, two models of the deck were considered. The first model uses a massless spine beam with lumped masses at the nodes. The second model uses a modified version of the spine beam where the lumped masses are connected to rigid links to model the C-shaped section of the deck. It was found that the C-shaped section allowed the coupling between rotational and transverse modes of the bridge. Rotational modes displayed lower frequencies in the C-shaped model than in the spine beam model while vertical modes were unchanged.

Using the finite element model of the Bill Emerson Memorial bridge the effects of damage on the static displacement, natural frequencies and mode shapes was studied. Damage was modeled as 5%, 10%, 20% and 30% decrease in Young's modulus for all the deck members. A maximum change of 1.2×10^{-2} cm/GPa was found for the change in the static displacement of the bridge. The maximum change for the natural frequencies was 1×10^{-3} Hz/GPa. A change of 0.4%/GPa was found for the mode shapes, showing that they are the parameters most sensitive to damage in the deck.

Chapter 5

Numerical Implementation

This chapter describes a numerical implementation for the proposed structural health monitoring techniques described in chapter 2. The linear model of the Bill Emerson Memorial bridge discussed in chapter 4 is used. To reduce the complexity of the problem, only vibration in the *X*-*Z* plane of the model is considered (longitudinal and vertical axes). This plane was selected because most of the ambient vibration in the structure is expected to be from traffic excitation. Thus, the vertical modes of the structure are expected to be excited more than the horizontal and rotational modes.

Damage is induced by decreasing, the Young's moduli of the deck members. Acceleration records are obtained from simulations performed using a state-space representation of the structure, and are used to determine the natural frequencies and mode shapes using NExT and ERA. Then, the least squares solution of the eigenvalue problem is used to detect the changes in the Young's moduli, identifying the location and amount of damage in the structure.

Dynamic records of the structure are required by the SHM methodologies discussed in this dissertation. The techniques will be tested on the numerical model by introducing damage and comparing the resulting parameters for the healthy and damaged structure. The techniques use ambient vibration to obtain the modal properties of the structure. These ambient vibrations will create small amplitudes, and we assume the structure will behave linearly.

In the first section of this chapter various identification models for structural parameter estimation are studied. The number of sensors needed for the implementation of the least squares solution of the eigenvalue problem is smaller for each model, in an effort to obtain a model that can potentially be used on the actual structure. Table 5-1 shows a summary of the different identification models studied in this section.

TABLE 5-1. Summary of Identification Models

Model No.	# DOF	Comments
1	449	Damage identified
2	194	Modeling errors introduced a small bias error. Damage identified
3	142	Identification not possible due to modeling errors.
4	62	Identification possible in a portion of the deck with partial instrumentation.

In the following section a description of the state space representation of the structure is provided. Here it is used to obtain acceleration records of the structure. A modal representation is used to increase the speed of the simulations. Then, the modal identification techniques (NExT and ERA) are used to detect the mode shapes and natural frequencies of the structure from the acceleration records calculated with the state space representation of the bridge. Here, the methods are tested for the special case of large structures with closely spaced modes. In the last section of this chapter the complete methodology is used to study two cases scenarios.

5.1 Identification Model

An identification model of the Bill Emerson Memorial bridge is developed herein. This model facilitates implementation of the parameter identification techniques described in chapter 2. The model focuses on the identification of damage in the deck members, although the conclusions obtained in this chapter can be applied to the other members of the bridge.

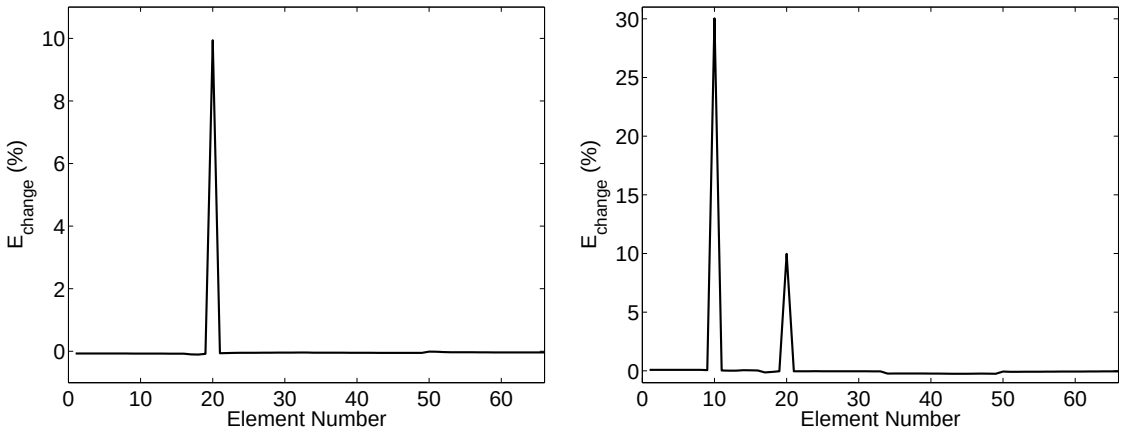

(a) 10% damage in element 20

(b) 10% damage in element 20 and 30% damage in element 10

FIGURE 5-1. Change in the Identified Stiffness for the First Identification Model

Two types of models of the structure are used in this section. The first type is used to calculate the "exact" natural frequencies and mode shapes of the structure, and it is denoted the "real model". The "real model" represents the real structure to be identified. This model describes the behavior of the structure in the *X*-*Z* plane (longitudinal and vertical axes) and has a total of 449 active degrees of freedom. The second type of model is used to identify the parameters of the structure based on the natural frequencies and mode shapes obtained from the real model (*e.g.*, Young's modulus). Models of this type are denoted "identification models". Different identification models are tested using the first 10 exact mode shapes and natural frequencies of the real model. These tests allow for the determination of the effects of the towers and the cables in the identification process.

The first identification model used is identical to the real model. Consequently, no modeling errors are expected. In this study the stiffness values of the cables and the tower elements are assumed to be known in order to focus on the deck. Figure 5-1 shows the identified change in the stiffness due to a 10% reduction in element 20, and 10% and 30% reductions in elements 20 and 10, respectively. The change in stiffness is defined as

$$\mathbf{E}_{change}(\%) = 100 \times \frac{\mathbf{E}_{undamaged} - \mathbf{E}_{damaged}}{\mathbf{E}_{undamaged}}, \quad (5\text{-}1)$$

where $\mathbf{E}_{undamaged}$ and $\mathbf{E}_{damaged}$ are vectors representing the identified undamaged and damaged Young's moduli.

In this case the methodology is able to identify the location and amount of damage. This first identification model has a total of 449 DOF. Having 449 sensors in a real implementation will be difficult with the current capabilities of data acquisition systems, although is likely to be possible in the future. Still, the 449 DOF model does not represent all motions in a full bridge.

A second identification model is studied to consider its capabilities for damage detection. For the second identification model the nodes at the towers are constrained, reducing the number of active degrees of freedom in the identification model and the number of sensors needed to 194. These 194 DOF include the vertical and longitudinal accelerations as well as the rotational accelerations of every node in the deck. Figure 5-2 shows the same cases as Fig. 5-1 for the second identification model. A small bias error is observed in the non-damaged members due to modeling errors in the identification model. This bias error tends to increase with higher values of damage.

The third evaluation model adds restraints on the longitudinal accelerations in the deck. This reduces the number of active degrees of freedom in the identification model to 142 and includes further modeling errors in the identification process. Figure 5-3 shows the change in the identified stiffness for the same cases shown for the previous identification models. In this case the modeling errors do not allow the identification of damage in the structure, showing that the longitudinal acceleration is an important factor for this bridge.

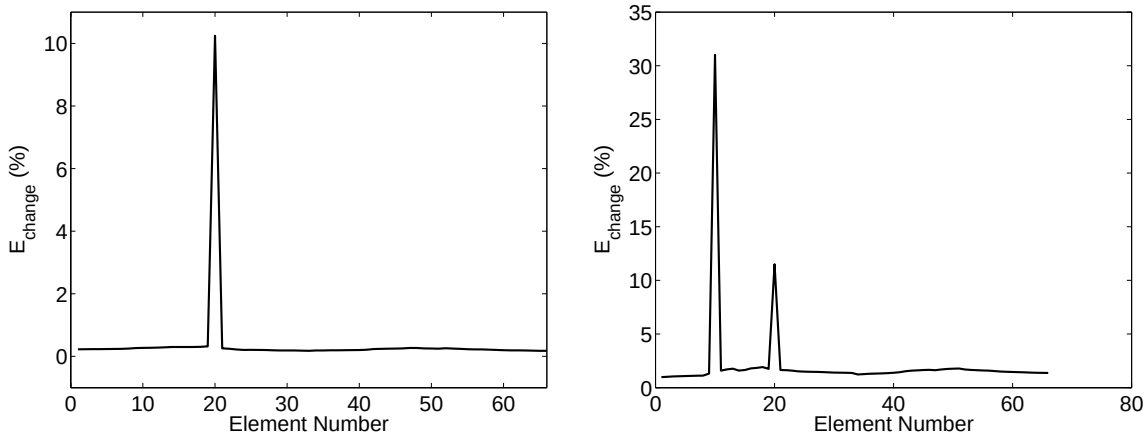

(a) 10% damage in element 20

(b) 10% damage in element 20 and 30% damage in element 10

FIGURE 5-2. Change in the Identified Stiffness for the Second Identification Model

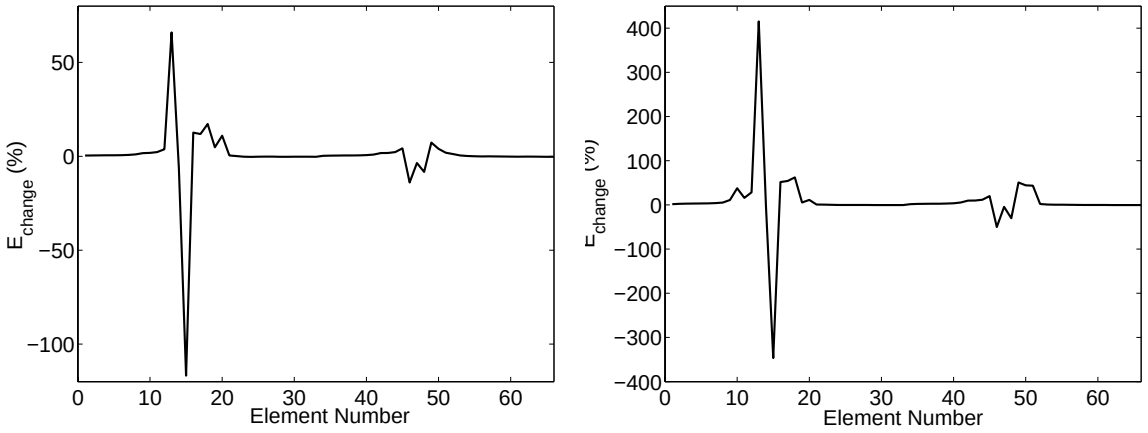

(a) 10% damage in element 20

(b) 10% damage in element 20 and 30% damage in element 10

FIGURE 5-3. Change in the Identified Stiffness for the Third Identification Model

This result is due to the boundary conditions for this bridge, which allow longitudinal displacements of the deck at Bent I and Pier IV as discussed in the previous chapter. Similar results are obtained when the rotations in the deck are restrained, showing that in cable-stayed bridges, the rotations are important in the determination of the stiffness. Figure 5-4 shows the vertical, longitudinal and rotational components of the first mode of vibration (deck DOF). This result is in contrast with the results of the benchmark structure

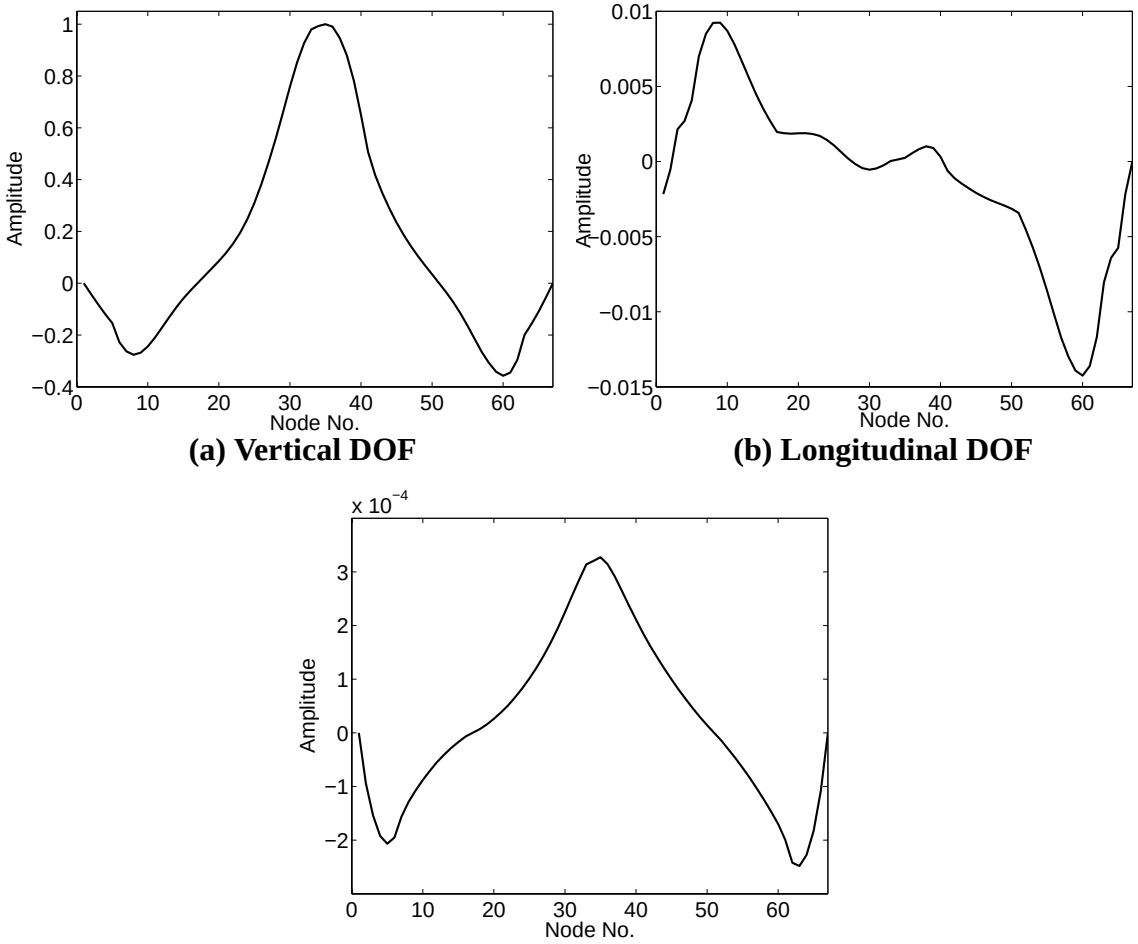

(a) Vertical DOF

(b) Longitudinal DOF

(c) Rotational DOF

FIGURE 5-4. First Mode of Vibration

discussed in chapter 3. In that case, the rotation of the floors of the structure are so small, they do not play an important factor in the identification of the structural parameters.

The fourth identification model was constructed to study the possibility of dividing the deck into several substructures. This model has only the degrees of freedom of the deck between Bent 1 and Pier II. Damage between elements 1 and 16 may be identified by this model, and damage outside these elements should not affect the identified change in stiffness. Figure 5-5 shows the stiffness change for this identification model for the same cases studied previously. This model successfully identifies the damage in the 10th

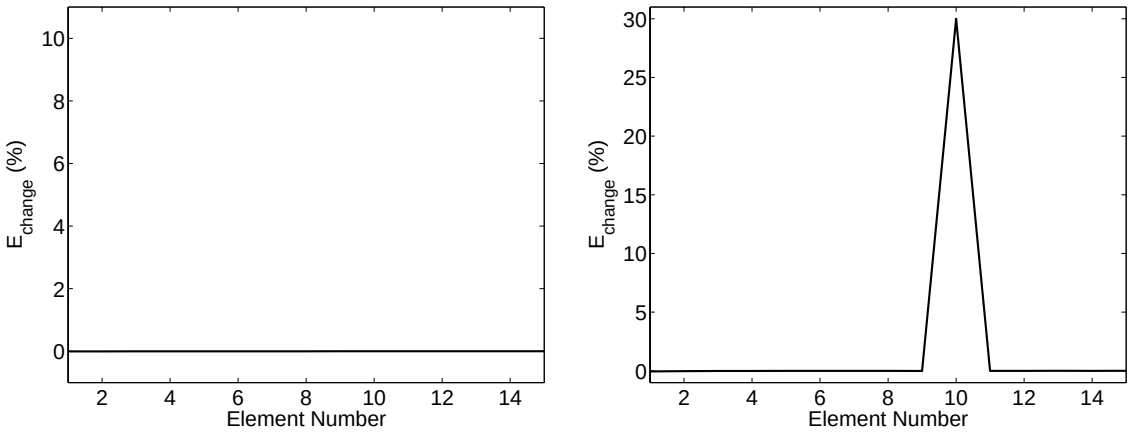

(a) 10% damage in element 20

(b) 10% damage in element 20 and 30% damage in element 10

FIGURE 5-5. Change in the Identified Stiffness for the Fourth Identification Model

element and it is not affected by damage in element 20, showing that the identification procedure can be used for sub-structures. This will allow us to have sensors only in the critical parts of the structure or in places with difficult access. This fourth identification model has a total of 62 DOF.

The fourth model is used as the identification model in the remainder of this chapter. A total of 62 acceleration measurements will be obtained from the dynamic simulations including the longitudinal, vertical and rotational accelerations for every node in the deck between Bent I and Pier II.

5.2 Modal Identification

This section discusses the experiences obtained with the modal identification techniques discussed in chapter 2. In the first part of this section a description of the state-space representation of the bridge is discussed. This was used to calculate the acceleration records used by the modal identification methodologies. In the second part of this section the results obtained with NExT and the ERA are presented.

5.2.1 State Space Representation

For the dynamic simulations of the structure a state-space representation of the bridge was determined. Consider the equation of motion of a multi-degree of freedom system

$$\mathbf{M}\ddot{\mathbf{x}}(t) + \mathbf{C}\dot{\mathbf{x}}(t) + \mathbf{K}\mathbf{x}(t) = \mathrm{F}(t), \tag{5-2}$$

where $\mathbf{M}$, $\mathbf{C}$ and $\mathbf{K}$ are the mass, damping and stiffness matrices, $\mathbf{x}(t)$ is the vector of displacements at time t, $\mathbf{F}(t)$ is the vector of forces at time t, and $(\dot{})$ indicates derivative with respect to time. By selecting the displacements and velocities as states, Eq. 5-2 can be written as

$$\dot{\mathbf{x}}_s(t) = \tilde{\mathbf{A}}\mathbf{x}_s(t) + \tilde{\mathbf{B}}\mathbf{F}(t) \tag{5-3}$$

$$\mathbf{y}(t) = \tilde{\mathbf{C}}\mathbf{x}_s + \tilde{\mathbf{D}}\mathbf{F}(t), \tag{5-4}$$

where $\mathbf{x}_s(t)$ are the states, $\mathbf{y}(t)$ are the outputs of the system and matrices $\mathbf{A}$, $\mathbf{B}$, $\mathbf{C}$ and $\mathbf{D}$ define the state-space representation. To obtain displacements, velocities and accelerations as the outputs of the state space representation, these matrices are

$$\tilde{\mathbf{A}} = \begin{bmatrix} \mathbf{0} & \mathbf{I} \\ -\mathbf{M}^{-1}\mathbf{C} & -\mathbf{M}^{-1}\mathbf{K} \end{bmatrix}; \tilde{\mathbf{B}} = \begin{bmatrix} \mathbf{0} \\ \mathbf{M}^{-1} \end{bmatrix}; \tilde{\mathbf{C}} = \begin{bmatrix} \mathbf{I} & \mathbf{0} \\ \mathbf{0} & \mathbf{I} \\ -\mathbf{M}^{-1}\mathbf{C} & -\mathbf{M}^{-1}\mathbf{K} \end{bmatrix}; \tilde{\mathbf{D}} = \begin{bmatrix} 0 \\ 0 \\ -\mathbf{M}^{-1} \end{bmatrix}, \tag{5-5}$$

where $\mathbf{0}$ and $\mathbf{I}$ are zero and identity matrices of appropriate dimensions, respectively.

The stiffness, damping and mass matrices are decomposed into modal coordinates to increase the speed of the simulations and to focus on the modal parameters of the

frequency range of interest [23]. Equation 5-2 describes the motion of a multi-degree of freedom system and is repeated here

$$\mathbf{M}\ddot{\mathbf{x}}(t) + \mathbf{C}\dot{\mathbf{x}}(t) + \mathbf{K}\mathbf{x}(t) = \mathrm{F}(t) \tag{5-6}$$

The displacement of the structure, $\mathbf{x}(t)$, can be decomposed in terms of modal coordinates

$$\mathbf{x}(t) = \sum_{r=1}^{N} \phi_r q_r(t) = \Phi\mathbf{q}(t), \tag{5-7}$$

where ϕ_r is the r-th mode shape, $q_r(t)$ is the r-th modal coordinate, N is the number of degrees of freedom, Φ is the matrix of mode shapes and $\mathbf{q}$ is the vector of modal coordinates. Replacing Eq. 5-7 in Eq. 5-6 gives

$$\mathbf{M}\Phi\ddot{\mathbf{q}}(t) + \mathbf{C}\Phi\dot{\mathbf{q}}(t) + \mathbf{K}\Phi\mathbf{q}(t) = \mathbf{F}(t). \tag{5-8}$$

Premultiplying Eq. 5-6 by Φ^T yields

$$\hat{\mathbf{M}}\ddot{\mathbf{q}}(t) + \hat{\mathbf{C}}\dot{\mathbf{q}}(t) + \hat{\mathbf{K}}\mathbf{q}(t) = \hat{\mathbf{F}}(t), \tag{5-9}$$

where

$$\hat{\mathbf{M}} = \Phi^T\mathbf{M}\Phi,\ \hat{\mathbf{C}} = \Phi^T\mathbf{C}\Phi,\ \hat{\mathbf{K}} = \Phi^T\mathbf{K}\Phi, \text{ and } \hat{\mathbf{F}}(t) = \Phi^T\mathbf{F}(t). \tag{5-10}$$

To reduce the dimension of the system only a limited number of mode shapes are used in the construction of Φ. By selecting the first 20 modes of the structure, the size of the numerical model is significantly reduced, preserving the same dynamic characteristics below the 20th mode. The sampling rate used for the time simulations can also be reduced

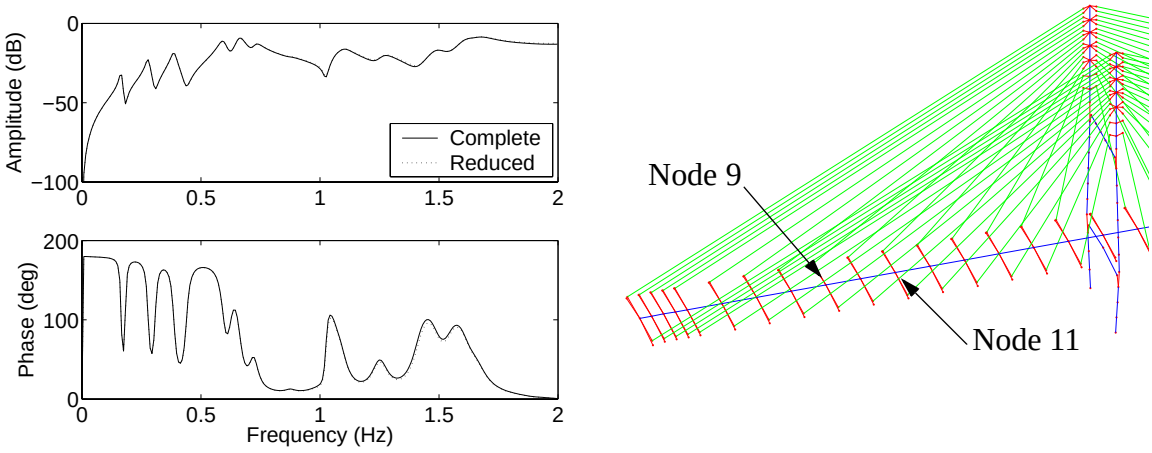

FIGURE 5-6. Transfer Functions of Complete and Reduced System

without creating any errors in the simulation due to higher modes. Using Eq. 5-9 to form the state-space representation of the system, a model with 40 states was obtained. The transformation between modal coordinates and displacement, velocity and acceleration can be included in the state-space representation by premultiplying the $\tilde{\mathbf{C}}$ and $\tilde{\mathbf{D}}$ matrices by the modal matrix Φ

$$\tilde{\mathbf{C}} = \begin{bmatrix} \Phi & \Phi & \Phi \end{bmatrix} \begin{bmatrix} \mathbf{I} & \mathbf{0} \\ \mathbf{0} & \mathbf{I} \\ -\mathbf{M}^{-1}\mathbf{C} & -\mathbf{M}^{-1}\mathbf{K} \end{bmatrix}, \tag{5-11}$$

$$\tilde{\mathbf{D}} = \begin{bmatrix} \Phi & \Phi & \Phi \end{bmatrix} \begin{bmatrix} 0 \\ 0 \\ -\mathbf{M}^{-1} \end{bmatrix}. \tag{5-12}$$

Figure 5-6 shows the transfer functions between vertical force at node 9 and vertical acceleration at node 11 for the complete (850 states) and reduced (40 states) systems. These two nodes are located between Bent I and Pier II in the deck as shown in the figure.

The reduction had little effect on the dynamic characteristics of the system in the range of interest.

Another option to increase the speed of the simulations is to reduce some degrees of freedom in the finite element model before forming the state-space model using static condensation. Static condensation starts by dividing the stiffness and mass matrices into active and condensed degrees of freedom [23].

$$\mathbf{K} = \begin{bmatrix} \mathbf{K}_{a,\,a} & \mathbf{K}_{a,\,c} \\ \mathbf{K}_{c,\,a} & \mathbf{K}_{c,\,c} \end{bmatrix}; \; \mathbf{M} = \begin{bmatrix} \mathbf{M}_{a,\,a} & \mathbf{M}_{a,\,c} \\ \mathbf{M}_{c,\,a} & \mathbf{M}_{c,\,c} \end{bmatrix}, \tag{5-13}$$

where the subscript $(\;)_a$ stands for active and $(\;)_c$ for condensed degree of freedom. Assuming that no loads are applied to the condensed degrees of freedom, static equilibrium can be written as

$$\begin{bmatrix} \mathbf{K}_{a,\,a} & \mathbf{K}_{a,\,c} \\ \mathbf{K}_{c,\,a} & \mathbf{K}_{c,\,c} \end{bmatrix} \begin{bmatrix} \mathbf{x}_a \\ \mathbf{x}_c \end{bmatrix} = \begin{bmatrix} \mathbf{F} \\ \mathbf{0} \end{bmatrix}, \tag{5-14}$$

The relation between the active and all degrees of freedom is written as

$$\begin{bmatrix} \mathbf{x}_a \\ \mathbf{x}_c \end{bmatrix} = \mathbf{T}\mathbf{x}_a, \tag{5-15}$$

where the transformation matrix $\mathbf{T}$ can be obtained from Eq. 5-14 as

$$\mathbf{T} = \begin{bmatrix} \mathbf{I} \\ -\mathbf{K}_{cc}^{-1}\mathbf{K}_{ca} \end{bmatrix}. \tag{5-16}$$

The reduced stiffness and mass matrices are then

$$\hat{\mathbf{M}} = \mathbf{T}^T\mathbf{M}\mathbf{T}; \hat{\mathbf{K}} = \mathbf{T}^T\mathbf{K}\mathbf{T}. \quad (5\text{-}17)$$

Note that, using this reduction technique, some errors will be introduced because the transformation matrix $\mathbf{T}$ is based on static equation and does not include the mass and damping matrices. Although this reduction has been found effective to form a reduced order model of the structure [34], the reduction using modal decomposition was used in this study because a more significant reduction can be achieved with minimum impact in the structural model.

5.2.2 Modal ID with NExT and ERA

Independent broad-band random excitations are generated with the Matlab command *randn* for simulation of the bridge response. The excitation is applied to all the vertical nodes of the bridge deck simulating random traffic loads. Figure 5-7 shows one minute of the force used in the simulations. A linear simulation of the bridge is performed using the state-space representation described in section 5.2.1. The Matlab command *lsim* is used to calculate the response of the system. A sampling frequency of 20 Hz and sample length of 31 minutes are used in the simulation. The first minute of each of the acceleration records is neglected to avoid including transient data in the identification process. Although the time used for the analysis seems long, 30 minutes records 529 cycles at the first natural frequency of the bridge (0.29 Hz). This time is comparable to the 540 cycles that a building with first natural frequency of 9Hz would have in a one minute record (chapter 3).

After the simulation the acceleration records were resampled to 3 Hz using the Matlab command *resample*. This approach allows us to identify modes up to 1.5 Hz, covering the

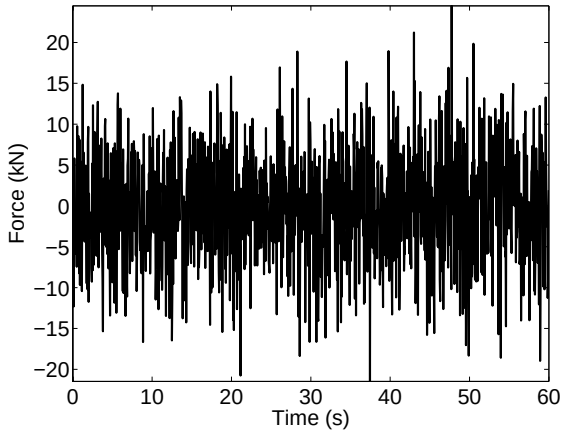

FIGURE 5-7. Typical Force Record

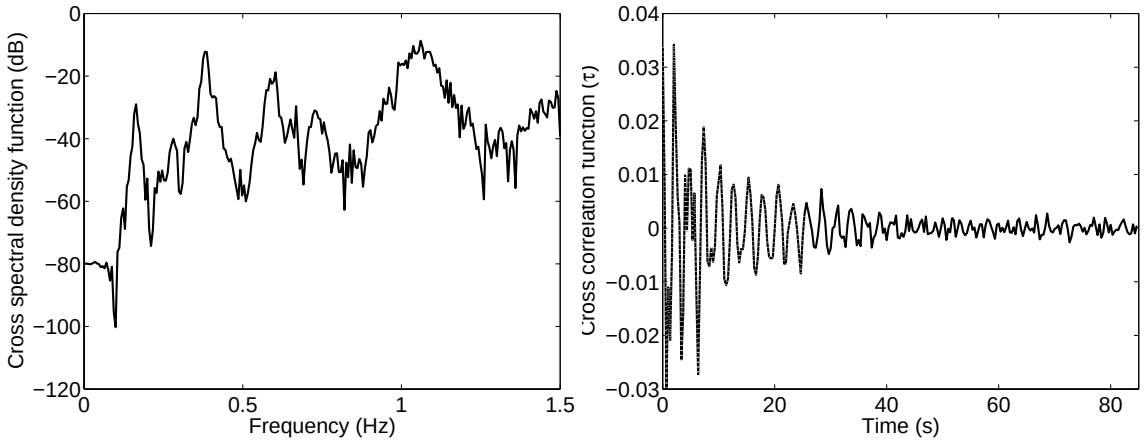

(a) Cross spectral density function (b) Cross correlation function

FIGURE 5-8. Typical Cross Spectral Density and Cross Correlation Functions

first 12 vertical modes of the bridge corresponding to 0.293, 0.391, 0.602, 0.664, 0.730, 0.879, 1.03, 1.07, 1.10, 1.26 and 1.49 Hz.

The Natural Excitation Technique (NExT) and the Eigensystem Realization Algorithm (ERA) are applied to the acceleration records for the identification of natural frequencies, mode shapes and damping ratios. When calculating the cross spectral density function, a boxcar window of 512 points and 75% overlapping between frames is used. Figure 5-8 shows typical cross spectral density and cross correlation functions.

In the ERA, 77 points of the cross spectral density functions are used to form a 40 by 1200 Hankel matrix. This corresponds to the dotted line in the cross correlation function shown in Fig. 5-8. In selecting the size of the Hankel matrix, special care was taken to select only the part of the cross correlation function that clearly shows a decay, avoiding the “noisy” data at the end of the cross-correlation function.

Fig. 5-9 shows a typical plot of the singular values of the Hankel matrix. Note that the singular values decrease monotonically, in contrast to other structures such as the building studied in chapter 3. Theoretically, the 11 vertical frequencies of the bridge will produce a jump close to the 22nd singular value which is not observed in this plot. By looking at the distribution of the singular values it is not possible to determine the number of frequencies to be identified. Thus, the cross spectral density function should be used to determine the number of natural frequencies to be identified in this type of structure. When the number of rows of the Hankel matrix is reduced to 120, the jump in the singular values is evident, but the frequencies and mode shapes identified by the technique are inaccurate. Accuracy in the identified modal parameters increases with a larger number of rows in the Hankel matrix. Thus, the number of rows should be selected by including as many points as possible of the decaying part of the cross correlation function (see Fig. 5-8).

The natural frequencies identified by the method are different depending on the reference channel selected to calculate the cross correlation functions. Furthermore, the accuracy of the identified mode shapes is also dependent on the reference channel. For example, Fig. 5-10 shows the identified mode shape of the undamaged structure for the 3rd vertical natural frequency using channels 3 and 10. These mode shapes correspond to the degrees of freedom of the identification model (between Bent I and Pier II) and are normalized so the higher amplitude is equal to one. Some differences between the two identified mode shapes are observed.

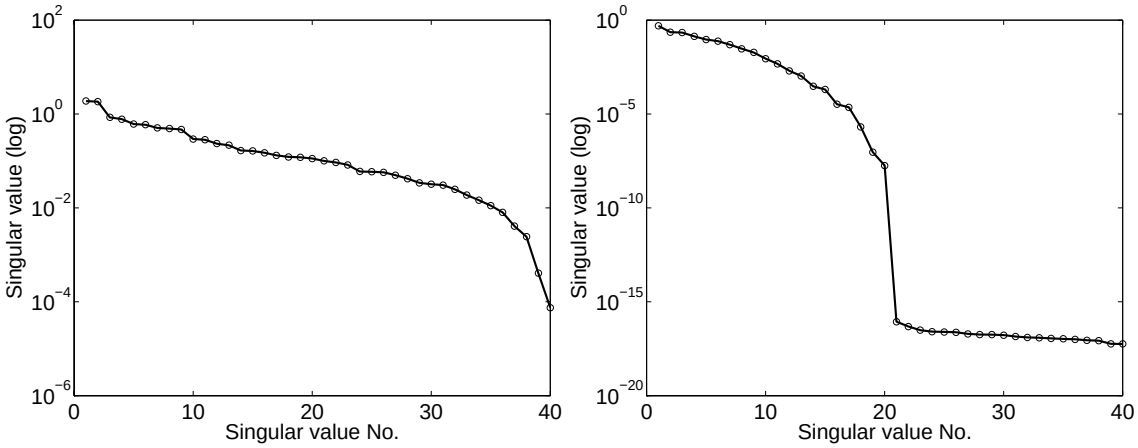

(a) 40 by 1200 Hankel matrix (b) 40 by 120 Hankel matrix

FIGURE 5-9. Singular Values of the Hankel Matrix

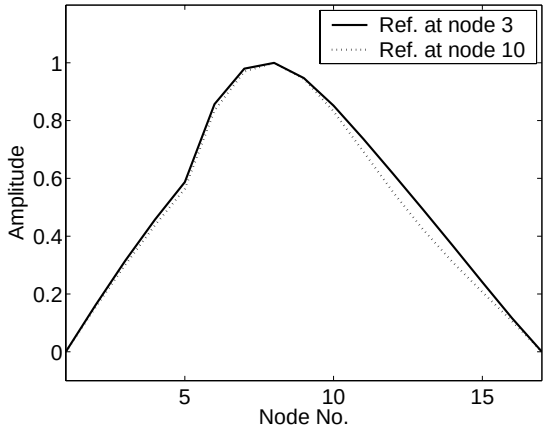

FIGURE 5-10. 3rd Vertical Mode Shape

Usually the ERA is applied by selecting a single reference channel. This reference channel should be selected at a point on the structure that is far from a node of vibration. In buildings the obvious solution would be a sensor located on the roof of the structure, but for this implementation the selection of the reference channel is not obvious. Only one column of the full cross correlation function matrix will be used for one reference channel, but the same method can be applied to all the columns of the cross correlation function matrix by selecting each channel as the reference. This approach will result in *n* sets of identified natural frequencies and mode shapes, where *n* is the number of reference channels. The identified modal parameters are selected as the average of these *n* sets.

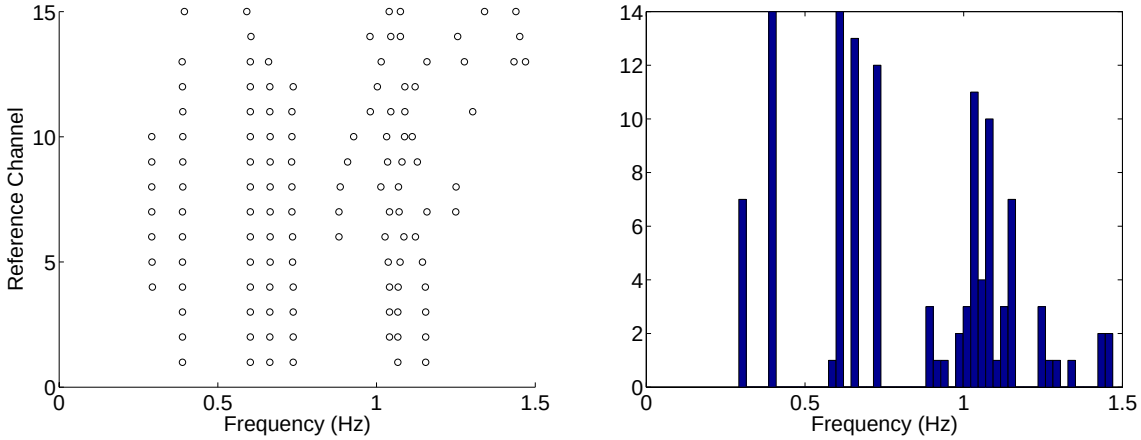

(a) Frequencies by reference channel (b) Histogram

FIGURE 5-11. Identified Natural Frequencies

Resulting *m* parameters corresponding to damping ratios higher than 4% and lower than 1% were not used in the analysis as they are not expected to be accurate modes.

Figure 5-11 shows the identified natural frequencies using every vertical acceleration as a reference channel. Correct natural frequencies appear at the same frequency for several reference channels while numerical errors appear as isolated frequencies in few reference channels. Seven of the 11 modes between 0 and 1.5 Hz for the undamaged structure were clearly identified by the method.

Figure 5-11b shows a histogram of the information shown in Fig. 5-11a. Here a spike is clearly shown for each identified natural frequency. Note that it is more difficult to detect closely spaced natural frequencies, such as the 7th, 8th and 9th modes, but the methodology is able to identify some of these modes. Table 5-2 shows the identified natural frequencies and the error obtained in the identification. The maximum error is

0.51% in the identification of the second mode. Even though not all modes were identified, the method is accurate.

TABLE 5-2. Identified Natural Frequencies

Freq. No.	Exact (Hz)	Identified (Hz)	Error (%)
1	0.2931	0.2922	0.3071
2	0.3912	0.3892	0.5112
3	0.6025	0.6024	0.0166
4	0.6643	0.6639	0.0602
5	0.7303	0.7353	0.6847
6	0.8789	-	-
7	1.0303	1.0326	0.2232
8	1.0712	1.0762	0.4668
9	1.0963	-	-
10	1.2651	-	-
11	1.4914	-	-

More natural frequencies can be identified by increasing the record length. This result is due to a better estimation of the cross correlation function because of a greater number of averages in the calculation of the cross spectral density function. Table 5-3 shows the identified natural frequencies with a two hour record. The last natural frequency was not identified because it is very close to the end of the frequency range being inspected (0 to 1.5 Hz). Although more modes can be obtained with a two hour record, the remaining part of this chapter uses 30 minute records.

As described previously, the identified mode shapes are slightly different for different reference channels. This variation can be used as a measure of the accuracy of the identified mode shape. Figure 5-12 shows the average, upper bound and lower bound of the 1st and 6th identified modes. The modes are each normalized such that the maximum value of the average is equal to one. The maximum difference between the upper bound and the lower bound for the 1st mode shape is 0.028, and for the 6th mode shape is 0.254 indicating that the 1st mode shape is more precisely identified. This error between the

TABLE 5-3. Identified Natural Frequencies for a Two Hour Record

Freq. No.	Exact (Hz)	Identified (Hz)	Error (%)
1	0.2931	0.2935	0.1517
2	0.3912	0.3922	0.2470
3	0.6025	0.6045	0.3390
4	0.6643	0.6650	0.1052
5	0.7303	0.7345	0.5735
6	0.8789	0.8810	0.2380
7	1.0303	1.0373	0.6793
8	1.0712	1.0834	1.1431
9	1.0963	1.0881	0.7523
10	1.2651	1.2671	0.1579
11	1.4914	-	-

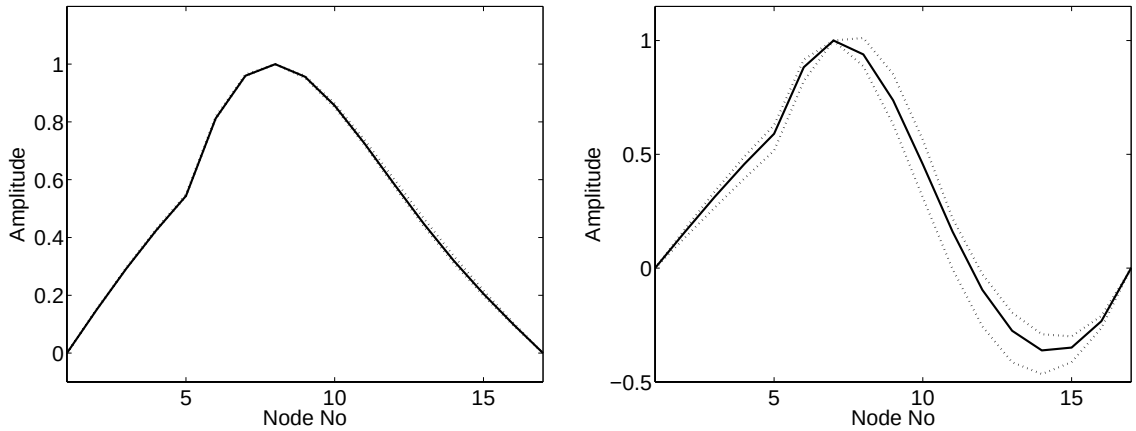

(a) 1st mode shape (b) 6th mode shape

FIGURE 5-12. Identified Mode Shapes

upper and lower bounds can be used as a measure to accept or reject an identified mode. It was found that closely spaced modes present higher errors in the estimation of the mode shapes than modes that are farther apart.

5.3 Damage Scenarios

A damage identification exercise is next performed using the identification model developed in section 5.1 and the modal parameters found in the previous section. Two damage scenarios are studied. The first damage corresponds to a 30% change in stiffness in element number 5, and the second is a 20% damage in element 20. The first case lies inside the sub-structure being monitored with the identification model, and the second case is outside this sub-structure. For the modal identification, 30 minutes of acceleration records resampled at 3Hz are used. These acceleration records correspond to the longitudinal, vertical and rotational accelerations of the deck nodes between Bent I and Pier II (62 channels). For the calculation of the cross spectral density function matrix a window of 512 points is used with 75% overlapping. The Hankel matrix used in the ERA has 40 columns and 1200 rows, utilizing 77 points of the cross spectral density function.

Table 5-4 shows the identified natural frequencies for each case. Different natural frequencies are identified for the different damage cases. The 6th, 9th, 10th and 11th are not identified for the healthy structure; the 4th, 6th, 10th, and 11th modal parameters are not identified for the first damage case; and for the second damage case the 1st, 8th, and 11th modal parameters are not identified. It is difficult to determine if the structure is damaged by the changes of the identified natural frequencies even though the damage in the structure is severe. This result agrees with the conclusions obtained in chapter 4.

Figure 5-13 shows the identified loss in stiffness using the fourth identification model discussed in section 5.1. Damage can be clearly identified and quantified by a loss in the stiffness in element number five for the first damage case. The second damage case did not affect the identified change in stiffness, indicating that the methodology can be applied to a portion of a structure.

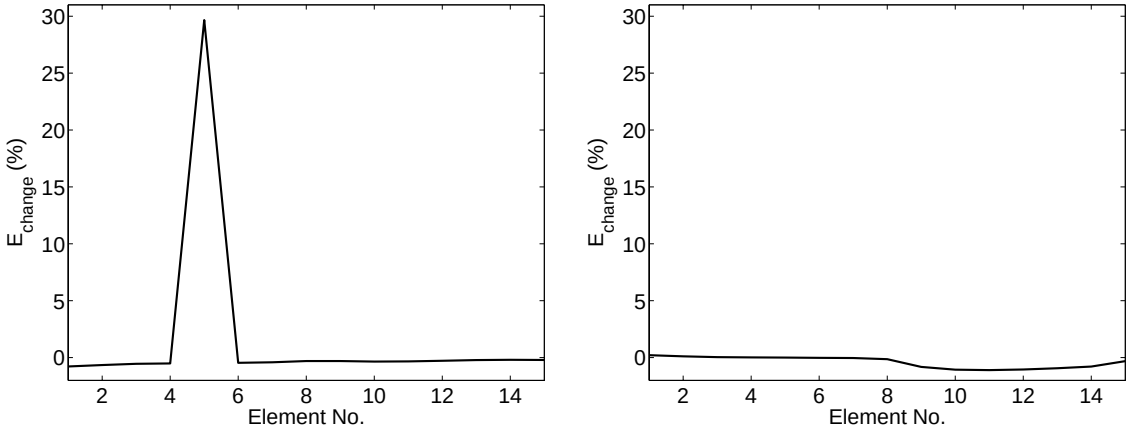

(a) 30% reduction in element 5 (b) 20% reduction in element 20

FIGURE 5-13. Stiffness Change

TABLE 5-4. Identified Natural Frequencies for Damage Scenarios

Freq. No.	Undamaged (Hz)	30% at element 5	20% at element 20
1	0.2922	0.2937	-
2	0.3892	0.3882	0.3936
3	0.6024	0.5967	0.6064
4	0.6639	-	0.6594
5	0.7353	0.7300	0.7242
6	-	-	0.8925
7	1.0326	1.0378	1.0255
8	1.0762	1.0737	-
9	-	1.0899	1.0969
10	-	-	1.2703
11	-	-	-

5.4 Summary

In this chapter a numerical implementation of the SHM methodology was discussed. The method was implemented on the numerical model of the Bill Emerson Memorial Bridge. Four different identification models were tested to identify what measurements are important for the structural parameter identification procedure. For the identification of damage in the bridge deck the dynamics of the tower have little effect, and no measures in

the towers are needed. It was also shown that the deck can be divided into sub-structures to reduce the number of sensors required. Longitudinal and vertical accelerations as well as rotational accelerations with respect to the transverse axis of the elements being monitored were found to have a strong impact in the identification procedure. This result conflicts with the results obtained in chapter 3, where rotations at the floors with respect to the *X* and *Y* axes were not important.

Here NExT and ERA correctly identified natural frequencies and mode shapes of the structure using 30 minute records with a sampling frequency of 3Hz. Long records are needed in this type of structure because of their low frequency behavior, although a high sampling rate is not necessary. Seven of the 11 available natural frequencies in the frequency range studied were identified for the undamaged structure. Even though not all the available natural frequencies were identified, the identification of damage was accurate. The identified mode shapes using two different reference channels are slightly different. A set of natural frequencies and mode shapes for a particular mode can be obtained by applying the methodology using different reference channels. A lower bound and upper bound for the estimated mode shapes can be obtained from this set, indicating the accuracy of the identification. It was found that the accuracy and the amount of identified parameters improves by using longer records due to better estimation of the cross spectral density function matrix.

Two damage scenarios were studied using the complete SHM methodology. The identification model focused on the elements between Bent 1 and Pier IV. In the first damage case, an element in the section being monitored was damaged by 30% and in the second case an element outside this section was damaged by 20%. The damage was successfully identified in the first damage scenario. In the second case no change in the Young's modulus was observed in the elements being monitored, showing the ability of the methodology to be applied to a portion of a structure.

Chapter 6

Experimental Implementation

An model was designed and built to experimentally verify the structural health monitoring methodology described in this dissertation. In the first part of this chapter, a description of the laboratory model is provided. Next, an identification model of the structure is discussed. This identification model focuses on the last six elements of the bridge (elements 25 through 30) and has a total of 12 active degrees of freedom. Hammer testing is used to determine the transfer function matrix between the force applied by the hammer and the acceleration records of the active DOF of the identification model. Then, the ERA is used to identify the natural frequencies and mode shapes of the structure based on the recorded data. A case scenario is presented where element 29 of the bridge is damaged. The parameter identification technique is used to identify the damaged element.

6.1 Cable-Stayed Bridge Model

An experimental model used to reproduce the complex behavior of cable-stayed structures was designed. The stainless steel experimental model shown in Fig. 6-1 has a total length of 2m (78 in) and a width of 19cm (7.5 in). The model was designed such that additional experiments could be performed by changing the mass, the stiffness of the deck members, the number of towers or the type of boundary conditions. The structure is supported by a single tower and two end supports (bents). Sixty cables are used to support the deck,

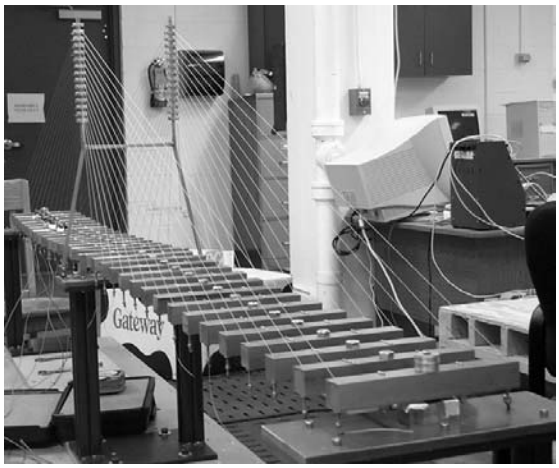

FIGURE 6-1. Laboratory Model

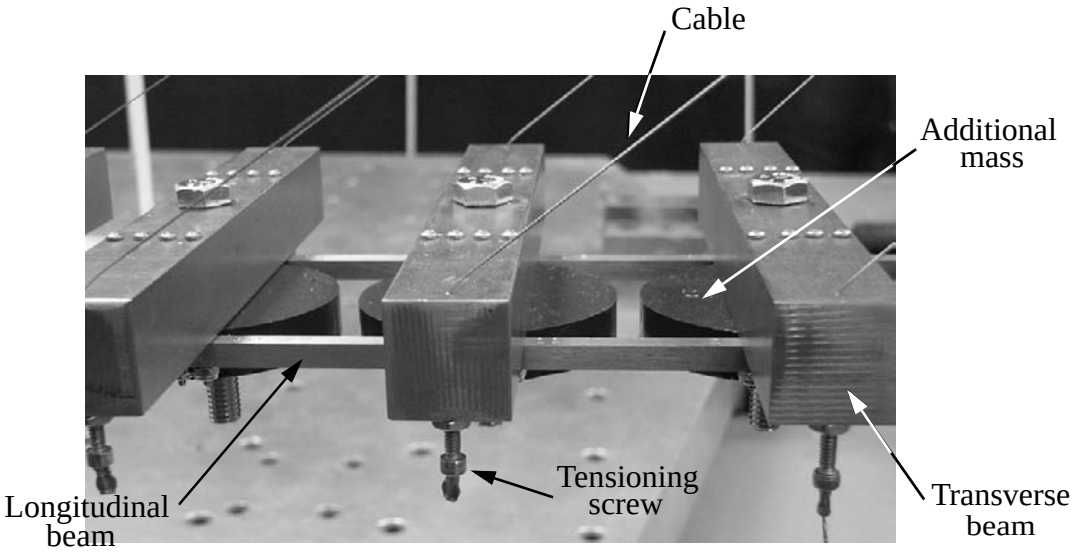

FIGURE 6-2. Laboratory Model - Deck

which is composed of thirty $2.54 \times 2.54 \times 19\,\text{cm}$ ($1 \times 1 \times 7.5$ in) transverse deck members, sixty $0.63 \times 0.63 \times 7.62\,\text{cm}$ ($0.25 \times 0.25 \times 3$ in) longitudinal members and twenty eight lead masses. The cables connect the tower and the transverse members. Two longitudinal members are used to connect each transverse member using two screws at each end. Additionally a 0.57kg (1.25 lb) mass is added to each section of the deck by a lead disk of 7cm (2.75in) radius and 1.27cm (0.5in) thick. To tension the cables a hollow

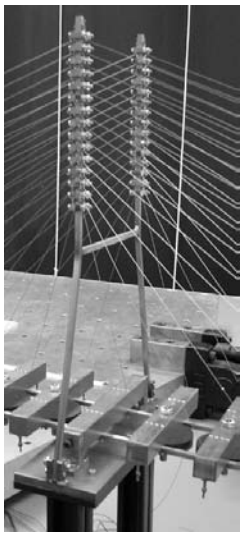

(a) Tower

(b) Cables Connections

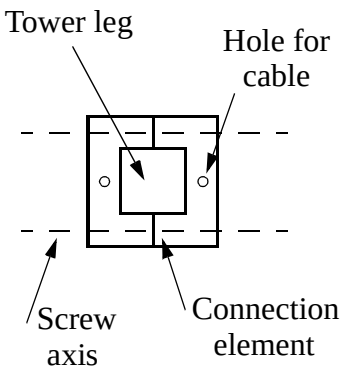

(c) Connection Detail

FIGURE 6-3. Laboratory Model - Tower

screw in the transverse deck members was used on each side as shown in Fig. 6-2. The cables are tensioned by loosening the screw and untensioned by tightening the screw. A lock nut was used to secure the screw once the cable was set to the desired tension.

The H-shaped tower was constructed using two 0.63×0.63 cm (0.25×0.25 in) square bars. The tower is 50cm (19.5 in) tall, the bottom is 29cm (11.37in) wide and the top section is 18.41cm (7.25in). The cables are connected at 1.27cm (0.5 in) increments, starting at 2.54cm (1in) from the top of the tower. Each cable is connected independently to each side of the tower as shown in Fig. 6-3. To connect the cables to the tower a small U-shaped element was built. Two of these elements are connected from each side of the tower using two screws, and the cable is connected to the tower using the hole in each side of the tower as shown in Fig. 6-3c.

The connection between the deck and the tower allows rotations with respect to the transverse axis of the bridge but restrains any other type of movement. At the other supports the deck is free to rotate with respect to the vertical axis and displace in the longitudinal direction. This boundary condition was achieved using a slotted bolt in the

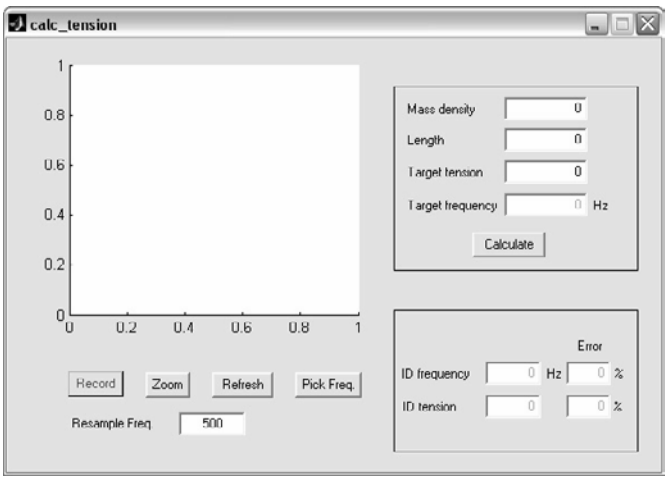

FIGURE 6-4. GUI to Measure the Tension in the Cables

middle of the end transverse elements of the deck. These boundary conditions are the same as the boundary conditions for the Bill Emerson Memorial Bridge discussed in Chapters 4 and 5. The boundary conditions of the bridge can be easily changed for future studies. Detailed plans used for the fabrication of the bridge can be found in Appendix A.

Before the bridge was tested the cables were tensioned to a predetermined value. The natural frequency of each cable was used to determine the tension in each cable. A microphone was connected to a computer and the sound produced by the cable was recorded. A spectral density function of the recorded sound is calculated and the cable is tensioned until the peak corresponding to the first natural frequency matches the target frequency calculated by

$$f = \frac{1}{2L}\sqrt{\frac{T}{\gamma}}, \tag{6-1}$$

where f is the first natural frequency of the cable, L is the length of the cable, T is the tension on the cable and γ is the mass density per unit length. A Matlab program was used to record and analyze the data (see Fig. 6-4). Note that the frequency of a cable including

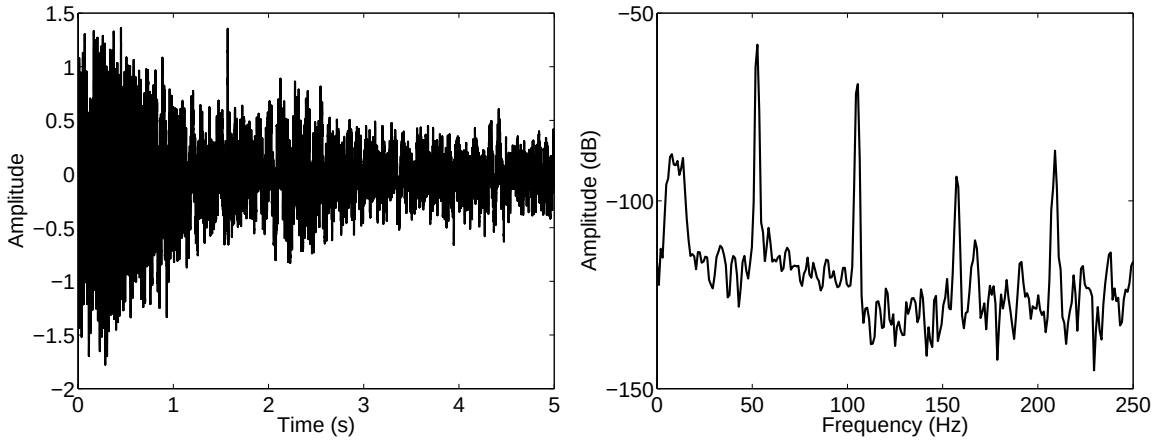

(a) Sound Record **(b) Power Spectral Density**

FIGURE 6-5. Representative Sound Record and Power Spectral Density Function

the catenary shape is not used here due to the light mass of the cables. The sound was recorded using the sound card of the computer with a sample frequency of 11025Hz and resampled to a lower frequency using Matlab. Then, the power spectral density was calculated and the natural frequency was selected from the peaks of the power spectral density. By inserting the information for each cable in the GUI shown in Fig. 6-4, the tension in the cable was calculated using Eq. 6-1. Figure 6-5 shows a plot of a typical sound record and its power spectral density. In this figure the first natural frequency is clearly close to 50 Hz. The second, third and fourth natural frequencies of the cable are also observed near 100, 150 and 200 Hz, respectively.

The length, tension and target natural frequency of each cable are shown in Table 6-1. The process of tensioning the cables is iterative because of the interaction of the tension of the different cables. After tensioning each cable, an additional set of data was obtained to assure that all the cables were correctly tensioned. The tension in each cable is shown in Table 6-2, where the cables are numbered as shown in Fig. 6-6.

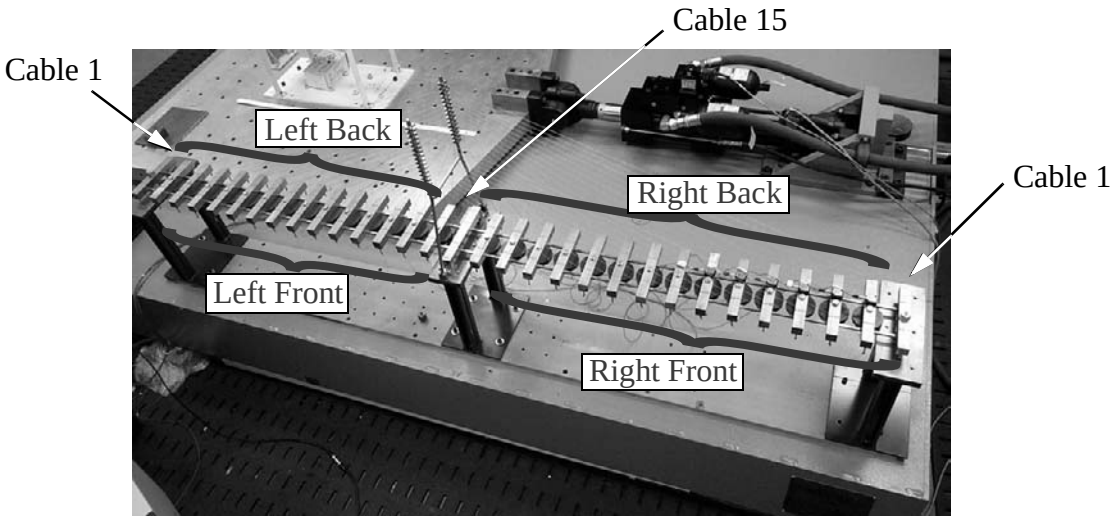

FIGURE 6-6. Cable Numbering

TABLE 6-1. Cable Frequency and Target Tensions

Cable No.	Length (m)	Target Frequency (Hz)	Target Tension (N)
1	1.22	52	22
2	1.15	54	21
3	1.07	57	20
4	1.00	58	18
5	0.93	61	18
6	0.85	64	16
7	0.78	68	15
8	0.71	72	14
9	0.64	76	13
10	0.57	84	12
11	0.50	94	12
12	0.43	101	10
13	0.37	112	9
14	0.32	123	8
15	0.28	135	7

TABLE 6-2. Final Tension of the Cables

Cable No.	First Natural Frequency (Hz)			
	Left Front	Left Back	Right Front	Right Back
1	51.9	53.7	51.9	51.2
2	54.6	55.0	53.0	53.8
3	57.6	57.6	56.0	57.0
4	58.3	58.8	58.8	58.1
5	61.7	61.5	62.0	61.7
6	64.0	63.9	64.6	64.6
7	67.8	68.5	67.9	69.1
8	71.7	72.3	72.3	73.0
9	76.4	75.6	78.0	77.4
10	83.1	82.4	85.7	85.7
11	96.5	96.6	94.0	92.1
12	97.8	106.2	101.7	101.8
13	112.3	109.4	111.9	115.7
14	118.9	125.4	129.8	120.9
15	134.4	136.9	134.4	137.5

6.2 Implementation

6.2.1 Identification Model

An identification model for the laboratory structure was developed to validate experimentally the proposed SHM technique. Here, the deck is modeled as a spine beam composed of 30 beam elements as shown in Fig. 6-7. Thirty five beam elements are used to model the tower, 60 cable elements are used for the cables, and 60 rigid links are used to connect the cables to the deck beam. Because of a limited number of sensors is available, the substructure approach is adopted. The focus is on the identification of damage in the last five elements of the deck (elements 25 to 30) shown by the thick line in Fig. 6-7. This is similar to the numerical implementation performed for the Emerson Bridge in Chapter 5. Thus, the only available degrees of freedom are the rotations with respect to the transverse axis and the vertical displacements of nodes 25 to 30 for a total of

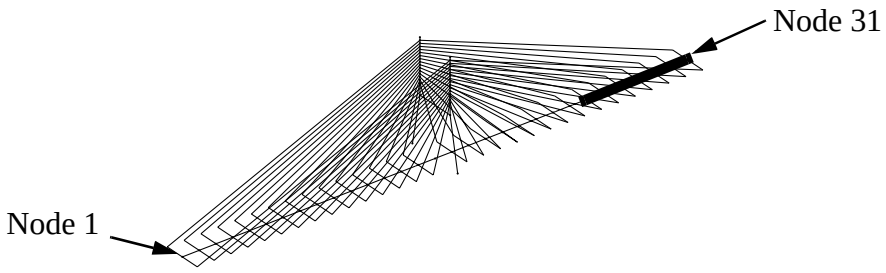

FIGURE 6-7. Identification Model

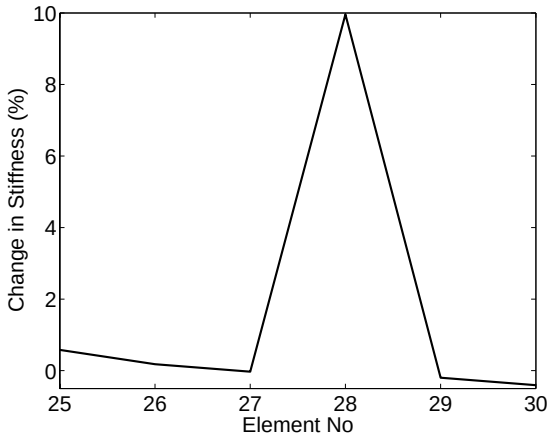

FIGURE 6-8. Numerical Evaluation of ID Model

12 active DOF. Node 31 is constrained because it is connected to the support in the real structure.

The identification model was evaluated using a numerical example prior to use in the experiment. This evaluation was performed using the same procedure described in the previous chapter. The identification model, without constraints (379 DOF), was used for the calculation of the modal parameters. Figure 6-8 shows the final results of the SHM technique for a 10% loss in element 28. As shown in the graph, small errors were introduced by the difference in active degrees of freedom between the identification model (12 DOF) and the model used for determining the modal parameters (379 DOF). In this evaluation the first 10 natural frequencies and mode shapes were used.

6.2.2 Experimental Setup

An impact hammer was used to test the model due to low level of ambient vibrations available in the laboratory. The model was fixed to a 52 metric ton (115000 lb) concrete base of the earthquake simulator which filters most of the excitation from the surrounding environment. A PCB 086C03 modally tuned impact hammer with the 084B05 impact cap was used for the impact force. The hammer used has a sensitivity of 2.17 mV/N (9.66 mV/ lb) without the steel extender. Six PCB 370A02 accelerometers were secured to the deck at the transverse beams corresponding to the active degrees of freedom in the identification model (nodes 25 to 30). The accelerometers have a resolution of 0.00032 g and a range of 20 g. Their individual specifications are found in Table 6-3. Three Siglab 20-42 data acquisition boxes were used to collect the data from the hammer and the six accelerometers.

TABLE 6-3. Accelerometers Specifications

PCB Accelerometer Model: 370A02						
Serial No.	631	852	641	651	656	839
Voltage Sensitivity (mV/g)	102.1	101.6	101.2	98.5	103.3	101.4
Transverse Sensitivity (%)	0.6	0.3	0.4	0.3	0.6	0.7
Resonant Frequency (Hz)	1160	1220	1180	1220	1220	1180
Zero g Offset Voltage (mV DC)	3	-11	-15	36	4	11

The transfer functions between the force applied by the hammer and the acceleration at the different points were calculated using the virtual network analyzer (VNA) tool available in the Siglab data acquisition system. A bandwidth of 100Hz was chosen for the experiments, allowing us to determine the natural frequencies of the model below 50 Hz. Fifteen hits were performed in each test with a record length of 512 points and 50% overlapping between windows. The average transfer function for each hit was computed and used for the analysis. Antialiasing filters were used to avoid aliasing of higher frequencies to the range of interest. The window F20_Exp.01 available in Siglab was used. This window records only the first 20% in the hammer channel to avoid recording

noise (e.g. the person resting the hammer on a table) and the remaining portion is padded with zeros. This also applies an exponential window to the acceleration data to avoid leakage in the calculation of transfer functions. The damping associated with this window is one percent of critical.

Different gains were used for the different types of sensors. Table 6-4 shows the gains selected for each channel in the data acquisition system and the gain for each sensor in the power amplifier. Before every test the DC value of the accelerometers was set to zero using the variable gain in the power amplifier.

TABLE 6-4. Channel Setup

Channel No.	1	2	3	4	5	6	7
Sensor Serial No.	Hammer	631	852	641	651	656	839
Location (Beam No.)		25	26	27	28	29	30
Power Amplifier gain	10	100	100	100	100	100	100
Range in Data Acquisition System (V)	±1.3	±10	±10	±10	±10	±10	±10

The hammer was used to hit the structure at the head of the screw holding the lead masses as shown in Fig. 6-9a. This location was selected to avoid excitation of any torsional modes. All active degrees of freedom in the identification model were selected as impact locations. This facilitates determination of the full transfer function matrix between vertical forces and vertical accelerations in the area of interest because a sensor was also placed at each location.

The rotation at each degree of freedom is an important factor in the identification process as discussed in Chapter 5. No rotational accelerometers were available to measure these rotations; thus the transfer functions between a moment applied to the structure and the resulting vertical accelerations were used. For this, the screws used to hold the additional lead masses were extended, and the hammer was used to apply a force at the end of the

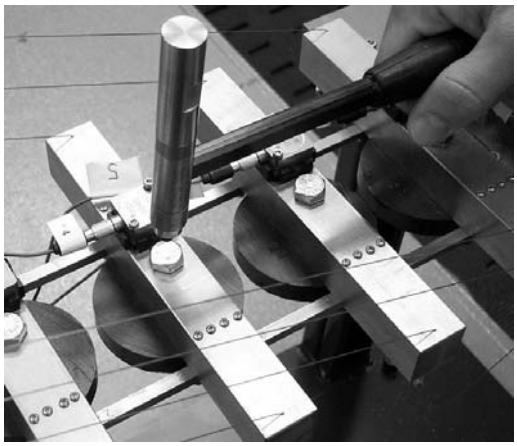

(a) Impulse Force

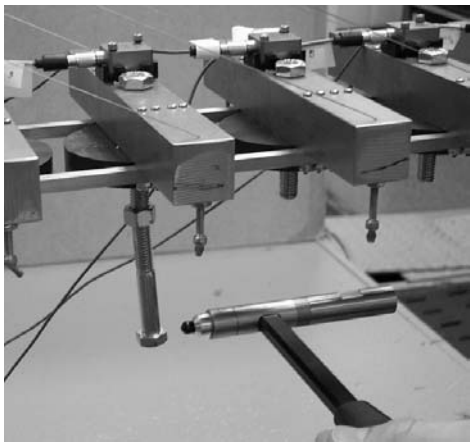

(b) Impulse Moment

FIGURE 6-9. Hammer Tests

screw in the longitudinal direction (See Fig. 6-9b). This applies a moment to the deck and a force in the longitudinal direction. The applied moment is equal to the force applied by the hammer times the length of the screw, measured as 10cm (4in). Because the accelerometers measure the vertical acceleration, only the response due to the applied moment will be captured. Also, the longitudinal modes are expected to have much higher frequency than the vertical modes, lying outside the frequency range of interest. When the moment is applied to the structure, vertical movement at the deck is observed. This procedure is then repeated at each node where rotations are required (Nodes 25 to 30).

6.2.3 Results

Figure 6-10a shows a typical transfer function obtained from the experiment. Note that a high DC value is obtained due to the type of accelerometers used (DC accelerometers). In reality the DC value should be zero because a static load will produce no acceleration. The high DC values may produce some errors in the identification process using the ERA because this approach yields a pole at or near zero. To avoid this problem, the magnitude of the recorded transfer functions was adjusted below 5 Hz. This change does not affect the modal information obtained using the ERA because the resonant frequencies of the

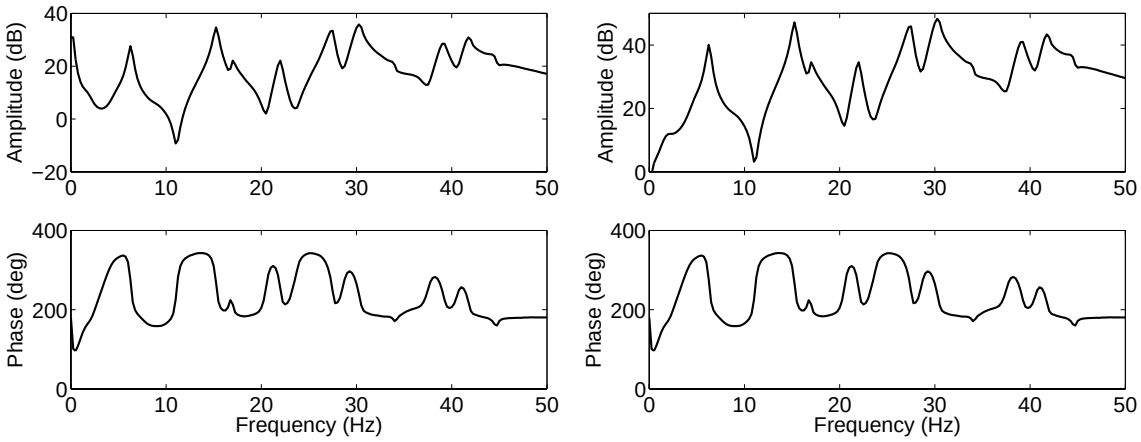

(a) Raw Data **(b) Data to Process with ERA**

FIGURE 6-10. Representative Experimental Transfer Function

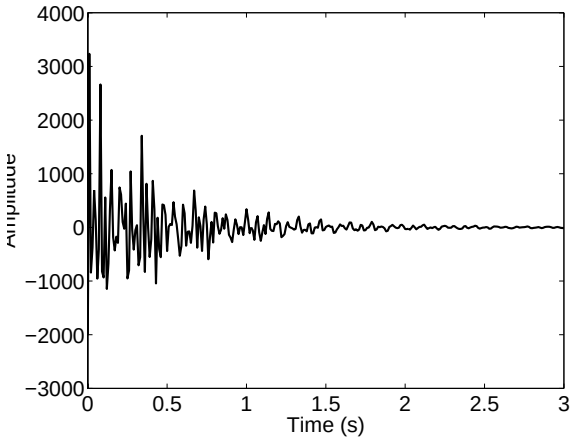

FIGURE 6-11. Impulse Response Function

structure are higher than 5Hz. Figure 6-10b shows the new transfer function. The sensitivity of the accelerometers and the gain factors of the power supply has been taken into account in this new transfer function.

The ERA can be used with free responses or with impulse response functions as discussed in Chapter 2. Here, impulse response functions calculated as the inverse Fourier transform of the transfer functions were used. Figure 6-11 shows a typical impulse response function. A Hankel matrix with 40 columns and 1200 rows was used in the identification.

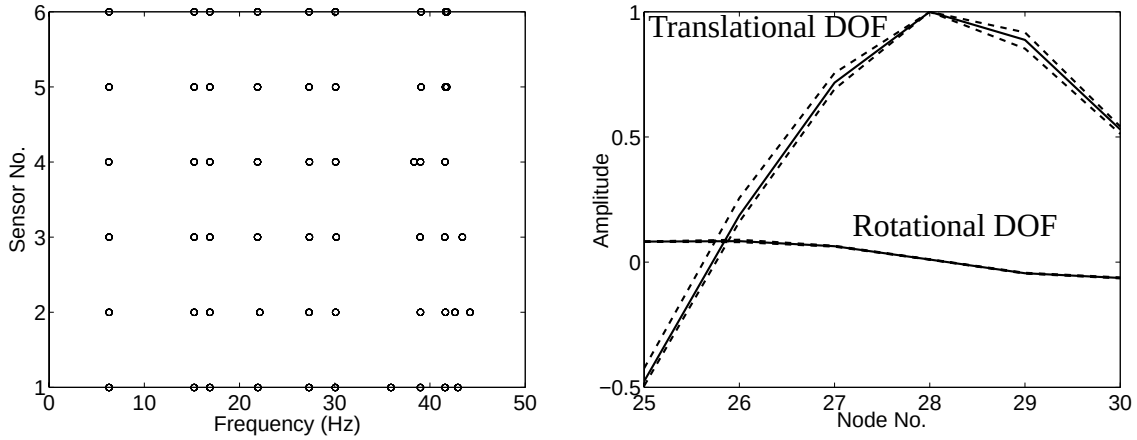

(a) Natural Frequency per Sensor (b) Fourth Identified Mode Shape

FIGURE 6-12. Identified Natural Frequencies and Mode Shapes

Six sets of natural frequencies and mode shapes were calculated with the ERA (one for each sensor), similar to the procedure followed in the previous chapter. Figure 6-12a shows the identified natural frequencies for each run. The natural frequencies of the structure can be clearly identified from this plot. Figure 6-12b shows the variation average, as well as the upper and lower bounds of the identified fourth mode shape. A small variation is observed between the upper and lower bounds. The average of the six measurements is used for the identification of the elemental properties of the structure.

Four different tests were performed. Two tests were conducted with the healthy structure, and two with a damaged structure. Damage was induced in the structure by replacing the longitudinal members at section 29 with a new “damaged” element. The height of the cross sectional area of the new members was reduced by 0.13cm (0.05 in). This change corresponds to a reduction of 50% in the moment of inertia of the element with respect to the transverse axis. The identified natural frequencies for the healthy and damaged structures are shown in Table 6-5. The eight natural frequencies from tests 2 and 4 were discarded due to the high variation between the upper and lower bounds of the identified mode shapes.

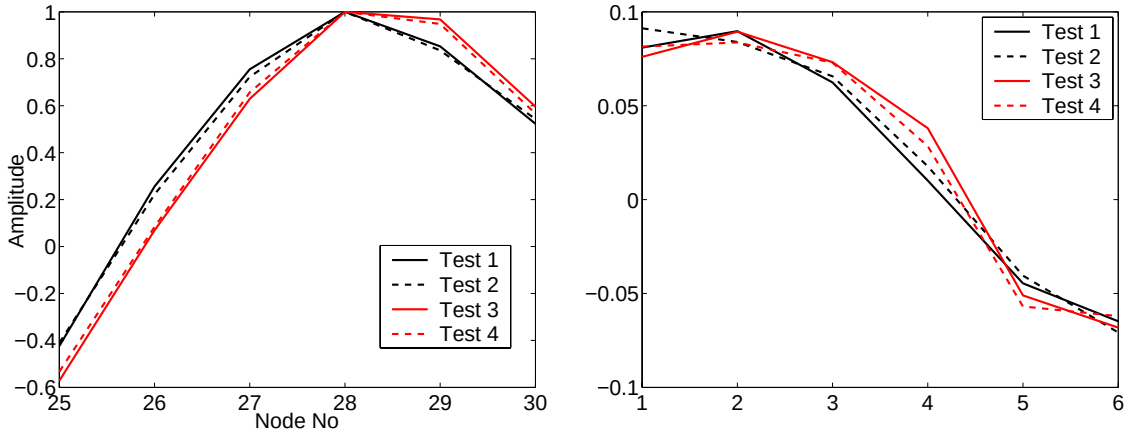

(a) Translational DOF (b) Rotational DOF

FIGURE 6-13. Identified 4th Mode Shapes

A change in the natural frequency is observed in the natural frequencies. The healthy structure has higher natural frequencies than the damaged structure as expected. The maximum variation was calculated to be 1.75% and occurred between the 6th natural frequencies in tests 1 and 3.

Figure 6-13 shows the 4th mode shape for each test. This graph shows good agreement between tests 1 and 2, and tests 3 and 4 for the translational DOF. In the rotational degrees

TABLE 6-5. Identified Natural Frequencies

Freq. No.	Healthy Structure		Damaged Structure	
	Test 1	Test 2	Test 3	Test 4
1	6.29	6.29	6.24	6.24
2	15.23	15.22	15.16	15.16
3	16.90	16.90	16.67	16.72
4	21.90	21.91	21.56	21.57
5	27.32	27.33	26.92	27.03
6	30.10	30.10	29.57	29.58
7	39.01	39.00	38.61	38.87
8	41.61	-	41.24	-

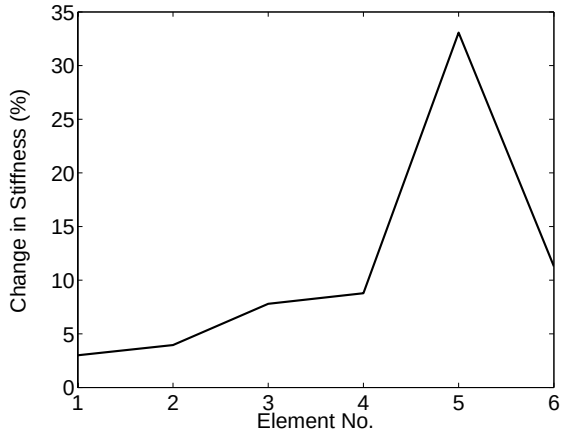

FIGURE 6-14. Change in the Stiffness

of freedom, this agreement is not as good as in the translational DOF. These results could be improved by obtaining a better measure of the rotational DOF, perhaps by using rotational accelerometers. A maximum variation of 18.7% is observed for the translational DOF of this mode shape. The variation in the mode shape is larger than the variation in the natural frequencies, in agreement with the results found in previous chapters.

Using the identified parameters, the change in the stiffness was calculated as shown in Fig. 6-14. In this plot it is clear that the maximum variation in stiffness occurs in element 29. Small changes in the stiffness are obtained in the other elements, most likely due to errors introduced in the measurements of the rotational degrees of freedom and modeling errors. Although the location of damage was clearly identified, the change in stiffness in the damaged member was expected to be 50%, but only 33% was identified.

6.3 Summary

In this chapter the experimental implementation of the SHM technique proposed in this dissertation is discussed. The implementation is performed using a laboratory model constructed to reproduce the complex behaviors of cable-stayed bridges. A description of

the structure is provided, and detailed plans used for the fabrication of the model are included in Appendix A.

An identification model to detect damage in the experimental structure was developed. This model focused on the 6 beams of the bridge close to one end, and has a total of 12 active degrees of freedom. A numerical study to verify the identification model was performed, similar to the numerical implementation discussed in the previous chapter. The conclusions of this numerical evaluation demonstrated that the identification model was appropriated to detect damage in these 6 elements.

Hammer testing was performed using the experimental model to determine the natural frequencies and mode shapes of the structure in both healthy and damaged configurations. The transfer functions between the forces applied by the hammer and six accelerometers was obtained. To calculate the rotational degrees of freedom, an impact moment was applied to the structure. This impact moment was achieved by applying an impact force to a relatively rigid extension below the section of the deck. The impact was applied along in the longitudinal axis of the bridge, resulting in a moment with respect to the transverse axis and a force in the longitudinal direction of the bridge.

The damage scenario was conducted by replacing the members corresponding to bay 29 of the bridge with smaller members. The ERA was applied to the frequency response functions obtained from the tests to determine the experimental natural frequencies and mode shapes of the structure. The identified natural frequencies only changed by 1.75% with the induced damaged while the 4th mode shape changed as much as 18.7% in the vertical DOF. This results indicates that the mode shapes are more sensitive to damage, agreeing with the results obtained in previous chapters.

The identification model was implemented to calculate the stiffness change between the damaged and undamaged stages. The methodology was successful in identifying the

location of damage, but the amount of damage was underestimated. These results are expected to improve with the addition of sensors to measure the rotational degrees of freedom.

Chapter 7

Conclusions and Future Work

This dissertation proposes and validates a structural health monitoring technique that can be applied to large flexible civil structures such as cable-stayed bridges. The methodology uses available techniques for modal identification such as the natural excitation technique (NExT) and the eigensystem realization algorithm (ERA). The identified modal parameters are used in a least squares solution of the eigenvalue problem for parameter identification. The proposed approach uses the geometry of the structure to identify parameters of structural members, such as Young's modulus, based on natural frequencies and mode shapes. The least squares solution of the eigenvalue problem is applied using a procedure similar to the finite element method. First, elemental matrices are created and transformed from local to general coordinates. Then, the complete identification model is assembled. Constraints and boundary conditions are then applied to the identification model.

The advantages of the proposed methodology include the following:

- It can be applied using ambient excitation, allowing the monitoring of structures during operation.
- It can be applied to portions of the structure or sub-structures, reducing the number of sensors needed.
- It does not require sorting and/or matching natural frequencies and mode shapes from different tests.

- The modal identification part of the method can be applied to closely space modes.
- The least squares part of the eigenvalue problem is applied using a procedure similar to the finite element method, increasing the speed of its implementation.

The disadvantages of the methodology include:

- It requires long records (greater than 30 minutes) for the identification of modal parameters of flexible structures due to the low frequency behavior of these structures.
- When identifying structures such as cable-stayed bridges the rotational components of the mode shapes are needed to successfully locate damage in the structure, requiring additional sensors.
- An estimate of the mass of the structure is needed for the determination of the structural parameters.

The methodology was applied to three structures. The first structure is the IASC-ASCE benchmark test structure. Three different cases, two numerical and one experimental were studied. The methodology was also applied to a numerical model of the Bill Emerson Memorial Bridge and to a laboratory test structure built to reproduce the challenges encountered in cable-stayed bridges.

The ERA was originally developed to use impulse response functions, although it can also be used with free response data. Using free response data the ERA cannot obtain the **B** and **D** matrices of the state-space representation, but it can accurately identify the **A** and **C** matrices. These last two are sufficient to determine the modal parameters of a structure.

The proposed methodology was applied to the first two numerical phases and the first experimental phase of the IASC-ASC Benchmark Problem. In the second numerical phase it was found that analyzing the results of several identification models produces more

precise information than only using a single identification model. The blind cases studied are a clear example of this. Here a 8 DOF identification model was used to detect the floor where damage occurs, and a 12 DOF identification model was subsequently used to identify the damaged side of the structure. The use of ambient vibration for SHM was validated during the experimental phase of this study. Here, the modal parameters obtained with ambient vibration were in good agreement with the natural frequencies and mode shapes obtained by hammer tests.

A model of the Bill Emerson Memorial Bridge was developed and employed to validate the proposed SHM technique and study the sensitivity of various parameters to damage in the deck. First, the model of the deck was found to be very important in modeling of cable-stayed bridges. Two different deck models were considered. The first model used a spine beam with nodal masses, and the second model used lumped masses connected with rigid links to better reproduce the behavior of the C-shaped section of the deck. A comparison between the natural frequencies of these two models demonstrated that the C-shaped section model increases the coupling between rotational and transverse modes of vibration, while vertical modes remain almost unchanged.

The sensitivity of the static displacement, natural frequencies and mode shapes to damage in the deck of the Emerson Bridge was also studied. The study concluded that the natural frequencies and the static displacement are considerably less sensitive to damage than the mode shapes. Thus, the detection of the mode shapes is of vital importance in the development and implementation of SHM for this type of structures. Similar results were obtained in the implementation of the methodology to the laboratory test structure.

The numerical model of the Emerson Bridge was also used to study the implementation of the proposed methodology for cable-stayed bridges. Here NExT and ERA were successfully implemented for the identification of closely space modes. Various identification models of decreasing complexity were studied, yielding an important result

that measuring the rotational accelerations with respect to the transverse axis and the longitudinal accelerations of the bridge's deck are essential for damage identification. Considerable modeling errors were found in the methodology when these measurements are not included in the identification model. It also was found that the methodology can be applied to substructures. This allows for the implementation of the methodology to critical sections of the bridge, reducing the number of sensors needed. The methodology was successful in detecting and locating damage in the numerical model using a few modes of vibration. These modes do not need to be the same between the different tests. This is of importance in structures with closely spaced modes because modes can change places (e.g. the 9th mode become the 8th mode) due to damage.

In the last chapter of this dissertation the proposed SHM methodology was implemented on a laboratory structure. The structure was designed and built for studies in SHM and structural control. A complete description of the structure is provided in Appendix A. Hammer testing was used for the modal identification of the structure. The experimental transfer functions between the force produced by the hammer and six accelerometers was determined. The impulse response functions were calculated as the inverse Fourier transform of the transfer functions. Next, the ERA was used to identify the modal parameters of the structure using the impulse response functions. The modal parameters of a healthy and damaged structure were compared. The mode shapes were found to be more sensitive to damage than the natural frequencies, agreeing with the results obtained in the sensitivity study. An identification model focusing on a subsection of the deck was developed and used to successfully identify damage in a case scenario. Here the methodology was successful in identifying the location of damage, but the extent of damage was underestimated.

7.1 Future Work

NExT has been developed for broadband, stationary excitations. Although several researchers have successfully applied the methodology to the case of non-stationary excitations, further studies are needed for a better understanding of this technique under different types of excitations. The frequency range of the ambient vibration in large bridges should also be studied to determine the most likely modal parameters to be detected. The identification of higher modes will reduce the record length needed for the implementation of the proposed methodology.

In this dissertation a study of the sensitivity of different parameters to damage was performed. A study of the sensitivity of these parameters to changes in the environment such as temperature and humidity seems appropriate for the implementation of the methodology in a real structure. The results of this study may be included in the proposed methodology to adjust the modal parameters of the structure before the identification of structural parameters.

Additionally, it would be appropriate to associate a probabilistic measure with the damage identified in the structure. Although in the implementation of the technique some averaging is performed in the calculation of the cross spectral density functions and in the least squares solution of the eigenvalue problem, a probabilistic framework seems justified. An index of the confidence of the results should be developed to have a measure of the accuracy of the results obtained.

A large number of sensors is typically needed for the implementation of SHM techniques on flexible civil structures such as cable-stayed bridges. Thus, determination of the optimal location of these sensors should be addressed to reduce the cost and computational efforts associated with implementation.

Furthermore, constant monitoring of these structures will produce a vast amount of information. Thus, there is a need for research in appropriate methods to manage this information. These studies should consider different levels of information for different users. While in an emergency we might only be concerned with life safety issues, annual bridge inspections might be more interested in near-term repairs that may extend the life of the structure. Information related to damage identification might be included with other types of information, such as traffic, to provide owners with the overall performance of the structure.

Appendix A

Model Drawings

Drawings of the experimental model used in Chapter 6 are provided here.

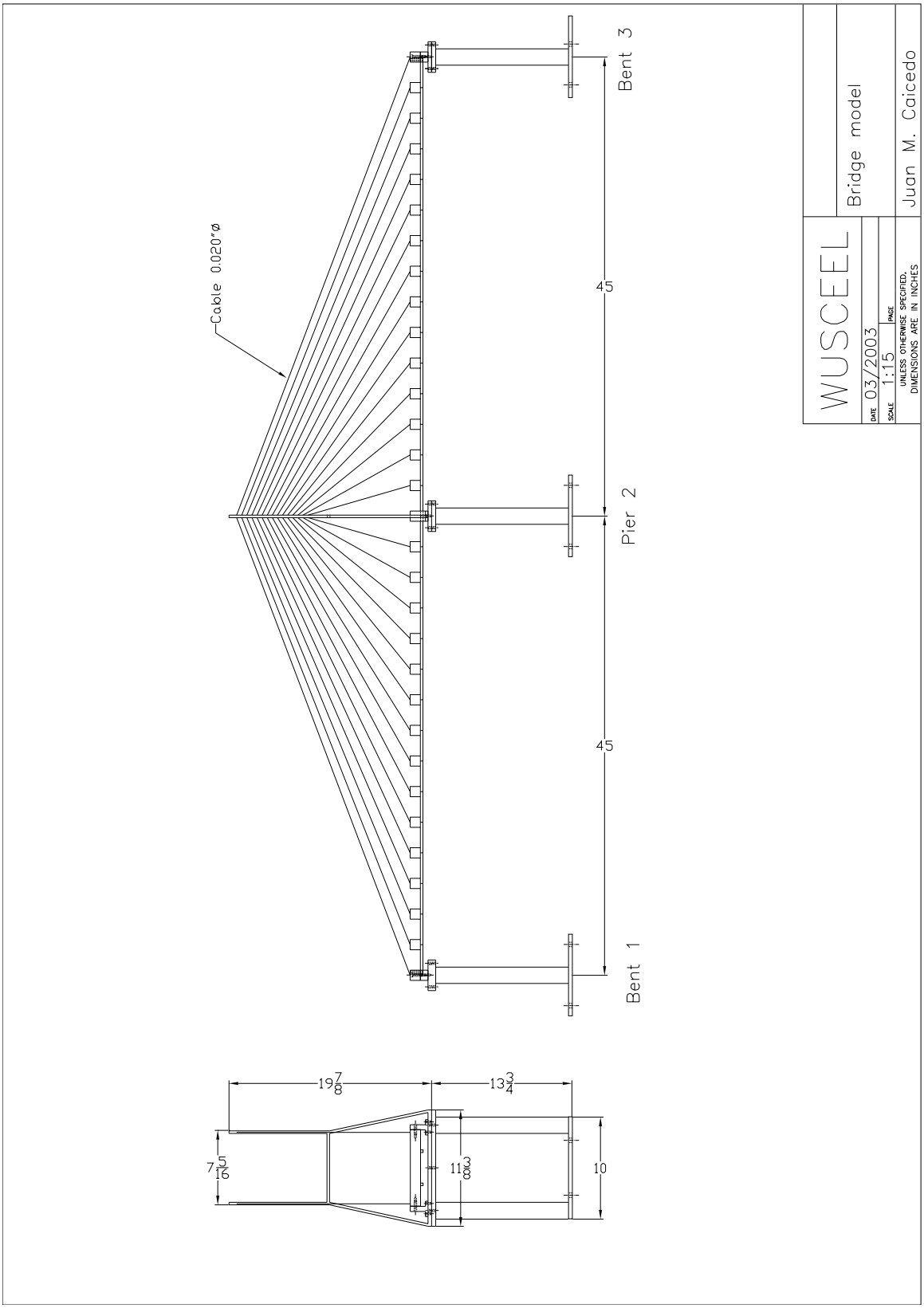
Cable 0.020"ø
Bent 3
Pier 2
Bent 1
45
45
19 7/8
13 3/4
7 5/16
11 3/8
10
WUSCEEL
Bridge model
DATE 03/2003
SCALE 1:15
PAGE
UNLESS OTHERWISE SPECIFIED,
DIMENSIONS ARE IN INCHES
Juan M. Caicedo

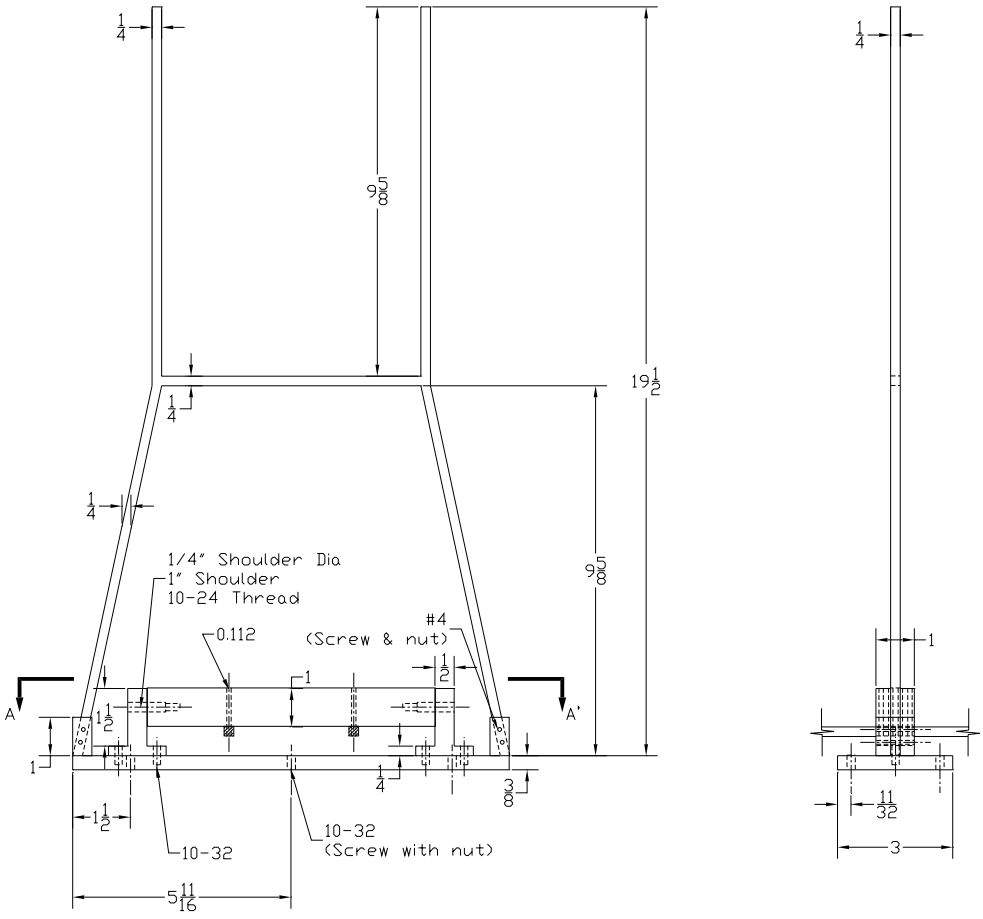

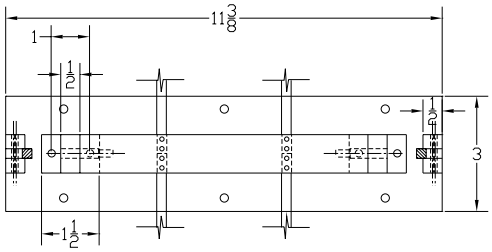

WUSCEEL	
DATE 03/2003	Tower
SCALE 1:5 PAGE	
UNLESS OTHERWISE SPECIFIED, DIMENSIONS ARE IN INCHES	Juan M. Caicedo

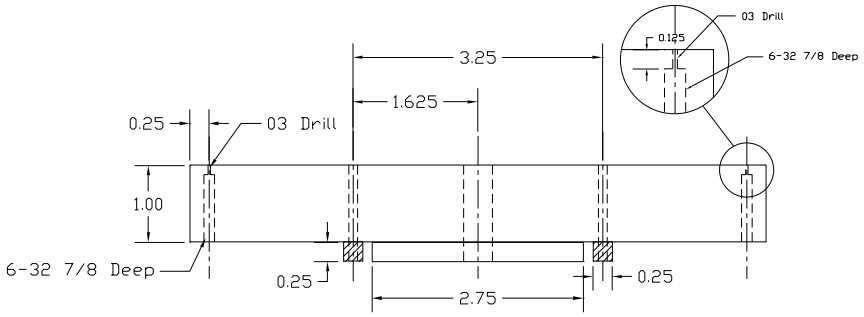

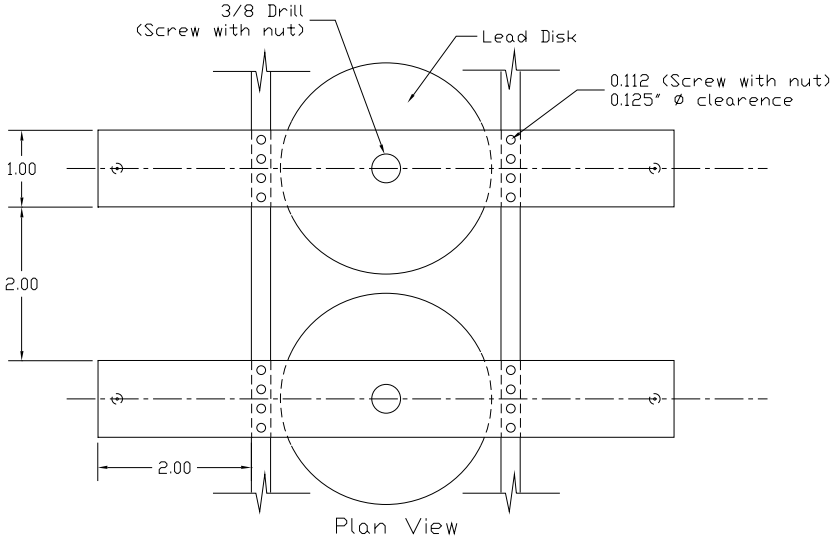

WUSCEEL	
DATE 03/2003	Deck
SCALE 1:2.5 PAGE	
UNLESS OTHERWISE SPECIFIED, DIMENSIONS ARE IN INCHES	Juan M. Caicedo

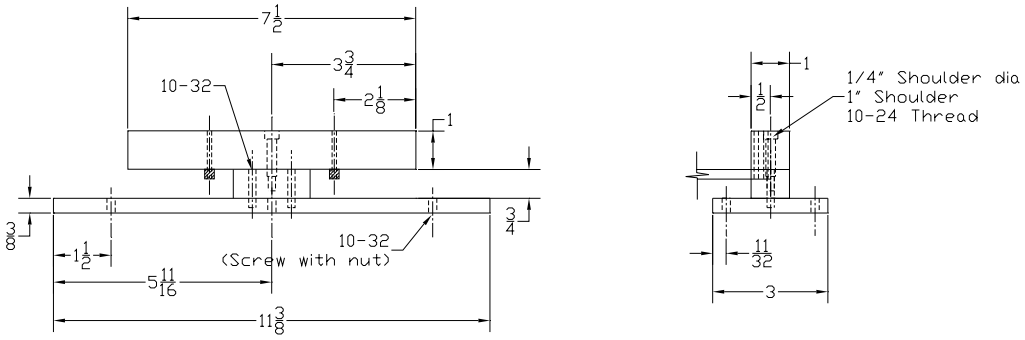

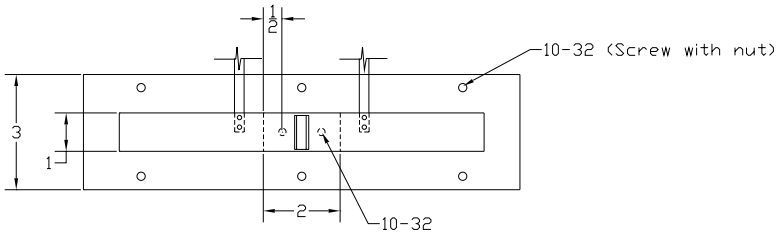

WUSCEEL	
DATE 03/2003	Bent 1 and 3
SCALE 1:5 PAGE	
UNLESS OTHERWISE SPECIFIED, DIMENSIONS ARE IN INCHES	Juan M. Caicedo

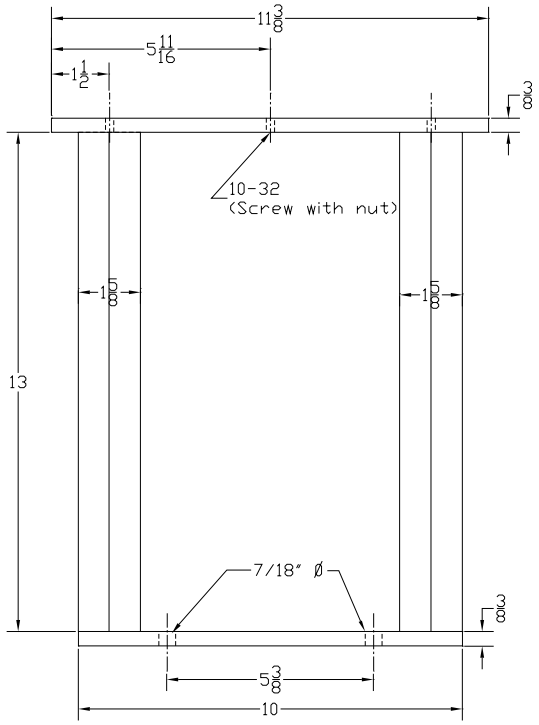

Front View

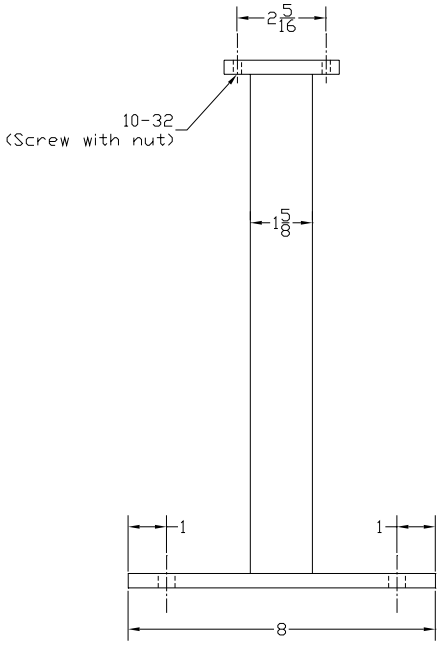

Lateral View

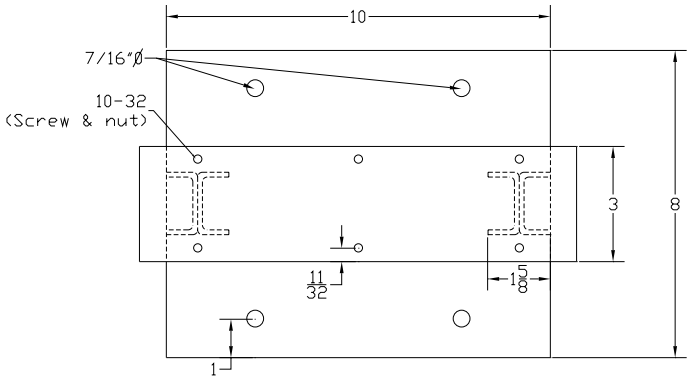

Plan View

WUSCEEL	
DATE 03/2003	Base for tower and bent 1
SCALE 1:5 PAGE	
UNLESS OTHERWISE SPECIFIED, DIMENSIONS ARE IN INCHES	Juan M. Caicedo

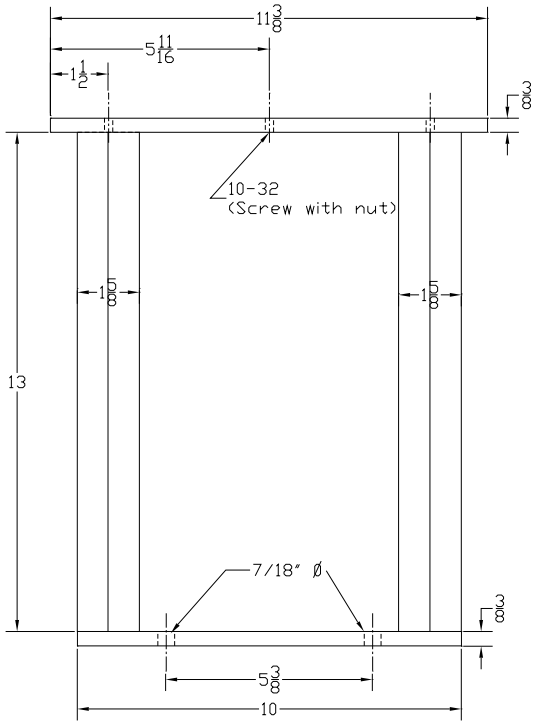

Front View

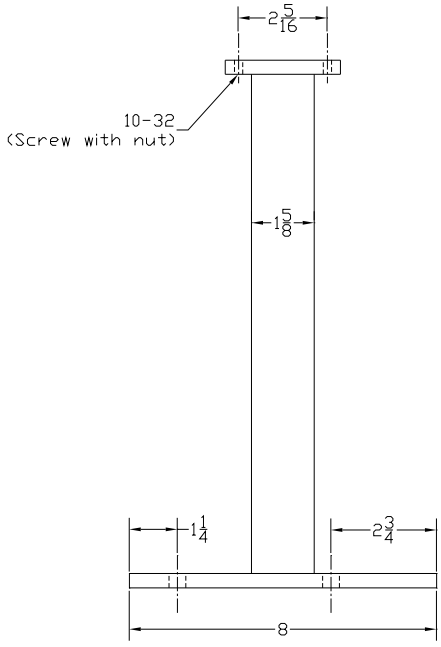

Lateral View

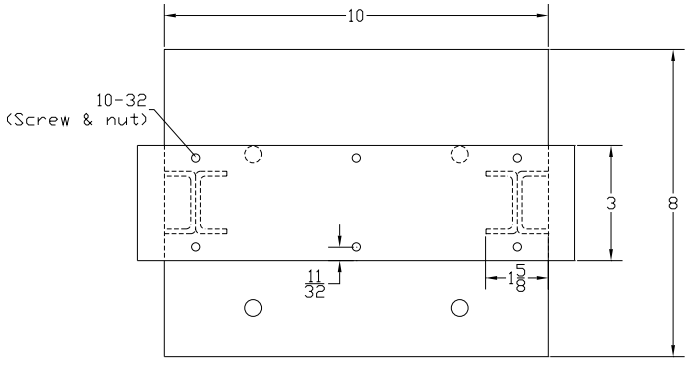

Plan View

WUSCEEL	
DATE 03/2003	Base for bent 3
SCALE 1=4 PAGE	
UNLESS OTHERWISE SPECIFIED, DIMENSIONS ARE IN INCHES	Juan M. Caicedo

References

[1] Au, S.K., Yuen, K.V. and Beck, J.L., “Two-stage System Identification Results for Benchmark Structure”, *Proceedings of the 14th ASCE Engineering Mechanics Conference*, Austin, Texas, May 21-24, 2000.

[2] Asmussen J.C., *Modal Analysis Based on the Random Decrement Technique. Application to Civil Engineering Structures.* Ph.D. Thesis, University of Aalborg, Denmakr, 1997.

[3] Beck, J.L., May, B.S., and Polidori, D.C., “Determination of modal parameters from ambient vibration data for structural health monitoring”, *First World Conference on Structural Control*, California, USA, 3-5 August 1994.

[4] Beck J.L, Katafygiotis, L.S., “Updating Models and Their Uncertainties - Bayesian Statistical Framework”, *Journal of Engineering Mechanics*, Vol. 124, pp. 455-461, 1998.

[5] Bendat, J.S. and Piersol, A.G., “Random Data. Analysis and Measurement Procedures”, John Willey and Sons, Inc, 2000, New York City, NY., 2000.

[6] Bernal, D., Dyke, S.J., Lam H.-F., and Beck, J.L, “Phase II of the ASCE Benchmark Study in SHM,” *Proceedings of the 15th ASCE Engineering Mechanics Conference*, New York, New York, June 2-5, 2002.

[7] Bernal, D., “Load Vectors for Damage Localization”, *Journal of Engineering Mechanics*, Vol. 128(1), pp. 7-14, 2002.

[8] Bernal, D. and Gunes, B., “Observer/Kalman and Subspace Identification of the UBC Benchmark Structural Model”, *Proceedings of the 14th ASCE Engineering Mechanics Conference*, Austin, Texas, May 21-24, 2000.

[9] Black, C.J. and Ventura, C.E. “Blind Test on Damage Detection of a Steel Frame Structure,” *Proceedings of the 16th International Modal Analysis Conf.,* Santa Bar-bara, California, Feb. 2–5, 1998.

[10] Bleich, F. *Bucking Strength of Metal Structures*, McGraw–Hill, New York, 1952.

[11] Caicedo, J.M., Deaton, S., Docker, M. and Orton, S., “Field Mission 2001 Report: The Turquish Earthquakes of 1999”, *Mid America Earthquake Center - Report or the 2001 Field Mission Fellowship*, <http://mae.ce.uiuc.edu/Education/Student/Graduate/Fieldmission/2001.htm>

[12] Caicedo, J.M., “Two Structural Health Monitoring Strategies Based on Global Accleration Responses: Development, Implementation and Verification”, Msc. Thesis. Washington University in St. Louis, May 2001.

[13] Caicedo, J.M., Dyke, S.J., “Phase II SHM Benchmark Studies: Application of the NExT and ERA for damage detection”, *Proceedings of the XXI IMAC Conference*, Kissimmee, Florida, February 3-6, 2003.

[14] Caicedo, J.M., Dyke, S.J. and Johnson, E.A., “Health Monitoring Based on Component Transfer Function”, *Proceedings of the 2000 International Conference on Advaces in Structural Dynamics*, Hong Kong, December 2000.

[15] Caicedo, J.M., Dyke, S.J. and Johnson, E.A., “NExT and ERA for Phase I of the IASC-ASCE Benchmark Problem: Simulated Data.” *Journal of Engineering Mechanics*, ASCE, (in press).

[16] Caicedo, J.M., Dyke, S.J., Turan, G. and Bergman, L.A. “Comparison of Modeling Techniques for Dynamic Analysis of a Cable-Stayed Bridge.” *Proceedings of the Engineering Mechanics Conference, ASCE*, Austin, Texas, May 21–23, 2000.

[17] Caicedo, J.M., Marulanda, J., Thomson, P., and Dyke, S.J. “Monitoring of Bridges to Detect Changes in Structural Health,” *Proceedings of the 2001 American Control Conference*, Arlington Virginia, June 2001.

[18] Çelebi, M., *Final Proposal for Seismic Instrumentation of the Cable-Stayed Girardeau (MO) Bridge*, U.S. Geological Survey, 1998.

[19] Chadwell C.B., Fenves, G.L. and Mahin, S.A., “Cable-Stayed Bridge Behavior Under Earthquake Excitation - A Case Study”, *Proceedings of the Seventh U.S. National Conference on Earthquake Engineering*, Boston, Massachusetts, July 21-25, 2002.

[20] Chang C.S. Study of Dynamic Characteristics of Aerolastic Systems Utilizing Randomdec Signatures. NASA-CR-132563, Feb. 1975.

[21] Chang, F.K. *Structural Health Monitoring*, Proceedings of the 2nd International Workshop on Structural Health Monitoring, Stanford University, Technomic Publishing Co., Lancaster, PA, September 8-10, 1999.

[22] Ching, J., Beck, J.L., “Two-Stage Bayesian Structural Health Monitoring Approach for Phase II ASCE Experimental Benchmark Studies”, *Proceedings of the 16th ASCE Engineering Mechanics Conference*, Seattle, Washington, July 16-18, 2003.

[23] Chopra, A.K., *Dynamics of Structures*, Prentince Hall Inc., Upper Saddle River, NJ, 1995.

[24] Cole, H.A., "On-the-line analysis of Random Vibrations," *AIAA*, Paper No. 68-288, 1968.

[25] Cook, R.D., Malkus, D.S. and Plesha, M.E., *Concepts and Applications of Finite element Analysis*, John Wiley & Sons Inc., New York City, NY, 1989.

[26] Corbin, M., Hera, A., and Hou, Z., "Locating Damage Regions Using Wavelet Approach", *Proceedings of the 14th ASCE Engineering Mechanics Conference*, Austin, Texas, May 21-24, 2000.

[27] Dorf, R.C. and Bishop, R.H., *Modern Control Systems*, Addison-Wesley Longman, Inc., Menlo Park, CA, 1998.

[28] Doebling, S.W., Farrar, C.R., Prime, M.B., and Schevitz, D.W. *Damage Identification and Health Monitoring of Structural and Mechanical Systems from Changes in their Vibration Characteristics: A Literature Review*, Los Alamos Report, LA-13070-MS, May, 1996

[29] Doebling, S.W., Farrar, C.R., and Prime M.B., "A Summary Review of Vibration-Based Damage Identification Methods", *The Shock and Vibration Digest*, Vol 30(2), pp. 91- 105, 1998.

[30] Dyke, S.J., Bernal, D., Beck, J.L., and Ventura, C., "Introducing an Experimental Benchmark Problem in Structural Health Monitoring," *Book of Abstracts, Joint ASME/ASCE Mechanics and Materials Conference*, Arlington, Virginia, June 27–29, 2001.

[31] Dyke, S.J., Bernal, D., Beck, J.L., and Ventura, C., "Experimental Phase II of the Structural Health Monitoring Benchmark Problem", *Proceedings of the 16th Engineering Mechanics Conference*, Seattle, Washington, July 16-18, 2003.

[32] Dyke, S.J., Bernal, D., Beck, J.L., and Ventura, C., "An Experimental Benchmark Problem in Structural Health Monitoring," *Proceedings of the 3rd International Workshop on Structural Health Monitoring*, Stanford, California, September 12-14, 2001.

[33] Dyke, S.J., Caicedo, J.M., and Johnson, E.A., "Monitoring of a Benchmark Structure for Damage Detection," *Proceedings of the 14th ASCE Engineering Mechanics Conference*, Austin, Texas, May 21-24, 2000.

[34] Dyke, S.J., Caicedo, J.M., Turan, G., Bergman, L.A., and Hague, S., "Phase I Benchmark Control Problem for Seismic Response of Cable-Stayed Bridges," *Journal of Structural Engineering*, Vol. 129(7), July 2003.

[35] Ernst, H.J. "Der E-Modul von Seilen unter Berucksichtigung des Durchhanges," *Der Bauingenieur*, Vol. 40(2), 1965.

[36] Farrar, C.R., Baker, W.E., Bell, T.M., Cone, K.M., Darling, T.W., Duffey, T.A., Eklund, A. and Migliory A., "Dynamic characterization and damage detection in the I-40 brodge over the Rio Grande," *Los Alamos National Laboratory,* Report LA-12767-MS., 1994.

[37] Farrar, C.R. and James, G. H., "System identification from Ambient vibration measurements on a bridge," *Journal of Sound and Vibration*, Vol. 205(1) p 1-18, 1997.

[38] Fleming, J. F., "Computer Analysis of Structural Systems", New York, McGraw Hill, 1989.

[39] Ghanem, R. and Shinozuka, M., "Structural-System Identification. I: Theory", *Journal of Engineering Mechanics*, Vol. 121(2), February, 1995.

[40] Giraldo, D.F., Caicedo, J.M. and Dyke, S.J., "Experimental phase of the SHM Benchmark Studies. Damage detection using NExT and ERA", *Proceedings of the 16th Engineering Mechanics Conference*, Seattle, Washington, July 16-18, 2003.

[41] Hague, S. "Composite Design for Long Span Bridges." *Proceedings of the XV ASCE Structures Congress*, Portland, Oregon, 1997.

[42] Hou, Z.K., Noori, M. and St. Amanda, R. "Wavelet-based approach for Structural Damage Detection," Journal of Engineering Mechanics, Vol. 126(7), pp. 677-683, 2000.

[43] Huang, C.S., Yang, Y.B., Lu L.Y. and Chen, C.H., "Dynamic testing and system identification of a multi-span highway bridge", *Earthquake Engineering and Structural Dynamics.* Vol. 28, pp. 857-878, 1999.

[44] IASC-ASCE Structural Health Monitoring Task Group Web Page: http:// wusceel.cive.wustl.edu/asce.shm/

[45] James, G.H., Carne, T.G., Lauffer J.P., Nord A.R., "Modal Testing using Natural Excitation", *Proceedings of the 10th International Modal Analysis Conference*, Sant Diego, California, 1992.

[46] James, G.H., Carne, T.G. and Lauffer J.P., “The Natural Excitation Technique (NExT) for Modal Parameter Extraction From Operating Wind Turbines,” Experimental Mechanics Department, Sandia National Laboratories Report SAND92-1666, Albuquerque, NM, Feb, 1993.

[47] James, G.H., Carne, T.G., Mayes, R.L., “Modal Parameter Extraction from Large Operating Structures Using Ambient Excitation,” *Proceedings of the 14th International Modal Analysis Conference*, Darbon, Michigan, 1996.

[48] Juang, J-N., “Applied System Identification”, Pearson Education, 1993.

[49] Juang, J.-N. and Pappa, R.S., “An Eigensystem Realization Algorithm for Modal Parameter Identification and Model Reduction.” *Journal of Guidance Control and Dynamic*s, Vol 8, pp. 620–627, 1985.

[50] Juang, J.-N. and Pappa, R.S., “Effects of Noise on Modal Parameters Identified by the Eigensystem Realization Algorithm," *Journal of Guidance, Control, and Dynamics*, Vol. 9, No. 3, pp. 294-303, May-June 1986.

[51] Juang, J-N., Phan M. Q., “Identification and control of mechanical systems”, Cambridge University Press, 2001.

[52] Johnson E.A., Lam H.F., Katafygiotis L. and Beck J., “A Benchmark Problem for Structural Health Monitoring and Damage Detection”, *Proceedings of the 14th ASCE Engineering Mechanics Conference*, Austin, Texas, May 21-24, 2000.

[53] Katafygiotis L.S., Lam H.F., Mickleborough N., “Application of a Statistical Approach on a Benchmark Damage Detection Problem”, *Proceedings of the 14th ASCE Engineering Mechanics Conference*, Austin, Texas, May 21-24, 2000.

[54] Kawashima, K., “Damage of Bridges Resulting from Fault Rupture in the 1999 Kocaeli and Duzce, Turkey earthquakes and the 1999 Chi-Chi, Taiwan Earthquake”, *Struct Eng./Earthquake Eng., JSCE*, Vol 19(2), pp. 179-197, 2002.

[55] Kim, C.-Y., Jung, D.-S., Kim, N.-S. and Yoon, J.-G., “Effect of Vehicle Mass on the Measured Dynamic Characteristics of Bridges from Traffic-Induced Vibration Tests”. *Proceedings of the XIX IMAC Conference*, Kissemmee, Florida, February 5-8, 2001.

[56] Kim, C.-Y., Kim, N.-S., Yoon, J.-G. and Jung, D.-S., “Monitoring System and Ambient Vibration test of Namhae Suspension Bridge”. *Proceedings of the SPIE’s 5th Annual International Symposium on Nondestructive Evaluation and Health Monitoring of Aging Infrastructure*, Newport Beach, California, March 5-9, 2000.

[57] Kim, S-E., Kim, Y., Choi, S-H., “Nonlinear Analysis of 3-D Steel Frames”, *Thin-Walled Structures*, Vol. 39, pp. 445-461, 2001.

[58] Ko, J.M., Ni, Y.Q., Wang, J.Y., Zun, Z.G. and Zhou X.T., “Studies of Vibration-Based Damage Detection of Three Cable-Supported Bridges in Hong Kong”, *Proceedings of the International Conference on Engineering and Technological Sciences*, Beijing, China, 2000.

[59] Lam, H.F., “Phase IIe of the IASC-ASCE Benchmark Study on Structural Health Monitoring”, *Proceedings of the XXI IMAC Conference*, Kissimii, Florida, February 3-6, 2003.

[60] Lew, J.S., Juang J.-N., and Longman, R.W., “Comparasion of Several System Identification Methods for Flexible Structures”, *Journal of Sound and Vibration*, Vol. 167, pp. 461-480, 1993.

[61] Lutes, L.D., Sarkani, S., “Stochastic Analysis of Structural and Mechanical Vibrations”, Prentince Hall, New Jersey, 1997.

[62] Lynch, J.P., “Descentralization of Wireless Monitoring and Control Technologies for Smart Civil Structures”, Ph.D. Dissertation, Department of Civil Engineering, Stanford University, August 2002.

[63] Marwala, T. and Heyns, P.S., “Multiple-Criterion method for determining strucural damage”. *AIAA Journal* Vol. 36(8), August 1998.

[64] Matlab® . The Math Works, Inc. Natick, Massachusetts, 1997.

[65] Nazmy A.S., Abdel-Ghaffar A. M., “Three-Dimensional Nonlinear Static Analysis of Cable-Stayed bridges”, *Computers & Structures*, Vol. 34(2), pp. 257-271, 1990.

[66] New Jersey Department of Transportation, “Fiscal Year 2003 Capital Program”, <http://www.state.nj.us/transportation/cpd/tcp/draft/Section2Activities/FY03%20CP%20SEC%202%20Construction.PDF>.

[67] Ni, Y.Q., Zhou, X.T., Ko, J.M., Wang, B.S., “Vibration-Based Damage Localization in Ting Kau Bridge Using Probabilistic Neural Networks”, *Advances in Structural Dynamics*, Vol. 2, pp. 1069-1076, 2000.

[68] Non Destructive Evaluation Validation Center - Federal Highway Administration, “Reliability of Visual Inspection for Highway Bridges”, <http://www.tfhrc.gov/hnr20/nde/01020.htm>.

[69] Nolambi J.-M., Vantomme J., and Harri K. “Damage assessment in reinforced concrete beams using eigenfrequencies and mode shape derivatives”. *Engineering Structures*, Vol. 24, 2002.

[70] Papoulis, A., “Probability, random variables, and stochastic processes”, McGraw Hill, New York, 1991.

[71] Pappa, R.S., Juang, J.-N, “Some Experiences with the Eigensystem Realization Algorithm”, *Journal of Sound and Vibration*, pp. 30-34, January 1998.

[72] Pines, J. D. and Lovell, P.A., “Conceptual Framework of a Remote Wireless Health Monitoring System for Large Civil Structures”, *Smart Materials and Structures*, Vol. 7, pp. 627-636, 1998.

[73] Qin, Q., Li H.B. and Qian L.Z., “Modal Identification of Tsing Ma Bridge by Using Improved Eigensystem Realization Algorithm”, *Journal of Sound and Vibration*, Vol. 247, pp. 325-341, 2001.

[74] Quast, P., Spencer, B.F., Sain, M.K. and Dyke, S.J., Microcomputer Implementations of Digital Control Strategies for Structural Response Reduction, *Microcomputers in Civil Engineering: Special Issue on New Directions in Computer Aided Structural System Analysis, Design and Optimization*, Vol. 10, pp. 13–25, 1995.

[75] Rao R., Mitra S.K., “Generalized Inverse of Matrices and its Applications”, John Willey and Sons, New York, 1971.

[76] Rytter, A., *Vibration Based Inspection of Civil Engineering Structures*, Ph. D. Dissertation, Department of Building Technology and Structural Engineering, Aalborg University, Denmark, 1993.

[77] Salawu, O.S., “Detection of Structural Damage through Changes in Frequency: a review”, *Engineering Structures*, Vol. 19(9), pp. 718–723, 1997.

[78] Seattle Department of Transportation, “Post-Earthquake Bridge Inspection”, <http://www.cityofseattle.net/transportation/bridgeinfo.htm#seismic>

[79] Schmidt, H., “Resolution Bias Errors in Spectral Density, Frequency Response and Coherence Function Measurements, I: General Theory”, *Journal of Sound and Vibration*, Vol. 101(3), 1985.

[80] Schmidt, H., “Resolution Bias Errors in Spectral Density, Frequency Response and Coherence Function Measuremente, III: Application to Second-Order Systems (White Noise Excitation”, *Journal of Sound and Vibration*, Vol. 101(3), 1985

[81] Shinozuka, M. and Ghanem, R., “Structural System Identification. II: Experimental Verification”, *Journal of Engineering Mechanics*, Vol. 121, No. 2., February 1995.

[82] Thomson, P., Marulanda Casas, J., Marulanda Arbelaes, J., Caicedo, J. M., “Real Time Health Monitoring of Civil Infraestructures Systems in Colombia”, *Proceedings of the SPIE 6th Annual International Symposium on NDE for Health Monitoring an Diagnostics*, Newport Beach, California, 4-8 March, 2001.

[83] Turan, G., “Active Control of a Cable-stayed Bridge Against Earthquake Excitations”, Ph.D. diss., University of Illinois, 2001.

[84] Wang, B.S., Liang, X.B., Ni, Y.Q. and Ko, J.M., “Comparative Study of Damage Indices in Application to a Long-Span Suspension Bridge”, *Advances in Structural Dynamics*, Vol. 2, pp. 1085-1092, 2000.

[85] Wang P.H., Tseng T.C., Yang C.G., “Initial Shape of Cable-Stayed Bridges”, *Computers & Structures*, Vol. 46, No. 6, pp. 1095-1106, 1993.

[86] Wilson, J., and Gravelle W. “Modelling of a Cable-Stayed Bridge for Dynamic Analysis,” *Earthquake Engineering and Structural Dynamics*, Vol. 20, pp. 707-721, 1991

Vita

Juan M. Caicedo

EDUCATION

- Washington University, St. Louis, MO: D.Sc. Civil Engineering, 2003
- Washington University, St. Louis, MO: M.S. Civil Engineering, 2001
- Universidad del Valle, Cali, Colombia, South America: B.S. Civil Engineering, 1998

PUBLICATIONS

- Caicedo, J.M., Dyke S.J. and Johnson, E.A, "NExT and ERA for Phase I of the IASC-ASCE Benchmark Problem: Simulated Data", *Journal of Engineering Mechanics* (in press).
- Dyke S.J., Caicedo J.M., Turan, G., Bergman, L.A. and Hague, S., "Phase I Benchmark Control Problem for Seismic Response of Cable-Stayed Bridges", *Journal of Structural Engineering*, Vol. 129, No. 7, July 1 2003.

PROFESSIONAL HISTORY

- Research Assistant - Washington University Structural Control & Earthquake Engineering Laboratory, St. Louis, MO (1999-present).
- Assistant Engineer - LECA Ingenieros Soc. L.T.D.A, Cali, Colombia, South America (1997-1998)
- Undergraduate Teaching and Research Assistant - School of Civil Engineering, Universidad del Valle, Cali, Colombia, South America (1996-1997).

AFFILIATIONS

- Earthquake Engineering Research Institute (2000-present)
- Chi-Epsilon, Civil Engineering Honor Society (2002-present)

August 2003